Stony Brook University

Carbon Nanoparticle Enhance Photoacoustic Imaging and Therapy for Bone Tissue Engineering

A Dissertation Presented

by

Yahfi Talukdar

to

The Graduate School

in Partial Fulfillment of the

Requirements

for the Degree of

Doctor of Philosophy

in

Biomedical Engineering

Stony Brook University

May 2017

Stony Brook University

The Graduate School

Yahfi Talukdar

We, the dissertation committee for the above candidate for the

Doctor of Philosophy degree, hereby recommend

acceptance of this dissertation.

Balaji Sitharaman – Dissertation Advisor
Associate Professor, Department of Biomedical Engineering

Yi-Xian Qin - Chairperson of Defense
Professor, Department of Biomedical Engineering

Paul Vaska
Professor, Department of Biomedical Engineering

James Penna
Associate Professor, Department of Orthopedic Surgery
Stony Brook Medicine

This dissertation is accepted by the Graduate School

Charles Taber

Dean of the Graduate School

Abstract of the Dissertation

Carbon Nanoparticle Enhanced Photoacoustic Imaging and Therapy for Bone Tissue Engineering

by

Yahfi Talukdar

Doctor of Philosophy

in

Biomedical Engineering

Stony Brook University

2017

Healing critical sized bone defects has been a challenge that led to innovations in tissue engineering scaffolds and biomechanical stimulations that enhance tissue regeneration. Carbon nanocomposite scaffolds have gained interest due to their enhanced mechanical properties. However, these scaffolds are only osteoconductive and not osteoinductive. Stimulating regeneration of bone tissue, osteoinductivity, has therefore been a subject of intense research. We propose the use of carbon nanoparticle enhanced photoacoustic (PA) stimulation to promote and enhance tissue regeneration in bone tissue-engineering scaffolds. In this study we test the feasibility of using carbon nanoparticles and PA for *in vivo* tissue engineering applications. To this end, we investigate 1) the effect of carbon nanoparticles, such as graphene oxide nanoplatelets (GONP), graphene oxide nano ribbons (GONR) and graphene nano onions (GNO), *in vitro* on mesenchymal stem cells (MSC), which are crucial for bone regeneration; 2) the use of

PA imaging to detect and monitor tissue engineering scaffolds *in vivo;* and 3) we demonstrate the potential of carbon nanoparticle enhanced PA stimulation to promote tissue regeneration and healing in an *in vivo* rat fracture model. The results from these studies demonstrate that carbon nanoparticles such as GNOP, GONR and GNO do not affect viability or differentiation of MSCs and could potentially be used *in vivo* for tissue engineering applications. Furthermore, PA imaging can be used to detect and longitudinally monitor subcutaneously implanted carbon nanotubes incorporated polymeric nanocomposites *in vivo*. Oxygen saturation data from PA imaging could also be used as an indicator for tissue regeneration within the scaffolds. Lastly, we demonstrate that daily stimulation with carbon nanoparticle enhanced PA increases bone fracture healing. Rats stimulated for 10 minutes daily for two weeks showed 3 times higher new cortical bone BV/TV and 1.8 times bone mineral density, compared to non-stimulated controls. The results taken together indicate that carbon nanoparticle enhanced PA stimulation serves as an anabolic stimulus for bone regeneration. The results suggest opportunities towards the development of implant device combination therapies for bone loss due to disease or trauma.

Dedication Page

For my family, teachers and mentors over the years

Table of Contents

Table of Contents

List of Figures

Chapter 1

Chapter 2

Figure 1: Representative HRTEM images of GNOs (A), GONRs (B), and GONPs (C). Scale bars: (A) 10 nm, (B) 50 nm, and (C) 10 nm. (D) Representative Raman spectra of GNOs (a), GONRs (b), and GONPs (c). (E) TGA profiles of GNOs, GONRs, and GONPs.

Figure 2: AlamarBlue assay results at one and three days after treatment with GNOs (A), GONRs (B), and GONPs (C) for adMSCs; after treatment with GNOs (D), GONRs (E), and GONPs (F) for bmMSCs. For each nanoparticle, cells were treated with PEG-DSPE, 5 μg/ml, 10 μg/ml, 50 μg/ml, 100 μg/ml, and 300 μg/ml concentrations. Data are presented as mean +/- standard deviation of percentage viability compared to untreated cells (n=4). Statistical significance ($p<0.05$) with respect to untreated groups, 5 μg/ml groups, and 10 μg/ml groups is denoted by (*), (#), and (+) respectively.

Figure 3: Calcein AM assay results at one and three days after treatment with GNOs (A), GONRs (B), and GONPs (C) for adMSCs; after treatment with GNOs (D), GONRs (E), and GONPs (F) for bmMSCs. For each nanoparticle, cells were treated with PEG-DSPE, at 5 μg/ml, 10 μg/ml, 50 μg/ml, 100 μg/ml, and 300 μg/ml concentrations. Data are presented as mean +/- standard deviation of percentage viability compared to untreated cells (n=4). Statistical significance ($p<0.05$) with respect to untreated groups, 5 μg/ml groups, and 10 μg/ml groups is denoted by (*), (#), and (+) respectively.

Figure 4: Adipogenesis results. (A) Histological specimens of adMSCs incubated with GNOs, GONRs, and GONPs for 24 hours, followed by incubation with adipogenic differentiation media for 21 days, stained by Oil Red O. (B) Elution of Oil Red O stain. Data are normalized to control values and presented as mean +/- standard deviation

(n=3). Statistical significance (p<0.05) compared to the control was determined by the Kruskal-Wallis test with Dunn's post hoc (*).

Figure 5: Osteogenesis results. adMSCs after treatment for 24 hours with either 10 or 50 μg/ml of GNOs, GONRs, or GONPs respectively, followed by 14 days of incubation with osteogenic differentiation media stained with Alizarin Red S.

Figure 6: Osteogenesis results. (A) Cellularity for adMSCs after treatment for 24 hours with either 10 or 50 μg/ml of GNOs, GONRs, or GONPs, followed by 14 days of incubation with osteogenic differentiation media. (B) ALP activity in adMSCs after treatment for 24 hours with either 10 or 50 μg/ml of GNOs, GONRs, or GONPs, followed by 14 days of incubation with osteogenic differentiation media. (C) Calcium content after treatment for 24 hours with either 10 or 50 μg/ml of GNOs, GONRs, or GONPs, followed by 14 days of incubation with osteogenic differentiation media. Data are presented as mean +/- standard deviation of mg of calcium per well (n=3). Statistical significance (p<0.05) compared to the control was determined by the Kruskal-Wallis test with Dunn's post hoc (*).

Figure 7: Representative TEM images of adMSCs treated with GNOs (A & B) and GONPs (C & D). GNOs aggregates (yellow arrow) are seen in vacuoles (green arrows) in the cytoplasm of the cell. GNOs are not seen inside the nucleus (black arrow). GONPs particles (blue arrows) are seen in the cytoplasm enclosed in vacuoles. They can also been seen inside the nucleus (red arrows).

Figure 8: A, D and G show representative brightfield images of adMSCs treated with GNOs, GONRs, and GONPs, respectively. B, E, H show the confocal Raman map of

selected regions in A, D, and G. Parts C, F and I show characteristic D- and G-band spectra of GNOs, GONRs, and GONPs employed to obtain confocal Raman maps of these nanoparticles.

Chapter 3

Figure 1: (A) Representative AFM image of a SWCNT. Inset is a cross-sectional topography plot of this nanotube that shows its diameter to be ~ 1 nm. (B) Optical images of PLGA and SWCNT-PLGA (C) SEM images of SWCNT-PLGA scaffold with scale bar showing 1 μm. The orange arrows point to SWCNTs and the green arrows point to PLGA polymer matrix. (D) MicroCT image of SWCNT-PLGA scaffold with scale bar of 5 μm.

Figure 2: US-PA images of PLGA (A, B & C) and SWCNT-PLGA (D, E and F) scaffold imaged at 680 nm embedded into chicken breast tissue at depths of (A & D) 0.5 mm, (B & E) 2 mm and (C & F) 6 mm. (G) 3D US-PA image rendition of SWCNT-PLGA scaffold embedded 0.5 mm in chicken breast tissue.

Figure 3: Representative US-PA images of PLGA (A & B) and SWCNT-PLGA (C & D) scaffolds in vivo. The scaffolds were implanted into subcutaneous pockets and imaged on day 7 (A &C) and day 14 (B &D) post-surgery. (E) 3D rendering of SWCNT-PLGA scaffold under the skin at day 7 imaged at 780 nm. Scale bar represents 2 mm.

Figure 4: Representative blood oxygen saturation maps of PLGA (A & B) and SWCNT-PLGA (C & D) scaffolds taken day 7 (A & C) and 14 (B &D) post-surgery. Scale bar represents 2 mm.

(D) bone mineral density of whole callus formed at fracture site. Statistical significance, denoted by (*), was determined by two-tailed, unpaired student t-test with $p<0.05$

Figure 5: MicroCT analysis of the proximal end of the fracture site of non-stimulated controls and photoacoustic stimulated (PA) groups two weeks following surgery. (A) Total volume, (B) BV/TV of calcified cartilage and new bone, (C) BV/TV of dense cortical bone and (D) bone mineral density of callus formed at the proximal end of the fracture site. Statistical significance, denoted by (*), was determined by two-tailed, unpaired student t-test with $p<0.05$

Figure 6: MicroCT analysis of the distal end of the fracture site of non-stimulated controls and photoacoustic stimulated (PA) groups two weeks following surgery. (A) Total volume, (B) BV/TV of calcified cartilage and new bone, (C) BV/TV of dense cortical bone and (D) bone mineral density of callus formed at the distal end of the fracture site. Statistical significance, denoted by (*), was determined by two-tailed, unpaired student t-test with $p<0.05$

Figure 7: Representative histological sections of fracture site from (A) non-stimulated controls and (B) photoacoustic stimulated groups two weeks following surgery stained with masson's trichrome. (C) Graph shows cartilage area normalized to callus area of the two groups. Statistical significance, denoted by (*), was determined by two-tailed, unpaired student t-test with $p<0.05$

List of Tables

Chapter 1

Chapter 2

List of Abbreviations

ALP	Alkaline phosphate
ANSI	American National Standards Institute
BMD	Bone mineral density
bmMSCs	Bone derived mesenchymal stem cells
BV/TV	Bone volume to total volume ratio
CA	Cartilage area
CEPS	Carbon nanoparticle enhanced photoacoustic stimulation
CNT	Carbon nanotubes
CON	Control
CT	X-ray computed tomography
DSPE-PEG	Distearoyl-sn-glycero-3-phosphoethanolamine-N-[amino(polyethylene glycol)]
EM	Electromagnetic
GNR	Graphene nanoribbons
GONP	Graphene oxide nanoplatelets
GONR	Graphene oxide nanoribbons
LIPUS	low intensity pulsed ultrasound
MRI	Magnetic resonance imaging
MSC	Mesenchymal stem cells
MWCNT	Multi walled carbon nanotubes
NIR	Near infrared
O-MWGNR	Oxidized multi walled graphene nanoribbons

O-SWGNR	Oxidized single walled graphene nanoribbons
OCT	Optical coherence tomography
OPN	Osteopontin
PA	Photoacoustic
PAM	Photoacoustic microscopy
PAS	Photoacoustic signals
PET	Positron emission tomography
PEMF	Pulsed Electromagnetic Field
PLGA	Poly(lactic-co-glycolic acid)
SEM	Scanning electron microscopy
SWCNT	Single walled carbon nanotubes
SWCNT-PLGA	SWCNT incorporated PLGA scaffold
TCA	Total callus area
TEM	Transmission electron microscopy
TGA	Thermogravimetric analysis
TV	Total volume
US	Ultrasound
US-PA	Ultrasound coregistered PA image

Publications

1. Talukdar Y, Avti P, Sun J, Sitharaman B. Multimodal ultrasound-photoacoustic imaging of tissue engineering scaffolds and blood oxygen saturation in and around the scaffolds. Tissue Engineering Part C: Methods. 2014;20(5):440-9.

2. Talukdar Y, Rashkow JT, Lalwani G, Kanakia S, Sitharaman B. The effects of graphene nanostructures on mesenchymal stem cells. Biomaterials. 2014;35(18):4863-77.

3. Rashkow JT, Talukdar Y, Lalwani G, Sitharaman B. Interactions of 1D-and 2D-layered inorganic nanoparticles with fibroblasts and human mesenchymal stem cells. Nanomedicine. 2015;10(11):1693-706.

4. Lalwani G, D'Agati M, Gopalan A, Patel SC, Talukdar Y, Sitharaman B. Three Dimensional Carbon Nanotube Scaffolds for Long-Term Maintenance and Expansion of Human Mesenchymal Stem Cells. Journal of Biomedical Materials Research Part A. 2017.

5. Avti PK, Talukdar Y, Sirotkin MV, Shroyer KR, Sitharaman B. Toward single-walled carbon nanotube–gadolinium complex as advanced MRI contrast agents: Pharmacodynamics and global genomic response in small animals. Journal of Biomedical Materials Research Part B: Applied Biomaterials. 2013;101(6):1039-49.

6. Sitharaman B, Avti PK, Schaefer K, Talukdar Y, Longtin JP. A novel nanoparticle-enhanced photoacoustic stimulus for bone tissue engineering. Tissue Engineering Part A. 2011;17(13-14):1851-8.

Chapter 1

Photoacoustic Stimulation for Bone Tissue Engineering

Bone defects and grafts

Bones give structure and shape to the body and allow locomotion. They provide protection and support to internal organs and act as storage for minerals and fat[1]. Even though they appear to be inert and stable, bones are dynamic tissues undergoing constant breakdown and renewal. A healthy bone, composed of 35% organic matrix and 65% inorganic elements, is maintained by osteoblasts and osteoclasts that strike a balance between bone formation and resorption respectively, in response to environmental mechanical and chemical cues[1]. This dynamic nature of the bone allows it to heal itself when injured. Injury to the bone is most commonly in the form of fractures, which are discontinuities in the bone caused by application of mechanical load higher than its allowable stress.[2] Most fractures heal by themselves with minimal or no medical interventions. But a healthy bone can heal itself only when the fractured ends are near. This is a major limitation in bone defects that are too large for the body to heal on its own. Most common causes for large bone defects are trauma, infection and cancer. These defects are filled with grafts that provide mechanical support and a suitable environment for regenerating bone tissue.[3]

The gold standard of bone grafts is autografts, that are bone tissues taken from another part of the body, usually the iliac crest, and placed at the defect site.[4] Since autografts are taken from the patient's own body, they pose no risks of immune rejection. Autografts contain complete bone tissue with mineralized matrix, bone cells and blood vessels and provide the best possible environment for regeneration. They are osteoconductive, allow bone cells to adhere, proliferate and produce bone matrix; osteoinductive, stimulate differentiation of preosteoblasts to osteoblasts; and osteogenic, provide stem cells and osteoblasts for new bone formation. The limitations of autografts, include, but are not limited to, necessity of additional surgery, risks of infection at surgery site, bone morbidity at donor site and lack of availability. To address these limitations allografts and xenografts have been developed as alternatives.

Allografts are bone tissues obtained from cadavers that donated their bodies for medical purposes and xenografts are either cow bone tissue or corals[5, 6]. These tissues are treated with freeze-drying, irradiation, acid washes, etc that could potential alter the mechanical and chemical structure of the grafts. Even with these treatments designed to minimize infection and transplant rejection, these grafts pose significant risks of inter and intra species disease transmission. To avoid such complications, scientists are invested in tissue engineering to develop synthetic grafts with various biomaterials that mimic native bone tissue or its properties to support and stimulate bone tissue regeneration.

Tissue Engineering

Tissue engineering is the use of biomaterials, chemicals and cells to replace or regenerate biological functions of damaged or injured tissue. Knowledge of mechanical properties, physiology and biochemistry is used to engineer scaffolds that would support and promote tissue regeneration[3]. Tissue engineering has developed exponentially over the past decade and has shown potential in regenerating small defects to whole organs[7-9]. Even though it is being investigated for regenerating various tissue types, most advances have been made in developing bone tissue engineering scaffolds[10]. Global tissue engineering scaffold market is expected to increase at the rate of 15% per year[11]. More than half a million bone grafts are performed each year in USA, with a market value forecasted to reach $3.3 billion in 2017[3]. Bone tissue engineering scaffolds could not only provide an alternative to contemporary bone grafts, but could potentially be the most efficient and cost-effective treatment of critical sized bone defects. The number of companies involved in tissue engineering has grown from 50 in 2007 to 391 in 2010, but only a few of these companies have successfully developed products that are currently in clinic[3]. This is mostly due to the complex design and regulatory considerations involved in developing bone tissue engineering scaffolds.

An ideal bone tissue engineering scaffold would be osteoconductive, osteoinductive and osteogenic. It will have mechanical properties like that of bone and be highly porous to allow tissue penetration. The scaffold needs to be made of material that would allow bone cells to adhere, proliferate and deposit extracellular matrix. The material and its degraded products have to be biocompatible[12]. The scaffold must be degradable; to allow bone tissue to eventually replace the scaffold material, but it must be mechanically strong enough to support the defect site till enough tissue has regenerated to take over its function. These scaffolds need to be sterilizable and stable on storage[12]. These design challenges have significantly delayed clinical entry of synthetic bone grafts, but advances in cell biology, nanotechnology and biomedical engineering has opened avenues to potential solutions. Mesenchymal stem cells (MSC) and preosteoblasts can now be directed to osteoblast lineages via chemical or mechanical cues [3, 6, 13]. Systemic or local delivery of therapeutic agents can accelerate bone formation or hinder bone resporption. Administration of these therapeutic agents have been challenging due to poor physiological stability, non-specific targeting and low cell-membrane permeability [14]. To overcome these limitations various mechanical stimulation technologies have been developed for bone tissue regeneration. To achieve functional tissue regeneration, mechanical stimulation of the bone cells is crucial. Such stimulation could be in the form of vibration, ultrasound, fluid shear stress etc. [13] In this study, we propose the use of a novel biophysical stimulus, photoacoustic (PA) effect, to enhance tissue regeneration in bone tissue engineering scaffolds. Furthermore, we propose to demonstrate the feasibility of using PA technology to image tissue engineering scaffolds and monitor tissue regeneration *in vivo*. With the synergistic effect of biocompatible polymers, nanoparticles and mechanical stimulation, our technology will encompass all the aforementioned criteria required to make an ideal tissue engineering scaffold.

Photoacoustic Effect

Photoacoustic effect is the formation of ultrasound waves from a surface following absorption of pulsed electromagnetic waves. The energy from each pulse causes a rapid expansion followed by contraction of the surface, which produces pressure waves that decimate as ultrasound[15]. PA technology is currently being developed for bioimaging applications[16-18]. It is advantageous over contemporary imaging modalities due to its high penetration depth, compared to optical imaging, and high contrast, compared to ultrasound (more in Chapter 3). PA images have high ultrasound resolution and high optical contrast due to selective absorption of the stimulating electromagnetic wave. *In-vivo* melatonin and hemoglobin are the only endogenouos absorbers and can be imaged without any contrast agents[19]. Furthermore, differential absorption of oxyhemoglobin and hemoglobin allows determination of oxygen saturation within the tissue. In this proposed research, we will use this technology to determine tissue regeneration within tissue engineering scaffolds. Longitudinal monitoring of oxygen saturation within the scaffold will allow determination of vasculogenesis and angiogenesis within these scaffolds. PA signal generated by hemoglobin, although sufficient for imaging, could potentially not be robust enough for mechanically stimulating bone cells to enhance tissue regeneration *in vivo*. To enhance PA intensity, we will utilize carbon nanoparticles that could be used a film on the skin surface at the fracture site or potentially be embedded into polymeric scaffold matrix.

Carbon Nanoparticles

Nanoparticles are particles that have at least one dimension smaller than 100 nm. Carbon nanoparticles are allotropes of carbon with hexagonal lattice structure formed by conjugated sp^2 carbon atoms. They can form tubes, sheets, spheres or various other geometric forms. Carbon nanotubes (CNT) and graphene, which are single layer sheets, have gained most prominence in

biomedical research due to their interesting physicochemical properties[20, 21]. CNT can either be single walled (SWCNT) or multiwalled (MWCNT) with diameters ranging from 0.8-2 nm and 2-100 nnm respectively. They have young's modulus of 0.27-1.34 TPa and tensile strength of 11-200 GPa[20]. When incorporated into polymeric matrix, they can significantly increase mechanical properties of the nanocomposites by up to 36-42%. It is this property of these nanoparticles that make it so attractive for tissue engineering applications. They can be incorporated into biocompatible polymers that have poor mechanical properties and used for bone tissue engineering applications[22]. Furthermore, CNT have very strong absorbance of ~0.99 from far ultraviolet to far infrared, making them highly suitable as PA agents[23, 24]. They have PA intensity 6 times higher than blood when stimulated with near infrared light making them ideal as *in vivo* contrast agents [25]. Therefore, in Aim 2, we will utilize CNT as a PA contrast agent to visualize tissue engineering scaffolds *in-vivo.*

Even though CNT is an excellent PA agent and could be used for PA stimulation for bone regeneration *in vivo*, graphene nanoparticles are better suited for applications in bone tissue engineering. Graphene are 2-dimensional single sheet of conjugated sp^2 carbon atoms with various geometric shapes. It is the thinnest, strongest and stiffest material currently known to man [26] with young's modulus of 1TPa and tensile strength of 130 GPa [27]. Graphene incorporated into polymeric matrix not only enhances mechanical properties of bone tissue engineering scaffolds[22] but also enhances cell adhesion, proliferation and stem cell differentiation [21, 28, 29]. To develop graphene as PA agents for enhancing bone tissue regeneration in tissue engineering scaffolds we must first determine its effects on viability and differentiation of mesenchymal stem cells which are crucial for tissue regeneration *in vitro*.

Preliminary data

In vitro PA stimulation enhances osteodifferentiation of mesenchymal stem cells

We have previously studied the effect of carbon nanotube (SWCNT) enhanced PA stimulation on differentiation of mesenchymal stem cells (MSCs) grown on poly(lactic-co-glycolic acid) (PLGA) films *in vitro*[30]. For the experimental groups (Table 1), MSCs seeded onto glass coverslips (Light), PLGA films (PLGA) or PLGA-SWCNT films (PLGA-SWCNT) were stimulated for 10 minutes/day with a 527nm Nd:YLF laser (200ns pulse duration, 10 Hz repetition rate) consecutively for 4, 9 and 15 days. The controls included baseline controls like experimental groups without PA stimulation and one positive control (Dex) in which the MSCs were cultured with osteogenic supplement media. We performed alkaline phosphate (ALP), calcium and osteopontin (OPN) assays and alizarin red staining to determine differences in osteogenic differentiation between the groups.

The stimulated groups showed significantly higher calcium content, whereas the non-stimulated controls, except for positive control, Dex, had negligible levels of calcium throughout the experiment ($p<0.05$) (Figure 1). By day 15, PLGA-SWCNT samples had a 131 %, 146%, and 347% greater calcium expression than PLGA, Light, and Dex respectively. At all three time points the positive control, Dex, had similar trends but lower levels of calcium than the PA stimulated groups. These results were congruent with alkaline phosphate and osteopontin assays along with the qualitative alizarin red staining of the extracellular matrix. The stimulated PLGA-SWCNT group had 10% higher ALP activity compared to stimulated PLGA group and 65% higher activity compared to light control ($p<0.05$) (Figure 2). OPN secretion was 6 to 7-fold higher in the PA stimulated Light, PLGA and PLGA-SWCNT groups compared to the positive control following 15 days of stimulation ($p<0.05$) (Figure 3). Further, PA stimulated PLGA-SWCNT group had 11% and 22% higher OPN content compared to PA stimulated Light and

PLGA groups respectively at day 15. These results indicate that PA stimulation holds promise for bone tissue engineering, and that nanomaterials that enhance the PA effect should allow development of biophysical rather than biochemical strategy to induce osteoinductive properties [30].

O-SWGNR produce the highest intensity PA signal

Oxidized graphene nanoribbons (GNR) made from single walled carbon nanotubes (O-SWGNR) was chosen to make the PA enhancing films because of its excellent PA properties. We investigated the PA signal generated when various carbon nanoparticles are stimulated with pulsed light of varying wavelengths[31]. The results indicate GNR have the highest PA intensity (Figure 5) compared to single-and-multi walled carbon nanotubes, micro-graphite flakes, oxidized graphite microparticles, and exfoliated graphene nanoplatelets. Furthermore, O-SWGNR had the higher PA intensity compared to GNR made from multi walled carbon nanotubes (O-MWGNR)[31]. Cell adhesion, proliferation and viability of fibroblasts and preosteoblasts were not affected when O-SWGNRs were incorporated into polymeric nanocompsites *in vitro[32]*. Dispersions of the particles themselves do not affect viability or differentiation of mesenchymal stem cells[30] *in vitro* (Chapter 2). Therefore, if GNR were to be used for *in vivo* applications, nanoparticles released from degraded scaffolds is not expected to have any toxic effects at low concentrations. Due to its high intensity PA generation and relatively low toxicity compared to other carbon nanoparticles, GNR were chosen to prepare carbon nanoparticle films for PA stimulation in Chapter 4.

Global Objective

The overall goal of this thesis is to develop carbon nanoparticle enhanced photoacoustic stimulation (CEPS) for bone tissue engineering. We believe carbon nanoparticle incorporated nanocomposite scaffolds, when stimulated by PA, could be an ideal solution for treating critical sized bone defects. It would enhance fracture healing while subsequently allow detection and monitoring by PA imaging. Towards this end, we investigate three separate components of CEPS that would eventually lead to its development for use in pre-clinical or clinical applications. As a proof of concept investigation, we seek to answer the following questions:

1) Do carbon nanoparticles affect normal cellular activity of stem cells crucial to bone tissue engineering?
2) Can PA imaging be used to detect and monitor tissue engineering scaffolds *in vivo*?
3) Does PA stimulation enhance healing in bone *in vivo*?

To answer these questions we designed the following aims:

Aim 1: Investigate the effect of graphene nanostructures on stem cells

Hypothesis: Graphene nanoparticles do not affect viability and differentiation of mesenchymal stem cells at low concentrations.

Carbon nanoparticles with varying synthesis and morphologies give them complex physicochemical properties. To develop them for tissue engineering applications we need to first investigate their interaction with cells crucial to tissue engineering. In this aim, we will treat bone derived (bmMSCs) and adipose derived stem cells (adMSCs) with 0-300 μg/ml concentrations of graphene with three different morphology: nanoonions (GNO), nanoplatelets (GNP) and nanoribbons (GNR) for 1 and 3 days. We will determine viability of treated groups with

Alamarblue and Calcien AM assays compared to untreated controls. Effect of treatment with GNO, GNP and GNR on osteo-and-adipogenic differentiation of adMSCs, following 24 hour treatment with 10 or 50 μg/ml dispersions, will be assessed by alkaline phosphatase activity, matrix calcium content and alizarin red staining for osteogenesis; and oil red o staining and elution for adipogenesis. Uptake of nanoparticles by adMSCs will be assessed by confocal raman and TEM.

Aim 2: Investigate PA imaging of tissue engineering scaffolds

Hypothesis: Carbon nanoparticle incorporated polymeric scaffolds have significantly higher PA intensity and can be delineated from surrounding tissue in PA images

Carbon nanoparticles have previously been shown to have strong PA intensity. Incorporating these particles in polymeric scaffolds would therefore allow for detection with PA imaging modality. The goal of this aim is to determine the strengths and weaknesses of carbon nanoparticle enhance photoacoustic imaging for bone tissue engineering applications. To this end, we will image PLGA and SWCNT-PLGA scaffolds with mutlimodal ultrasound and PA imaging (US-PA) *ex vivo,* in chicken breast tissue, at varying depths and stimulation wavelengths. We will then implant PLGA and SWCNT-PLGA scaffolds in subcutaneous pockets of wistar rats and image them *in vivo* 7 and 14 days post surgery. PA intensity within the scaffolds and oxygen saturation in and around the scaffolds will be compared between the groups. Following euthanasia, the scaffolds and surrounding tissue will be resected and analyzed by histology.

Aim 3: Investigate the effect of carbon nanoparticle enhanced PA on an *in vivo* rat fracture model

Hypothesis: Daily stimulation of fractures with PA will increase bone healing in rats

PA stimulation has never been investigated for applications in tissue engineering. In this aim, we will test its effect of healing closed transverse fracture in the femur of Sprague dawley rats. We will place carbon nanoparticle films on the skin surface directly above the fracture site and stimulate with PA. Stimulations will be provided with near infrared (NIR) laser at 20kHz repetition rate, with 60 ns pulse width, for 10 minutes daily. The quantity and quality of bone formation within the callus will be analyzed by microCT and histology at the end of 2 weeks.

References

[1] Kumar VA, . Abul; Aster, Jon. Bones, joints, and soft tissue tumors. Robbins Basic Pathology2013. p. 765.

[2] Creevey W, DeCoster TA, Prokuski L, Sirkin MS, Ziran B, Henley B, et al. Fracture and Dislocation Classification Compendium-2007. J Orthop Trauma. 2007;21:S1-S133.

[3] Velasco MA, Narváez-Tovar CA, Garzón-Alvarado DA. Design, Materials, and Mechanobiology of Biodegradable Scaffolds for Bone Tissue Engineering. BioMed research international. 2015;2015.

[4] Stevens MM. Biomaterials for bone tissue engineering. Materials today. 2008;11:18-25.

[5] AlGhamdi A, Shibly O, Ciancio S. Osseous grafting part II: xenografts and alloplasts for periodontal regeneration--a literature review. Journal of the International Academy of Periodontology. 2010;12:39-44.

[6] Oryan A, Alidadi S, Moshiri A, Maffulli N. Bone regenerative medicine: classic options, novel strategies, and future directions. J Orthop Surg Res. 2014;9:18.

[7] Stock UA, Vacanti JP. Tissue engineering: current state and prospects. Annual review of medicine. 2001;52:443-51.

[8] Badylak SF, Weiss DJ, Caplan A, Macchiarini P. Engineered whole organs and complex tissues. The Lancet. 2012;379:943-52.

[9] Lysaght MJ, Hazlehurst AL. Tissue engineering: the end of the beginning. Tissue engineering. 2004;10:309-20.

[10] Lanza R, Langer R, Vacanti JP. Principles of tissue engineering: Academic press; 2011.

[11] Bohner M. Resorbable biomaterials as bone graft substitutes. Materials Today. 2010;13:24-30.

[12] Logeart-Avramoglou D, Anagnostou F, Bizios R, Petite H. Engineering bone: challenges and obstacles. J Cell Mol Med. 2005;9:72-84.

[13] Qin Y-X, Hu M. Mechanotransduction in musculoskeletal tissue regeneration: Effects of fluid flow, loading, and cellular-molecular pathways. BioMed research international. 2014;2014.

[14] Zhuang J, Kuo C-H, Chou L-Y, Liu D-Y, Weerapana E, Tsung C-K. Optimized Metal–Organic-Framework Nanospheres for Drug Delivery: Evaluation of Small-Molecule Encapsulation. ACS nano. 2014;8:2812-9.

[15] Tam AC. Applications of photoacoustic sensing techniques. Reviews of Modern Physics. 1986;58:381.

[16] Xu M, Wang LV. Photoacoustic imaging in biomedicine. Review of scientific instruments. 2006;77:041101.

[17] Wang LV, Hu S. Photoacoustic tomography: in vivo imaging from organelles to organs. Science. 2012;335:1458-62.

[18] Wang LV. Multiscale photoacoustic microscopy and computed tomography. Nature photonics. 2009;3:503-9.

[19] Talukdar Y, Avti P, Sun J, Sitharaman B. Multimodal ultrasound-photoacoustic imaging of tissue engineering scaffolds and blood oxygen saturation in and around the scaffolds. Tissue Engineering Part C: Methods. 2014;20:440-9.

[20] Hopley EL, Salmasi S, Kalaskar DM, Seifalian AM. Carbon nanotubes leading the way forward in new generation 3D tissue engineering. Biotechnology advances. 2014;32:1000-14.

[21] Dubey N, Bentini R, Islam I, Cao T, Neto AHC, Rosa V. Graphene: A Versatile Carbon-Based Material for Bone Tissue Engineering. Stem cells international. 2015;2015.

[22] Lalwani G, Henslee AM, Farshid B, Lin L, Kasper FK, Qin YX, et al. Two-dimensional nanostructure-reinforced biodegradable polymeric nanocomposites for bone tissue engineering. Biomacromolecules. 2013;14:900-9.

[23] Mizuno K, Ishii J, Kishida H, Hayamizu Y, Yasuda S, Futaba DN, et al. A black body absorber from vertically aligned single-walled carbon nanotubes. Proceedings of the National Academy of Sciences. 2009;106:6044-7.

[24] Yang Z-P, Ci L, Bur JA, Lin S-Y, Ajayan PM. Experimental observation of an extremely dark material made by a low-density nanotube array. Nano letters. 2008;8:446-51.

[25] Pramanik M, Swierczewska M, Green D, Sitharaman B, Wang LV. Single-walled carbon nanotubes as a multimodal-thermoacoustic and photoacoustic-contrast agent. Journal of biomedical optics. 2009;14:034018--8.

[26] Geim AK, Novoselov KS. The rise of graphene. Nature materials. 2007;6:183-91.

[27] Lee C, Wei X, Kysar JW, Hone J. Measurement of the elastic properties and intrinsic strength of monolayer graphene. science. 2008;321:385-8.

[28] Lee WC, Lim CHY, Shi H, Tang LA, Wang Y, Lim CT, et al. Origin of enhanced stem cell growth and differentiation on graphene and graphene oxide. ACS nano. 2011;5:7334-41.

[29] Kalbacova M, Broz A, Kong J, Kalbac M. Graphene substrates promote adherence of human osteoblasts and mesenchymal stromal cells. Carbon. 2010;48:4323-9.

[30] Talukdar Y, Rashkow JT, Lalwani G, Kanakia S, Sitharaman B. The effects of graphene nanostructures on mesenchymal stem cells. Biomaterials. 2014;35:4863-77.

[31] Lalwani G, Cai X, Nie L, Wang LV, Sitharaman B. Graphene-based contrast agents for photoacoustic and thermoacoustic tomography. Photoacoustics. 2013;1:62-7.

[32] Farshid B, Lalwani G, Sitharaman B. In vitro cytocompatibility of one-dimensional and two-dimensional nanostructure-reinforced biodegradable polymeric nanocomposites. Journal of Biomedical Materials Research Part A. 2015;103:2309-21.

Tables

Table 1. Summary of experimental groups showing either the presence or absence of the respective components[30].

S.No	Experimental Group	PLGA Film	SWCNTs	Osteogenic Media	PA Stimulation Performed
1	Light	No	No	No	Yes
2	PLGA	Yes	No	No	Yes
3	PLGA-SWCNT	Yes	Yes	No	Yes
4	Light Control	No	No	No	No
5	PLGA Control	Yes	No	No	No
6	PLGA-SWCNT Control	Yes	Yes	No	No
7	Dex	No	No	Yes	No

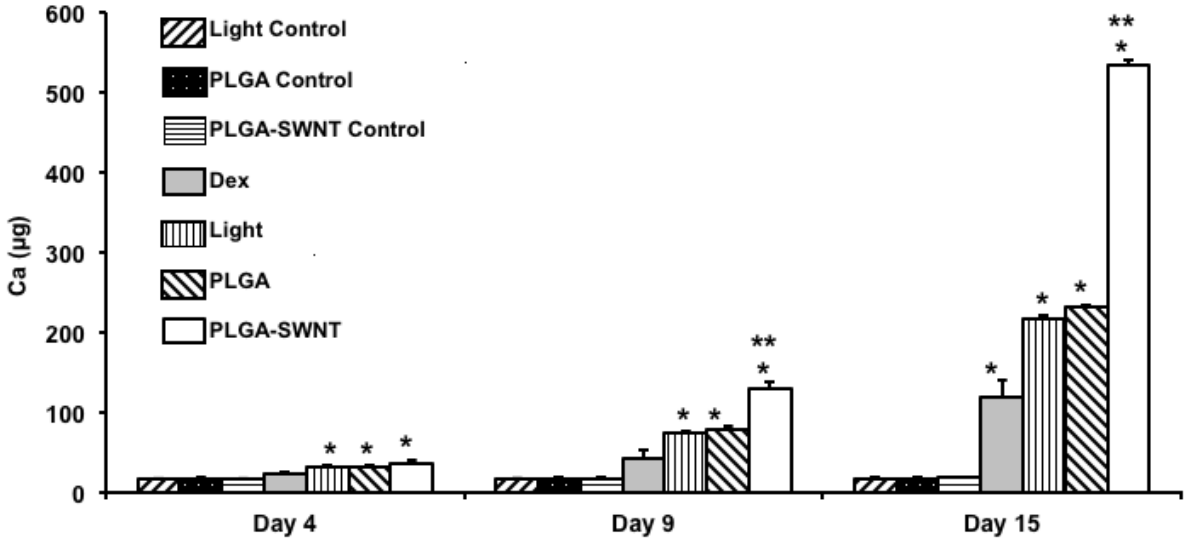

Figures

Figure 1: Quantitative analysis of calcium matrix deposition of MSCs following 4, 9, and 15 days in culture with or without PA stimulation[30].

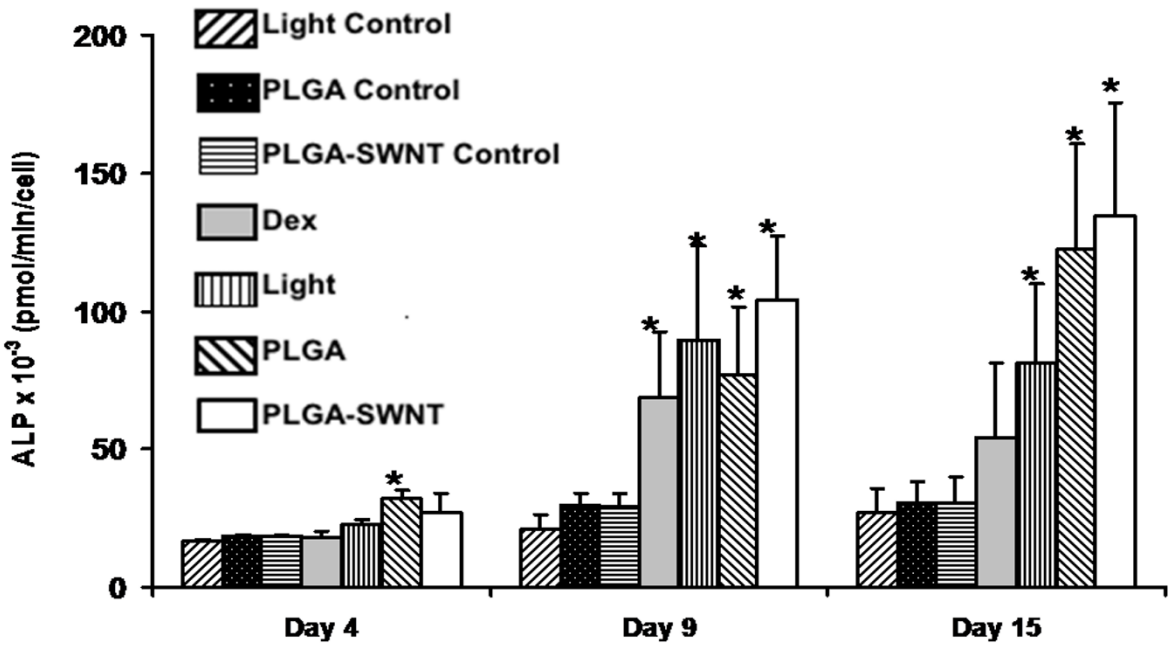

Figure 2: Quantitative analysis of alkaline phosphatase activity (ALP) of MSCs grown on glass cover slips (Light), PLGA or PLGA-SWCNT scaffolds following 4, 9, and 15 days in culture with or without PA stimulation[30].

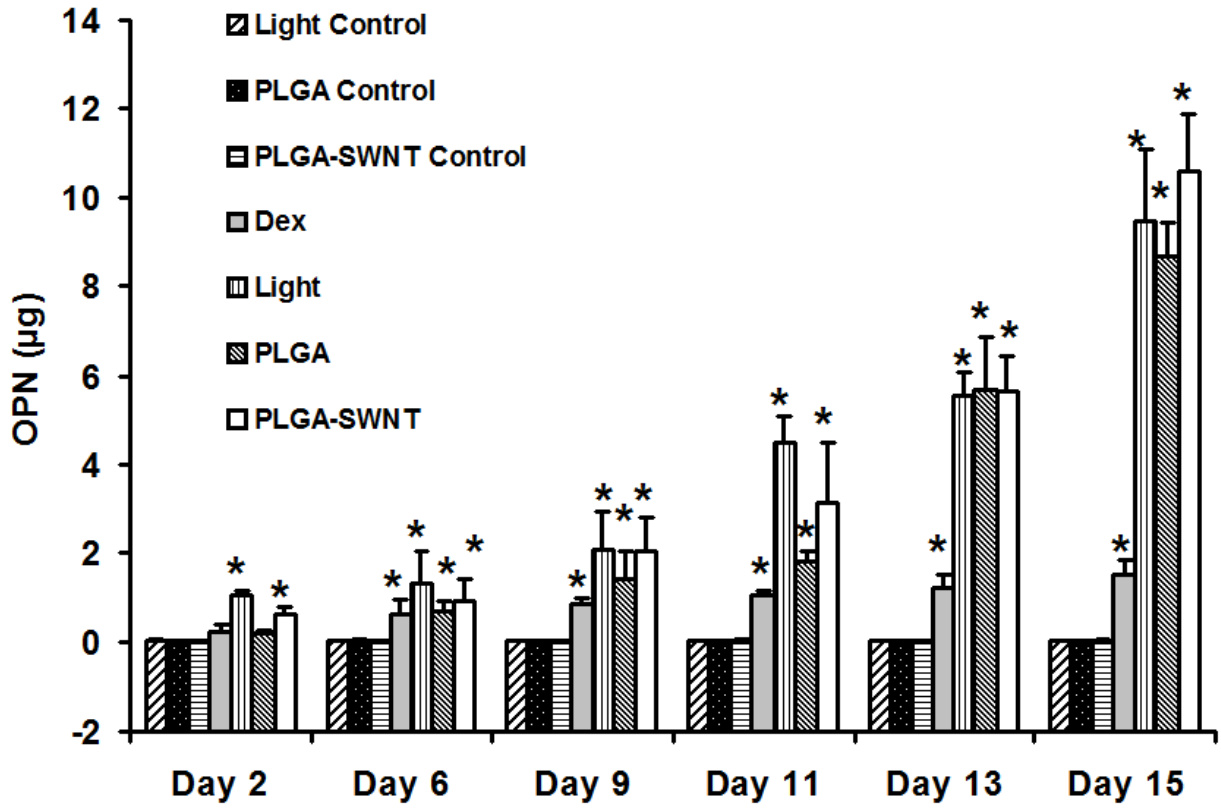

Figure 3: Quantitative analysis of osteopontin in culture media of MSCs grown on glass cover slips (Light), PLGA or PLGA-SWCNT scaffolds following 4, 9, and 15 days in culture with or without PA stimulation[30].

Figure 4: Alizarin red optical images from left to right, PA stimulated PLGA-SWNT (PLGA-SWNT), PA stimulated PLGA (PLGA), osteogenic supplemented control (Dex), PA stimulated direct light (Light). Circle diameters correspond to 15 mm[30].

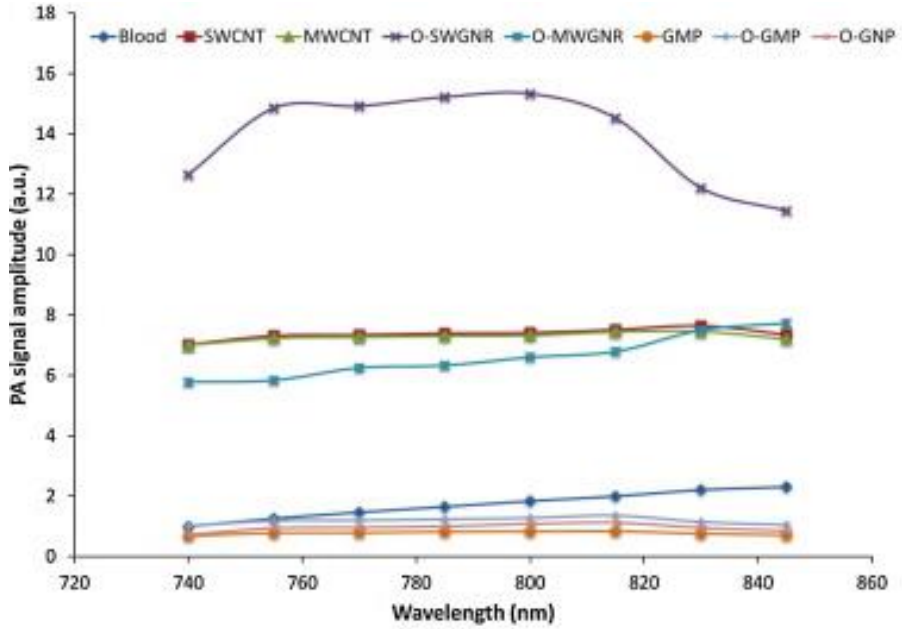

Figure 5: PA spectra of blood, single-walled carbon nanotubes (SWCNTs), multi-walled carbon nanotubes (MWCNTs), oxidized single-walled graphene nanoribbons (O-SWGNRs), oxidized multi-walled graphene nanoribbons (O-MWGNRs), micro-graphite flakes (GMPs), oxidized graphite microparticles (O-GMPs), and exfoliated graphene nanoplatelets (O-GNPs). PA signal amplitudes are normalized to that of blood at 740 nm[31].

Chapter 2: Investigate the effect of Graphene Nanostructures on Mesenchymal Stem Cells

Portions of this chapter have been reproduced from:

Yahfi Talukdar, Jason T. Rashkow, Shruti Kanakia, Balaji Sitharaman. “The effects of graphene nanostructures on mesenchymal stem cells.” *Biomaterials*. 2014;35(18):4863-77.

*The authors listed in the above manuscript have contributions towards data reported in this chapter

Abstract

We report the effects of two-dimensional graphene nanostructures; graphene nano-onions (GNOs), graphene oxide nanoribbons (GONRs), and graphene oxide nanoplatelets (GONPs) on viability, and differentiation of human mesenchymal stem cells (MSCs). Cytotoxicity of GNOs, GONRs, and GONPs dispersed in distearoyl-sn-glycero-3-phosphoethanolamine-N-[amino(polyethylene glycol)] (DSPE-PEG), on adipose derived mesenchymal stem cells (adMSCs), and bone marrow-derived mesenchymal stem cells (bmMSCs) was assessed by AlamarBlue and Calcein AM viability assays at concentrations ranging from 5-300 μg/ml for 24 or 72 hours. Cytotoxicity of the 2D graphene nanostructures was found to be dose dependent, not time dependent, with concentrations less than 50 μg/ml showing no significant differences compared to untreated controls. Differentiation potential of adMSCs to adipocytes and osteoblasts,--characterized by Oil Red O staining and elution, alkaline phosphatase activity, calcium matrix deposition and Alizarin Red S staining-- did not change significantly when treated with the three graphene nanoparticles at a low (10 μg/ml) and high (50 μg/ml) concentration for 24 hours. Transmission electron microscopy (TEM) and confocal Raman spectroscopy indicated cellular uptake of only GNOs and GONPs. The results lay the foundation for the use of these nanoparticles at potentially safe doses as *ex vivo* labels for MSC-based imaging and therapy.

Introduction

Carbon nanoparticles such as zero dimensional (0D) fullerene, one dimensional (1D) carbon nanotubes, and recently two dimensional (2D) graphene [1] have been investigated for applications in therapeutics [2-5], bioimaging [6-8], and regenerative medicine [9]. Mesenchymal stem cells (MSCs) are an important class of adult or somatic stem cells, found in various tissues including bone marrow and adipose tissue. MSCs are multipotent cells that differentiate readily into osteocytes, chondrocytes, or adipocytes; express phenotypic characteristics of endothelial, neural, smooth muscle, skeletal myoblasts, and cardiac myocyte cells; and support hematopoietic stem cells or embryonic stem cells in culture [10-12]. MSC therapies are currently being widely investigated to repair, regenerate, and restore damaged tissues [13, 14], with some of these therapies in clinical trials [15, 16].

Nanoparticles have been employed to deliver growth factors/genes into MSCs to manipulate their differentiation [17, 18]. They have also been used as contrast agents/nanoprobes for stem cell tracking [19, 20] to locate the site of stem cell activity, and determine the efficacy of the therapy. Recent reports have indicated that graphene nanoparticles show excellent efficacy as delivery agents of genes and biomolecules as well as multimodal imaging agents [21-23], and thus could be suitable as multifunctional agents for MSC imaging and therapy.

The development of graphene nanoparticles for MSC applications necessitates thorough examination of their effects and interactions with these cells to identify the potential therapeutic doses. To date, very few studies have investigated the cytotoxicity of graphene nanoparticle formulation with specific focus on progenitor cells, or MSCs [24, 25]. Zhang et. al. examined the toxicity of graphene quantum dots (GQDs), single reduced graphene sheets with diameters in the range of 5 to 10 nm, on three progenitor cell types: neurospheres cells, pancreas progenitor cells, and cardiac progenitor cells [24]. Akhavanet. al. employed umbilical cord-derived MSCs and

investigated the size-dependent cytotoxicity of graphene oxide nanoplatelets and reduced graphene oxide nanoplatelets (prepared using the modified Hummer's method) [25].

Graphene nanoparticles, depending on the synthesis method, can exhibit different morphologies, chemical properties, and physical properties. Graphene nano-onions (GNOs) are spherically shaped concentric layers of graphene. Graphene nanoribbons (GONRs), synthesized using multiwalled carbon nanotubes, are ribbon-shaped graphene stacks. Graphene nanoplatelets (GONPs), synthesized using graphite as the starting material, are disc-shaped multi-layered graphene. Reports indicate that graphene nanoparticles, depending on their morphology and synthesis method, show diverse responses on cells and tissues [26-29]. Thus, it is necessary to systematically investigate the effects that graphene nanoparticles with different morphologies, synthesized by various methods, have on MSC viability and differentiation. In this study, the dose- and time- dependent effects were investigated of three graphene nanoparticles-- GNOs, GONRs, and GONPs-- which were water-dispersed with 1,2-distearoyl-sn-glycero-3-phosphoethanolamine-N-[amino(polyethylene glycol)] (DSPE-PEG), on the viability and differentiation of human MSCs.

Materials and Methods

1 Nanoparticle Synthesis and Characterization

2.1.1 Synthesis of nanomaterials

GNOs were purchased from Graphene Laboratories Inc. (NY, USA). GONRs were synthesized from multi-walled carbon nanotubes (MWCNTs) possessing outer diameters between 20-30 nm (Cat. No. 636487, Sigma Aldrich, New York, USA) using a modified longitudinal unzipping method [30]. GONPs were synthesized from graphite flakes using a modified Hummer's method [21]. Nanoparticles were dispersed in a 1.2 mg/ml solution of DSPE-PEG and bath sonicated for 1 hour to ensure homogenous stable dispersions before treating the cells.

1.2 Raman spectroscopy

Raman spectroscopy was performed using a WITec alpha300R Micro-Imaging Raman Spectrometer equipped with a 532 nm Nd-YAG excitation laser. Spectra were recorded between 50 -3750 cm^{-1} at room temperature.

1.3 Transmission electron microscopy

Nanomaterials were dispersed in ethanol:water (1:1) by probe sonication (Cole Parmer Ultrasonicator LPX 750) using a 1 sec "on", 2 sec "off" cycle. The samples were subjected to ultracentrifugation (5000 rpm for 5 minutes), and the supernatant was dropped onto lacey carbon grids (300 mesh size, copper support, Ted Pella, USA). HRTEM imaging was performed using a JOEL 2100F high-resolution analytical transmission electron microscope at the Center for Functional Nanomaterials, Brookhaven National Laboratory, New York. Samples were imaged at an accelerating voltage of 200 kV.

1.4 Thermogravimetric analysis

Thermogravimetric analysis (TGA) was performed on GNOs, GONRs, and GONPs using a Perkin-Elmer Diamond 500 (Waltham, MA, USA) instrument at the Center for Functional Nanomaterials, Brookhaven National Laboratory, New York. The samples were heated from 50^{o}C to 800^{o}C with the heating rate of 10^{o}C /min under the argon flow of 20 ml/min.

1.5 Zeta potential and hydrodynamic diameter

Zeta potential and hydrodynamic diameter of GNOs, GONRs, and GONPs dispersed in DSPE-PEG was measured at 25^{o}C using Malvern Zetasizer Nano ZS instrument at the Center for Functional Nanomaterials, Brookhaven National Laboratory, New York. The electrophoretic mobility values were calculated based on three separate measurements of 20 runs each. The zeta potential values were calculated from the electrophoretic mobility by the software using the Helmholtz-Smoluchowski equation. The hydrodynamic diameter of nanoparticles was calculated by measuring the velocity of particles under Brownian motion using the Stokes-Einstein equation.

2.2 Cell Culture

Adult human MSCs were isolated from lipoaspirate (Lifeline Cat No. FC-0034) and normal bone marrow (Lonza Cat NO. PT-2501). StemLife^{TM} MSC medium (Lifeline, Cat No. LL-0034) was used for cell cultures, with a media change every 2-3 days. The cells were incubated at 37° C and 5% CO_2 throughout the experiment. Passages 4 through 8 were used for the studies.

2.3 Viability

Adipose-derived human MSCs (adMSCs) and bone marrow-derived MSCs (bmMSCs) were used for the viability studies. Cells were plated in 96-well plates with 5000 cells/well. Twenty-four hours after plating, the cells were treated with a 10% volume of DSPE-PEG (control), or of

GNOs, GONRs, and GONPs concentrations at 0 μg/ml, 5 μg/ml, 10 μg/ml, 50 μg/ml, 100 μg/ml and 300 μg/ml. Viability was assessed 24 or 72 hours after treatment with alamarBlue and Calcein AM assays.

2.4 AlamarBlue

Viability of adMSCs and bmMSCs treated with various concentrations (0-300 μg/ml) of graphene nanoparticles was determined using an alamarBlue assay. Untreated cells were used as a positive control. Cells treated with ice-cold methanol were used as a negative control. Twenty-four or 72 hours after treatment, the culture media were removed from the wells. After washing the wells with phosphate buffer solution (PBS), 100 μl of media were added. Ten μl of alamarBlue (Life Technologies, St. Louis, MO, USA) reagent was added to the wells. After incubating for two hours, fluorescence was measured at an excitation wavelength of 530 nm and emission wavelength of 580 nm.

2.5 Calcein AM

Viability of cells treated with different concentrations (0-300 μg/ml) of graphene nanoparticles was evaluated with a Calcein AM assay. At each time point, culture media were removed, and each well was washed with 100 μl of PBS to remove nanoparticles. Next, the PBS was completely removed and 100 μl of 0.05% Calcein AM reagent was added to each well and incubated for 30 minutes at room temperature. The fluorescence was measured at an excitation wavelength of 485 nm and an emission wavelength of 530 nm.

2.6 Adipogenic differentiation

Adipose-derived MSCs (adMSCs) were used for the differentiation studies. adMSCs were plated in 24-well plates at a density of 20,000 cells/well. The cells were treated with DSPE-PEG and either 10 μg/ml or 50 μg/ml of GNOs, GONRs, or GONPs. After incubation with the

nanoparticles for 24 hours, the wells were washed with PBS to remove nanoparticles and treated with adipogenic and osteogenic differentiation media (Lonza, Cat No. PT-3004 & PT-3002). For adipogenic differentiation, the wells were treated with three rounds of adipogenic induction media, three days each round, and then incubated with the adipogenic maintenance media for a total of 21 days, with a media change every three days. Adipogenic differentiation was characterized with Oil Red O staining and elution and quantification of this dye. For osteogenic differentiation, the cells were treated with the osteogenic media for 14 days. Alizarin red S staining, alkaline phosphatase activity, and calcium matrix deposition were analyzed as markers of osteogenic differentiation.

2.7 Oil Red O

A well-established protocol was used for staining triglycerides and esters within the cells. Oil Red O stain was used to determine differences in adipogenic differentiation between the groups [31]. After incubation, the culture media were removed from the wells, and the cells were washed with PBS. The wells were then treated with 1 ml of 4% paraformaldehyde solution for 10 minutes, followed by 60 minutes of incubation with 1ml of fresh 4% paraformaldehyde solution. The paraformaldehyde was then removed, and the cells were washed with water, followed by a 60% isopropanol solution. After drying at room temperature, the wells were filled with a 0.5ml Oil Red O working solution made of two parts Oil Red O stock solution (0.35% solution in isopropanol) with three parts isopropanol. The wells were then incubated for 10 minutes. Excess Oil Red O dye was removed by incubating with a 100% isopropanol solution for 10 minutes. The wells were then washed immediately with double-distilled water four times. They were then imaged using a BX-51 Olympus microscope (Hamburg, Germany). The concentration of Oil Red O dye eluted was quantified by optical absorbance (wavelength = 500 nm). Optical absorbance of elute from each well was measured in triplicates (Varioskan Flash, Thermo Electron, Finland) and compared to the 100% isopropanol controls.

2.8 Osteogenic differentiation

2.8.1 Alizarin Red S

The well-established Alizarin Red S staining method was used to characterize a mineralized matrix due to osteodifferentiation of adMSCs[32]. Alizarin Red S solution (40 mM) was prepared in water and adjusted to a pH of 4.1 using 0.5 N ammonium hydroxide. After incubation with differentiation media, media were removed from the wells and the cells were washed with PBS. The cells were fixed using 1 ml of a 4% paraformaldehyde solution for 15 minutes. After fixation, the wells were washed twice with deionized water, and 1 ml of Alizarin Red S was added to each well. Following 20 minutes of incubation with light shaking, the wells were washed four times with deionized water while shaking for five minutes. The wells were imaged using a BX-51 Olympus microscope (Hamburg, Germany).

2.8.2 Cellularity

The number of cells per well was determined using QuantiFluor Dye Systems (Promega, WI, USA). A standard curve of double-stranded DNA was used to determine DNA content in each well. Subsequently, a standard curve of a known number of adMSCs was used to determine the number of cells per well corresponding to the calculated DNA content. 100 µl of sample or standard were added to a 96-well plate. 100 µl of 1x TE buffer were added with 100 µl of a QuantiFluor dye working solution. The 96-well plate was incubated in the dark at room temperature for 10 minutes. Fluorescence for each well was measured at an excitation wavelength of 480 nm and an emission wavelength of 570 nm. Data are presented as number of cells per well.

2.8.3 Alkaline Phosphatase activity

The ALP activity for the cells was measured using a well-established protocol utilizing the conversion of *p*-nitrophenylphosphate (pNPP) to *p*-nitrophenolate [33]. To perform this assay, cells in a 24-well plate were washed with PBS, and 2 ml of fresh PBS were added. These cells were then lysed by sonication for 30 minutes. 100 µl of pNPP were added to the cell lysate, placed in a 96-well plate in triplicates, and incubated at 37°C for one hour. After incubation, 100 µl of NaOH stop solution was added to each well, and absorbance was measured at 405 nm (Varioskan Flash, Thermo Electron, Finland). Data are presented as ALP activity in µmol per minute per cell.

2.8.4 Calcium Matrix Deposition

Arsenazo III Calcium Assay was used to determine calcium matrix deposition [34]. 100 µl of cell lysate were placed in triplicates in a 96-well plate with an equal volume of 1 M acetic acid. After overnight incubation, 20 µl of solution from each well or calcium chloride standard was added to 280 µl of Arsenazo III Calcium Assay reagent in a 96-well plate. Absorbance was measured at 650 nm wavelength (Varioskan Flash, Thermo Electron, Finland).

2.9 Nanoparticle uptake

2.9.1 Transmission Electron Microscopy

Histological specimens for transmission electron microscopy (TEM) were prepared by standard techniques. Briefly, adMSCs were cultured on ACLAR embedding film (Electron Microscopy Sciences) and placed in a 6-well plate for 24 hours before being treated with a 10% volume of DSPE-PEG (control) or a 50 µg/ml concentration of GNOs, GONRs, and GONPs for 24 hours. Cells were then washed with PBS and fixed using 1 ml of a 1% glutaraldehyde solution for one hour. After fixation, glutaraldehyde was removed, and a 1% osmium tetroxide solution in 0.1M

PBS was added to the cells. The samples were then dehydrated by graded ethanol washes, and embedded in Durcupan resin (Sigma Life Science, St. Louis, MO). Sections of 80 nm were cut using a Reichert-Jung UltracutE ultramicrotome and placed on formvar-coated slot copper grids. Uranyl acetate and lead citrate were used to counterstain the sections. Samples were viewed with a TEM (JOEL JEM-1400) at 120 kV, and digital images were acquired with a Gatan CCD Digital Camera system and compiled using Adobe Photoshop.

2.9.2 Confocal Raman Microscopy

For investigating cellular uptake of nanoparticles using confocal Raman microscopy, adMSCs were incubated with GNOs, GONRs, and GONPs at 50 μg/ml in glass chamber slides (Nunc Lab-Tek II) for 24 hours. Following incubation, the cells were washed with PBS and fixed with ice-cold methanol. Confocal microscopy images were taken using an excitation laser set at 532 nm on an Alpha combination microscope (WITec, Knoxville, TN). An objective of 100x was used for brightfield images, and area maps were constructed using G-band intensity of GNOs, GONRs, and GONPs respectively.

2.10 Statistics

Cell viability of the treated samples is presented as percentage of live cells compared to untreated cells at one day and three-day time points. CD50 values, or the concentration at which 50% of the cells are viable, were calculated from viability vs. concentration graphs. Statistical significance of the difference in viability after one and three days between the control (PEG-DSPE) stem cells and the nanoparticle-treated stem cells was analyzed by the Kruskal-Wallis test with Dunn post hoc. Differences in differentiation of cells treated with 10 or 50 μg/ml of GNOs, GONRs, or GONPs were analyzed with the Kruskal-Wallis test with Dunn post hoc. All statistics were done using Graph Pad InStat 3 software with comparisons having $p < 0.05$ considered to be significantly different.

Results

3.1 Nanoparticle Characterization

3.1.1 Transmission electron microscopy

TEM images of various nanostructures are presented in Figure 1. GNOs (Figure 1 A) were hollow, multiwalled, and concentric polyhedral structures shaped like onions with diameters in the range of 50-300 nm. Multiwalled GONRs (Figure 1 B) appeared as rectangular sheets with breadths and lengths of ~60-90 nm and 500-1500 nm, respectively. GONPs (Figure 1 C) were disk-shaped with diameters between 20-40 nm and thicknesses between 3-5 nm.

3.1.2 Raman spectroscopy

Representative Raman spectra of all the nanomaterials are presented in Figure 1 D. Peaks at 1335 cm^{-1} (D band), 1576 cm^{-1} (G band), and 2680 cm^{-1} (G' band) were observed for GNOs (Figure 1 D [a]). Peaks at 1340 cm^{-1} (D band) and 1580 cm^{-1} (G band) were observed for GONRs (Figure 1 D [b]), and peaks at 1351 cm^{-1} (D band) and 1604 cm^{-1} (G band) were observed for GONPs (Figure 1D [c]). The I_D/I_G ratios for GNOs, GONRs, and GONPs were 0.92, 1.28, and 1.09, respectively.

3.1.3 Thermogravimetric analysis

Figure 1 E shows TGA spectra of GNOs, GONRs, and GONPs. The TGA spectra of pristine GNOs showed a negligible weight loss of (~0.03%) up to 800°C. The thermal decomposition of GONRs and GONPs can be divided into three temperature zones: 0-100°C, 100-200°C and >200°C. GONRs showed ~10% weight loss and GONPs showed ~6% weight loss in the first temperature zone between 0-100°C. In the second temperature zone between 100-200°C, weight

loss for GONRs and GONPs was ~30% and ~10%, respectively. In the third temperature zone (>200°C), both GONRs and GONPs showed a gradual weight loss of ~25%.

3.1.4 Zeta Potential and hydrodynamic diameter

The zeta potential and hydrodynamic diameter values for GNOs, GONRs, and GONPs are listed in Table 1. All nanomaterials were dispersed in DSPE-PEG and vortexed before measurements to ensure uniformity. The zeta potential values for GNOs, GONRs, and GONPs were -32.3±1.35 mV, -26.30±0.75 mV and -12.47±0.12 mV, respectively. The hydrodynamic diameter for GNOs was 460.76±53.58 nm; for GONRs was 457.5±35.70; and for GONPs was 296.4±20.32 nm.

3.2 Viability

3.2.1 AlamarBlue

AlamarBlue assay works on the basis of conversion of resazurin to fluorescent resorufin by live cells [35]. Figure 3 shows viability of adMSCs (Figure 2 A, B and C) and bmMSCs (Figure 2 D, E and F) treated with GNOs (Figure 2 A and D), GONRs (Figure 2 B and E), and GONPs (Figure 2 C and F) at concentrations ranging from 0-300 μg/ml. The viability of the cells treated with DSPE-PEG alone was ~50% of controls in adMSCs and ~80% in bmMSCs: significantly lower compared to the untreated control. For the groups treated with GNOs, GONRs, and GONPs, viability decreased with increasing concentration. The lowest viability was at a nanoparticle concentration of 300 μg/ml for all groups. Table 2 lists the percentage decrease in viability at day one and day three for adMSCs and bmMSCs treated with 300 μg/ml concentration of GNOs, GONRs, or GONPs. Table 4 lists CD50 values of adMSCs and bmMSCs treated with GNOs, GONRs, and GONPs assessed by alamarBlue assay.

3.2.2 Calcein AM

Calcein AM is used to determine viability of cells by measuring fluorescence of calcein, which is a product of intercellular esterase activity in live cells [36]. Figure 3 displays the cell viability--determined using Calcein AM assay-- on day one and day three of adMSCs (Figure 2 A, B and C) and bmMSCs (Figure 2 D, E and F) treated with GNOs (Figure 3 A and D), GONRs (Figure 3 B and E), and GONPs (Figure 3 C and F) at concentrations between 0-300 μg/ml. For both time points, the viability decreased with increasing nanoparticle concentration, with the lowest viability occurring at 300 μg/ml. Table 3 lists the decrease in viability at day one and day three for adMSCs and bmMSCs treated with a 300 μg/ml concentration of GNOs, GONRs, or GONPs. Table 4 lists CD50 values of adMSCs and bmMSCs treated with GNOs, GONRs, and GONPs assessed by Calcein AM assay.

3.3 Adipogenic differentiation

3.3.1 Oil Red O Staining and Elution

Oil Red O, a fat-soluble diazol dye, stains neutral lipids and cholesteryl esters without staining biological membranes [37]. Figure 4 A shows representative images of adMSCs stained with Oil Red O. The images were taken three weeks post 24 hour incubations with GNOs, GONRs, and GONPs. Fat vacuoles (black arrows, Figure 4 A) could be seen within the cells for all groups (including the control group) in optical microscopy images. Figure 4 B shows Oil Red O stain elution concentrations that allow quantification of adipocytes present in the experimental and controls groups. Elution concentrations showed no significant difference in staining in any of the graphene nanoparticle groups compared to the control.

3.4 Osteodifferentiation

3.4.1 Alizarin Red S

Alizarin Red S is a dye which binds to calcium and is used to detect calcium deposits in the extracellular matrix of cultured cells [38]. Figure 5 shows adMSCs stained with Alizarin Red S to characterize calcium deposition after incubation with GNOs, GONRs, or GONPs at concentrations of 10 and 50 μg/ml for 24 hours, followed by incubation with osteogenic media for 14 days. Red staining (black arrows) of calcium matrix deposition could be observed for all the groups. There was no difference in distribution of the staining pattern between the groups treated with graphene nanoparticles and those untreated. For cells treated with GNOs, traces of the nanoparticles (black circles) are seen in the images (Figure 5). There was a higher amount of nanoparticles with some traces of large aggregates observed in GONR treated cells. Groups treated with GONPs showed visible aggregates of varying sizes. Groups treated with 50 μg/ml of GONPs had large aggregates of nanoparticles with Alizarin Red S staining seen at a distance around these nanoparticles.

3.4.2 Cellularity

DNA content was quantified by QuantiFluor Dye Systems and used to determine cellularity of each group. The number of cells per well was used to calculate the ALP activity in each cell of the different groups. Figure 6 A shows the number of adMSCs per well after 24 hours of incubation with GNOs, GONRs, or GONPs at concentrations of 10 and 50 μg/ml, followed by 14 days of incubation with osteogenic differentiation media. There were ~100,000 cells in each well, with no significant differences between the treated groups or control.

3.4.3 Alkaline Phosphatase

Alkaline Phosphatase (ALP) is an early-stage marker in osteogenesis [39]. Figure 6 B shows ALP activity in adMSCs after 24 hours of incubation with GNOs, GONRs, or GONPs at concentrations of 10 and 50 μg/ml, followed by 14 days of incubation with osteogenic differentiation media. ALP activity between the groups ranged from 3.6×10^{-7} to 2.7×10^{-6} μmoles/min/cell, with no significant difference observed for all groups.

3.4.4 Calcium Matrix Deposition

Matrix calcium content is a late-stage marker of osteogenesis [34]. Figure 6 C shows calcium content per well for adMSCs treated with 10 or 50 μg/ml of GNOs, GONRs, or GONPs for 24 hours, followed by incubation with osteogenic differentiation media for 14 days. The calcium matrix content for all the groups ranged from 2-6 mg/well. At both concentrations, no significant difference in calcium content was found between the experimental and control groups.

3.5 Cell uptake

3.5.1 Transmission Electron Microscopy

The uptake of nanoparticles into the cells was characterized by transmission electron microscopy (TEM). Figure 7 shows representative TEM images of cells incubated with GNOs and GONPs at concentration of 50 μg/ml for 24 hours. No cellular uptake of GONRs was observed. GNOs (yellow arrows, Figure 7 A& B) were found in the cell membrane (red arrow, Figure 7 A) and cytoplasmic vesicles (green arrows, Figure 7 A & B). GNO particles were absent in or around the nucleus (black arrow, Figure 7 A). For cells treated with GONPs (blue arrows, Figure 7 C & D), individual and aggregated nanoparticles were observed in vesicles (green arrows, Figure 7 C & D) throughout the cytoplasm. GONPs were also seen on the nuclear membrane and inside the nucleus (red arrows, Figure 7C).

3.5.2 Confocal Raman Microscopy

The TEM results were corroborated with confocal Raman mapping. G-band intensities of GNOs, GONRs, and GONPs were used to image the uptake of these nanoparticles into cells. Figure 8A displays representative bright-field microscope images showing GNOs (yellow arrows) within the cytoplasm of the cells. Figure 8B-C shows Raman microscopy analysis, confirming these particles as GNOs. Raman spectra of intracellular GNOs showed a red shift of the D- and G-bands compared to spectra of pristine samples shown in Figure 1(a). Many these particles were observed to gather around the nucleus. The bright-field image and Raman map indicate that the GNOs did not penetrate the nuclear membrane. Figure 8D shows bright-field images of adMSCs treated with GONRs. Aggregates of GONRs (yellow arrows) were seen in the extracellular space and embedded on the cell membrane. Figure 8E shows the confocal Raman map confirming the presence of GONRs on the outside of the cells. No characteristic GONR spectrum was noticed inside the cells. Figure 8G shows bright-field images of GONPs (yellow arrows) attached to the cell membrane, as well as within the cytoplasm of the cells. Raman mapping, shown in Figure 8H, confirmed the presence of GONPs within the cells, though there were no distribution patterns. Figure 8I shows the Raman spectra of intercellular GONPs, with a red shift on the D- and G- bands which could be related to their intercellular environment [40, 41].

Discussion

The objective of this study was to investigate the dose and time-dependent effects of aqueous dispersions of GNOs, GONRs, and GONPs on MSCs. Cellular interactions of graphene nanoparticles could depend on several factors, such as morphology (size and shape), surface charge, chemical state (functionalization), particulate state (dispersion), and the number of layers. These factors may also affect the cellular uptake and cytotoxicity [30, 42, 43]. Therefore, graphene nanoparticles with three distinct morphologies (onions – polyhedral spherical; ribbons – longitudinal flat sheets; and platelets – circular stacks of graphene) were included in this study. adMSCs and bmMSCs were chosen since these cells are widely used for tissue engineering applications[44, 45]. Additionally, these cells can be isolated from bone marrow and adipose tissue from patients to maintain biocompatibility and minimize host rejection [46]. The initial cytotoxicity screening, over a broad range of concentrations (0-300 μg/ml) and time points (one and three days), was performed on adMSCs and bmMSCs to identify a range of potentially safe doses. adMSCs were then employed to investigate whether these graphene nanoparticles at a potentially safe low and high dose affect the differential capabilities of MSCs. The cytotoxicity and differentiation studies together allowed identification of the range of doses for the three-graphene nanoparticle formulations that do not elicit any significantly adverse outcomes on the viability and differentiation capabilities of MSCs.

The Raman spectroscopy of GNOs, GONRs, and GONPs are presented in Figure 1 D. All the nanoparticles exhibit characteristic Raman spectra of graphene (presence of D, G, and 2D bands). The D-band is a first order Raman peak, corresponding to the presence of structural defects (disruption of C=C sp^2 domains) in the graphene sheet. The G-band corresponds to the in-plane vibrations of pristine graphene (stretching between carbon-carbon bonds), whereas the G-band corresponds to the number of graphene layers [47]. The D-band, which occurs in the range of 1350 cm^{-1}, is a one-phonon double resonance process [47]. The G-band, at about 2700 cm^{-1}, is a

two-phonon double resonance phenomenon [40, 47]. The ratio of D- and G-band intensities has been routinely used to infer the amount of defects in the sp^2-bonded carbon [48]. Table 1 lists the I_D/I_G ratio for GNOs, GONRs, and GONPs. The I_D/I_G ratio for GNOs was slightly lower than GONRs and GONPs, but higher than pristine graphene sheets, which suggested the presence of structural defects. GONRs and GONPs showed an increased I_D/I_G ratio compared to pristine multi-walled carbon nanotubes and graphite flakes, which indicated the presence of defects attributed to the disruption of the sp^2-bonded carbon due to oxidative unzipping of nanotubes [21, 49].

TGA has been widely used for characterization of carbon-based nanomaterials [49, 50]. As shown in Figure 1 E, the TGA spectra of pristine GNOs showed a negligible weight loss up to 800°C, confirming its high thermal stability and purity. The thermal decomposition of GONRs and GONPs observed between 0-100°C corresponds to the removal of adsorbed water vapor and other volatiles formed during their synthesis. The observed weight loss in the second temperature zone (between 100-200°C) can be attributed to the removal of hydroxyl and carboxylic acid and ester functional groups from the basal plane and edges of the graphene sheets. In the third temperature zone (>200°C), the observed weight loss corresponded to the gradual structural degradation of sp^2 and sp^3 bonded carbon atoms in GONRs and GONPs. A significantly higher weight loss was observed for GONRs and GONPs compared to GNOs, suggesting that the surface of GONRs and GONPs are highly functionalized.

Nanoparticles with a surface charge attract ions of the opposite charge, which form a thin electrical double layer around the surface of the nanoparticles. The electric potential at the boundary of the double layer is known as the zeta potential. As shown in Table 1, the zeta potential values for all the nanoparticles were negative. This can be attributed to the presence of hydroxyl and carboxyl functional groups on the surface of GNOs, GONRs, and GONPs during their synthesis. For colloidal suspension, zeta potential values greater than -30 mV are generally

considered to have good stability. GNO and GONR dispersions in DSPE-PEG showed a zeta potential value of -32.3 ± 1.35 mV and -26.30 ± 0.75 mV, respectively, suggesting good and medium stability. GONP dispersions in DSPE-PEG showed a low zeta potential value of -12.47 ± 0.12 mV, which is too low for electrostatic stabilization. Although zeta potential plays a key role in determining the stability of colloidal dispersions, it does not measure the sizes of nanoparticles or their aggregates in dispersions. Dynamic light scattering is routinely employed for this purpose. This measures the hydrodynamic diameter: the diameter of a hypothetical sphere with a diffusion coefficient like that of the nanoparticle or aggregates in dispersion. The hydrodynamic diameter of GNOs, GONRs, and GONPs (Table 1) dispersed in DSPE-PEG were 460.76 ± 53.58 nm, 457.5 ± 35.70 nm, and 296.4 ± 20.32 nm, respectively. However, graphene particles have an anisotropic shape, so it is difficult to interpret whether the hydrodynamic diameter values refer to individual nanoparticles or their aggregates. Nevertheless, these numbers suggest that GNOs, GONRs, and GONPs dispersed in DSPE-PEG may exist as sub-micron sized aggregates.

The alamarBlue and calcein AM cytotoxicity assays showed a corresponding decrease in viability of both stem cell types with an increasing concentration of nanoparticles. Although the results of the two assays showed similar trends, the viability values for each assay were not similar. This variability is due to differences in how these assays assess viability, which in turn influence their sensitivity. At lower incubation concentrations (5 and 10 μg/ml) for all the graphene nanoparticle groups, the cells were more viable compared to the PEG-DSPE controls. Overall, for all groups, bmMSCs showed higher viability compared to adMSCs. A significant decrease in viability with an increase in time points was not observed consistently. The CD50 values followed the trend GNOs > GONRs > GONPs, and were >50 μg/ml for all three graphene nanoparticles The CD50 values of graphene nanoparticles have been shown to vary greatly based on synthesis methods, size, morphology, surface coatings, and cell types used for those investigations [25, 30, 42, 43]. These studies indicate that concentrations <50 μg/ml are relatively safe for most cell types. Taken

together with the viability results of this study, GNOs, GONRs ,or GONPs with incubation concentrations of ≤50 μg/ml could be potentially suitable for treating adMSCs and bmMSCs.

For differentiation studies, two representative differentiation pathways of MSCs, osteogenesis and adipogenesis, were chosen [51, 52]. adMSC were treated with two concentrations of the GNOs, GONRs, or GONPs: a low concentration of 10 μg/ml that showed near 100% viability at both time points, and a higher concentration of 50 μg/ml that showed >50% viability when compared to groups treated with DSPE-PEG. The assessment of adipogenesis by Oil Red O staining (Figures 4 A and B) indicated no significant differences in absorbance of Oil Red O stain elute for experimental and control groups. Assessment of ALP activity as an early indicator of osteogenesis of adMSCs showed normal levels at both concentrations, 14 days after treatment with GNOs, GONRs, or GONPs [33]. adMSCs treated with 10 μg/ml of GONRs had the highest ALP activity, ~75% compared to the control. However, this increase was not statistically significant. Assessment of calcium content, a late stage indicator of osteogenesis of adMSCs, showed calcium concentrations similar to untreated controls 14 days after treatment with GONPs at both concentrations. adMSCs treated with 50 μg/ml of GNOs or GONRs also showed calcium concentrations similar to untreated controls. Groups treated with 10 μg/ml of GNOs or GONRs showed approximately half the amount of calcium compared to groups treated at the 50 μg/ml concentration or untreated controls, even though the differences were not statistically significant. Alizarin Red S staining of calcium deposits further qualitatively confirms the above quantitative results. ALP is an early stage marker of osteo-differentiation and its activity declines as the matrix matures. In contrast, calcium is a late stage marker of osteodifferentiation, and its activity increases as the matrix matures. Thus, lower levels of ALP activity, combined with lower calcium concentrations for GNOs and GONRs at 10 μg/ml compared to untreated control groups, suggest that the matrix had not completely matured. This assessment is further corroborated by an Alizarin Red S stained histological evaluation.

TEM and confocal Raman microscopy of histological specimens of adMSCs treated with the various graphene nanoparticles showed differences in cellular uptake, and followed the trend GONRs < GNOs <GONPs. GONPs were found in the cytoplasm and nucleus; GNOs in cytoplasmic vacuoles; GONRs were not found within the cells. The red shift in Raman peaks for GNOs and GONPs could be related to their interaction with the intercellular environment [40, 41]. The differential uptake of the various graphene nanoparticle dispersions may be related their distinct size/aspect ratio, surface properties (charge and functional groups), and aggregation states (hydrodynamic diameter); --attributes that could affect their uptake [53, 54]. However, a higher uptake of a graphene nanoparticle cannot be attributed as the main reason for the observed cytotoxicity[55]. As stated above, the CD50 values followed the trend GNOs > GONRs > GONPs, and suggest that GONRs are more cytotoxic compared to GONPs, even though they do not show cellular uptake. Thus, other reasons could also play a role, such as differences in reactive oxygen species (ROS) generation and/or peroxidation of cell membrane lipids by the various graphene nanoparticles [56].

The above results indicate that effects of GNOs, GONPs, and GONRs on MSCs are significantly different from studies with other types of graphene nanoparticles. A study by Zhang et. al. focused on the effects of graphene quantum dots (GQDs) on three progenitor cell types: neurospheres cells, pancreas progenitor cells, and cardiac progenitor cells. Zhang et. al. indicated that after 72 hours, at concentrations in the range of 1 to 200 μg/ml, all three cell types showed viability of at least 50% [24]. The lowest viability was observed with the 200 μg/ml treatment group, with decreases in viability of about 25% to 30% for all three cell types. GQDs also showed no effect on differentiation and proliferation of neurospheres. Akhavanet. al. [25] treated umbilical cord-derived MSCs with graphene nanoplatelets of four sizes: 11 ± 4 nm, 90 ± 37 nm, 418 ± 56 nm, and 3.8 ± 0.4 μm each at concentrations ranging from 0.01 μg/ml to 100 μg/ml. The results showed that the viability of cells incubated with various sizes of graphene oxide

nanoplatelets for 24 hours were both size- and concentration-dependent. The smallest particles (size = 11 ± 4 nm) at a concentration of 100 µg/ml showed >50% reduction in viability. However, their effects on the differentiation of the MSCs were not reported in this study.

Several studies report that *in vitro* cytotoxicity and intracellular uptake mechanisms (such as passive diffusion and endosomal uptake) of nanoparticles are dependent on their surface charge and/or aggregation state [57, 58]. For instance, individually dispersed and small-sized graphene were more toxic than their aggregated counterparts [25, 43]. The results of TEM (Figure 1 A-C), Raman spectroscopy (Figure 1 D), TGA (Figure 1 E), zeta potential, and hydrodynamic diameter (Table 1) measurements of GNOs, GONRs, and GONPs taken together indicated that these graphene nanoparticles not only possess distinctly different morphological features, but also surface properties. Since the differences in cytotoxicity and cellular uptake results observed in this study are due to complex interplay of various physical and chemical properties of GNOs, GONRs, and GONPs, these results cannot be generalized for all graphene-based nanoparticles. More thorough investigations are currently underway to better understand the differences in cellular uptake of various graphene nanoparticles, including their uptake mechanism and the reasons for the observed variation in cell death.

Graphene-based biomaterials are being increasingly investigated for applications in tissue engineering [59-61]. Their high surface area, strong mechanical properties and ability to be functionalized make them suitable for biomaterial developments for tissue engineering applications. When incorporated into polymeric matrix of bone tissue engineering scaffolds they have been show to increase cell adhesion, proliferation and stem cell differentiation[59]. The above results provide guidelines on potentially safe ranges for biomedical applications, which could be further explored for more specific applications such as nanocomposite scaffold development and tissue regeneration in *in vivo*.

Conclusion

GNOs, GONRs, and GONPs elicited a dose-dependent (0-300 µg/ml), but not a time-dependent (24 and 72 hours) cytotoxic response on adMSCs and bmMSCs. For all three nanoparticles, concentrations of less than 50 µg/ml showed no significant differences compared to untreated controls. The adipogenic and osteogenic differentiation potential of adMSCs was not adversely affected after treatment with a low (10 µg/ml) or high (50 µg/ml) concentration. GNOs and GONPs were internalized by adMSCs, while GONRs were not. The results suggest that GNOs, GONRs, and GONPs at concentrations of less than 50 µg/ml for 24 or 72 hours could be considered potentially safe incubation conditions for *ex vivo* labeling for MSCs. The results open avenues for use of these graphene nanoparticle formulations for applications in regenerative medicine.

References:

[1] Xia Y, Yang P, Sun Y, Wu Y, Mayers B, Gates B, et al. One-Dimensional Nanostructures: Synthesis, Characterization, and Applications. Advanced Materials. 2003;15:353-89.

[2] Mendes RG, Bachmatiuk A, Büchner B, Cuniberti G, Rümmeli MH. Carbon nanostructures as multi-functional drug delivery platforms. Journal of Materials Chemistry B. 2013;1:401-28.

[3] Yang K, Hu L, Ma X, Ye S, Cheng L, Shi X, et al. Multimodal Imaging Guided Photothermal Therapy using Functionalized Graphene Nanosheets Anchored with Magnetic Nanoparticles. Advanced Materials. 2012;24:1868-72.

[4] Yang K, Zhang S, Zhang G, Sun X, Lee ST, Liu Z. Graphene in mice: ultrahigh in vivo tumor uptake and efficient photothermal therapy. Nano Letters. 2010;10:3318-23.

[5] Shruti Kanakia, Jimmy Toussaint, Sayan Mullick Chowdhury, Gaurav Lalwani, Tanuf Tembulkar, Terry Button, et al. Physicochemical Characterization of A Novel Graphene-Based Magnetic Resonance Imaging Contrast Agent. International journal of nanomedicine. 2013;In Press.

[6] Lalwani G, Cai X, Nie L, Wang LV, Sitharaman B. Graphene-based contrast agents for photoacoustic and thermoacoustic tomography. Photoacoustics. 2013;1:62-7.

[7] Avti PK, Talukdar Y, Sirotkin MV, Shroyer KR, Sitharaman B. Toward single-walled carbon nanotube-gadolinium complex as advanced MRI contrast agents: Pharmacodynamics and global genomic response in small animals. Journal of biomedical materials research Part B, Applied biomaterials. 2013;101:1039-49.

[8] Kanakia S, Toussaint JD, Chowdhury SM, Lalwani G, Tembulkar T, Button T, et al. Physicochemical characterization of a novel graphene-based magnetic resonance imaging contrast agent. International journal of nanomedicine. 2013;8:2821-33.

[9] Lalwani G, Henslee AM, Farshid B, Lin L, Kasper FK, Qin YX, et al. Two-dimensional nanostructure-reinforced biodegradable polymeric nanocomposites for bone tissue engineering. Biomacromolecules. 2013;14:900-9.

[10] Friedenstein A, Piatetzky-Shapiro I, Petrakova K. Osteogenesis in transplants of bone marrow cells. J Embryol Exp Morph. 1966;16:381-90.

[11] Young RG, Butler DL, Weber W, Caplan AI, Gordon SL, Fink DJ. Use of mesenchymal stem cells in a collagen matrix for Achilles tendon repair. J Orthop Res. 2005;16:406-13.

[12] Smith RKW, Korda M, Blunn GW, Goodship AE. Isolation and implantation of autologous equine mesenchymal stem cells from bone marrow into the superficial digital flexor tendon as a potential novel treatment. Equine Vet J. 2003;35:99-102.

[13] Caplan AI. Mesenchymal stem cells. J Orthopaed Res. 1991;9:641-50.

[14] Shang Q, Wang Z, Liu W, Shi Y, Cui L, Cao Y. Tissue-Engineered Bone Repair of Sheep Cranial Defects with Autologous Bone Marrow Stromal Cells. J Craniofac Surg. 2001;12:586-93.

[15] Kang H-J, Kim H-S, Koo B-K, Kim Y-J, Lee D, Sohn D-W, et al. Intracoronary infusion of the mobilized peripheral blood stem cell by G-CSF is better than mobilization alone by G-CSF for improvement of cardiac function and remodeling: 2-year follow-up results of the Myocardial Regeneration and Angiogenesis in Myocardial Infarction with G-CSF and Intra-Coronary Stem Cell Infusion (MAGIC Cell) 1 trial. Am Heart J. 2007;153:237. e1-. e8.

[16] Janssens S, Dubois C, Bogaert J, Theunissen K, Deroose C, Desmet W, et al. Autologous bone marrow-derived stem-cell transfer in patients with ST-segment elevation myocardial infarction: double-blind, randomised controlled trial. The Lancet. 2006;367:113-21.

[17] Corsi K, Chellat F, Yahia LH, Fernandes JC. Mesenchymal stem cells, MG63 and HEK293 transfection using chitosan-DNA nanoparticles. Biomaterials. 2003;24:1255-64.

[18] Cao X, Deng W, Wei Y, Yang Y, Su W, Wei Y, et al. Incorporating pTGF-β1/calcium phosphate nanoparticles with fibronectin into 3-dimensional collagen/chitosan scaffolds: efficient, sustained gene delivery to stem cells for chondrogenic differentiation. Eur Cell Mater. 2012;23:81-93.

[19] Lee JH, Jung MJ, Hwang YH, Lee YJ, Lee S, Lee DY, et al. Heparin-coated superparamagnetic iron oxide for in vivo MR imaging of human MSCs. Biomaterials. 2012;33:4861-71.

[20] Reddy AM, Kwak BK, Shim HJ, Ahn C, Lee HS, Suh YJ, et al. In vivo tracking of mesenchymal stem cells labeled with a novel chitosan-coated superparamagnetic iron oxide nanoparticles using 3.0T MRI. Journal of Korean medical science. 2010;25:211-9.

[21] Paratala BS, Jacobson BD, Kanakia S, Francis LD, Sitharaman B. Physicochemical Characterization, and Relaxometry Studies of Micro-Graphite Oxide, Graphene Nanoplatelets, and Nanoribbons. PLoS ONE. 2012;7:e38185.

[22] Bao H, Pan Y, Ping Y, Sahoo NG, Wu T, Li L, et al. Chitosan-Functionalized Graphene Oxide as a Nanocarrier for Drug and Gene Delivery. Small. 2011;7:1569-78.

[23] Chen B, Liu M, Zhang L, Huang J, Yao J, Zhang Z. Polyethylenimine-functionalized graphene oxide as an efficient gene delivery vector. J Mater Chem. 2011;21:7736-41.

[24] Zhang M, Bai L, Shang W, Xie W, Ma H, Fu Y, et al. Facile synthesis of water-soluble, highly fluorescent graphene quantum dots as a robust biological label for stem cells. J Mater Chem. 2012;22:7461-7.

[25] Akhavan O, Ghaderi E, Akhavan A. Size-dependent genotoxicity of graphene nanoplatelets in human stem cells. Biomaterials. 2012;33:8017-25.

[26] Wang X, Podila R, Shannahan JH, Rao AM, Brown JM. Intravenously delivered graphene nanosheets and multiwalled carbon nanotubes induce site-specific Th2 inflammatory responses via the IL-33/ST2 axis. International journal of nanomedicine. 2013;8:1733.

[27] Shen J, Hu Y, Li C, Qin C, Ye M. Synthesis of amphiphilic graphene nanoplatelets. Small. 2009;5:82-5.

[28] Kosynkin DV, Higginbotham AL, Sinitskii A, Lomeda JR, Dimiev A, Price BK, et al. Longitudinal unzipping of carbon nanotubes to form graphene nanoribbons. Nature. 2009;458:872-6.

[29] Delgado JL, Herranz MÁ, Martín N. The nano-forms of carbon. J Mater Chem. 2008;18:1417-26.

[30] Mullick Chowdhury S, Lalwani G, Zhang K, Yang JY, Neville K, Sitharaman B. Cell specific cytotoxicity and uptake of graphene nanoribbons. Biomaterials. 2013;34:283-93.

[31] Hong L, Peptan IA, Colpan A, Daw JL. Adipose tissue engineering by human adipose-derived stromal cells. Cells, Tissues, Organs. 2006;183:133-40.

[32] Majors AK, Boehm CA, Nitto H, Midura RJ, Muschler GF. Characterization of human bone marrow stromal cells with respect to osteoblastic differentiation. J Orthop Res 2005;15:546-57.

[33] Boufker HI, Lagneaux L, Najar M, Piccart M, Ghanem G, Body JJ, et al. The Src inhibitor dasatinib accelerates the differentiation of human bone marrow-derived mesenchymal stromal cells into osteoblasts. BMC cancer. 2010;10:298.

[34] Mikos AG. Effect of bone extracellular matrix synthesized in vitro on the osteoblastic differentiation of marrow stromal cells. Biomaterials. 2005;26:971-7.

[35] O'Brien J, Wilson I, Orton T, Pognan F. Investigation of the Alamar Blue (resazurin) fluorescent dye for the assessment of mammalian cell cytotoxicity. Eur J Biochem. 2003;267:5421-6.

[36] Gupta AK, Wells S. Surface-modified superparamagnetic nanoparticles for drug delivery: preparation, characterization, and cytotoxicity studies. IEEE Trans Nanobiosci. 2004;3:66-73.

[37] Mehlem A, Hagberg CE, Muhl L, Eriksson U, Falkevall A. Imaging of neutral lipids by oil red O for analyzing the metabolic status in health and disease. Nat Protoc. 2013;8:1149-54.

[38] Krause U, Seckinger A, Gregory CA. Assays of Osteogenic Differentiation by Cultured Human Mesenchymal Stem Cells. 2011. p. 215-30.

[39] Toquet J, Rohanizadeh R, Guicheux J, Couillaud S, Passuti N, Daculsi G, et al. Osteogenic potential in vitro of human bone marrow cells cultured on macroporous biphasic calcium phosphate ceramic. J Biomed Mater Res. 1999;44:98-108.

[40] Heller DA, Baik S, Eurell TE, Strano MS. Single-Walled Carbon Nanotube Spectroscopy in Live Cells: Towards Long-Term Labels and Optical Sensors. Adv Mater. 2005;17:2793-9.

[41] Strano MS, Huffman CB, Moore VC, O'Connell MJ, Haroz EH, Hubbard J, et al. Reversible, band-gap-selective protonation of single-walled carbon nanotubes in solution. J Phys Chem B. 2003;107:6979-85.

[42] Liao K-H, Lin Y-S, Macosko CW, Haynes CL. Cytotoxicity of graphene oxide and graphene in human erythrocytes and skin fibroblasts. ACS Appl Mater Interfaces. 2011;3:2607-15.

[43] Mao HY, Laurent S, Chen W, Akhavan O, Imani M, Ashkarran AA, et al. Graphene: promises, facts, opportunities, and challenges in nanomedicine. Chem Rev. 2013;113:3407-24.

[44] Dubey N, Bentini R, Islam I, Cao T, Castro Neto AH, Rosa V. Graphene: A Versatile Carbon-Based Material for Bone Tissue Engineering. Stem cells international. 2015;2015:804213.

[45] Zigdon-Giladi H, Rudich U, Geller GM, Evron A. Recent advances in bone regeneration using adult stem cells. World journal of stem cells. 2015;7:630.

[46] Strauer BE, Kornowski R. Stem cell therapy in perspective. Circulation. 2003;107:929-34.

[47] Dresselhaus MS, Dresselhaus G, Saito R, Jorio A. Raman spectroscopy of carbon nanotubes. Phys Rep. 2005;409:47-99.

[48] Salzmann CG, Llewellyn SA, Tobias G, Ward MA, Huh Y, Green ML. The Role of Carboxylated Carbonaceous Fragments in the Functionalization and Spectroscopy of a Single-Walled Carbon-Nanotube Material. Adv Mater. 2007;19:883-7.

[49] Kosynkin DV, Higginbotham AL, Sinitskii A, Lomeda JR, Dimiev A, Price BK, et al. Longitudinal unzipping of carbon nanotubes to form graphene nanoribbons. Nature. 2009;458:872-6.

[50] Lalwani G, Kwaczala AT, Kanakia S, Patel SC, Judex S, Sitharaman B. Fabrication and Characterization of Three-Dimensional Macroscopic All-Carbon Scaffolds. Carbon. 2013;53:90-100.

[51] Pittenger MF, Mackay AM, Beck SC, Jaiswal RK, Douglas R, Mosca JD, et al. Multilineage potential of adult human mesenchymal stem cells. science. 1999;284:143-7.

[52] Jaiswal RK, Jaiswal N, Bruder SP, Mbalaviele G, Marshak DR, Pittenger MF. Adult human mesenchymal stem cell differentiation to the osteogenic or adipogenic lineage is regulated by mitogen-activated protein kinase. Journal of Biological Chemistry. 2000;275:9645-52.

[53] Raffa V, Ciofani G, Vittorio O, Riggio C, Cuschieri A. Physicochemical properties affecting cellular uptake of carbon nanotubes. Nanomedicine. 2010;5:89-97.

[54] Rejman J, Oberle V, Zuhorn IS, Hoekstra D. Size-dependent internalization of particles via the pathways of clathrin- and caveolae-mediated endocytosis. Biochem J. 2004;377:159-69.

[55] Chang Y, Yang S-T, Liu J-H, Dong E, Wang Y, Cao A, et al. In vitro toxicity evaluation of graphene oxide on A549 cells. Toxicology letters. 2011;200:201-10.

[56] Shvedova AA, Pietroiusti A, Fadeel B, Kagan VE. Mechanisms of carbon nanotube-induced toxicity: Focus on oxidative stress. Toxicology and Applied Pharmacology. 2012;261:121-33.

[57] Liu S, Wei L, Hao L, Fang N, Chang MW, Xu R, et al. Sharper and faster "nano darts" kill more bacteria: a study of antibacterial activity of individually dispersed pristine single-walled carbon nanotube. ACS nano. 2009;3:3891-902.

[58] Arvizo RR, Miranda OR, Thompson MA, Pabelick CM, Bhattacharya R, Robertson JD, et al. Effect of nanoparticle surface charge at the plasma membrane and beyond. Nano Lett. 2010;10:2543-8.

[59] Dubey N, Bentini R, Islam I, Cao T, Neto AHC, Rosa V. Graphene: A Versatile Carbon-Based Material for Bone Tissue Engineering. Stem cells international. 2015;2015.

[60] Akhavan O, Ghaderi E, Shahsavar M. Graphene nanogrids for selective and fast osteogenic differentiation of human mesenchymal stem cells. Carbon. 2013;59:200-11.

[61] Kalbacova M, Broz A, Kong J, Kalbac M. Graphene substrates promote adherence of human osteoblasts and mesenchymal stromal cells. Carbon. 2010;48:4323-9.

Figures

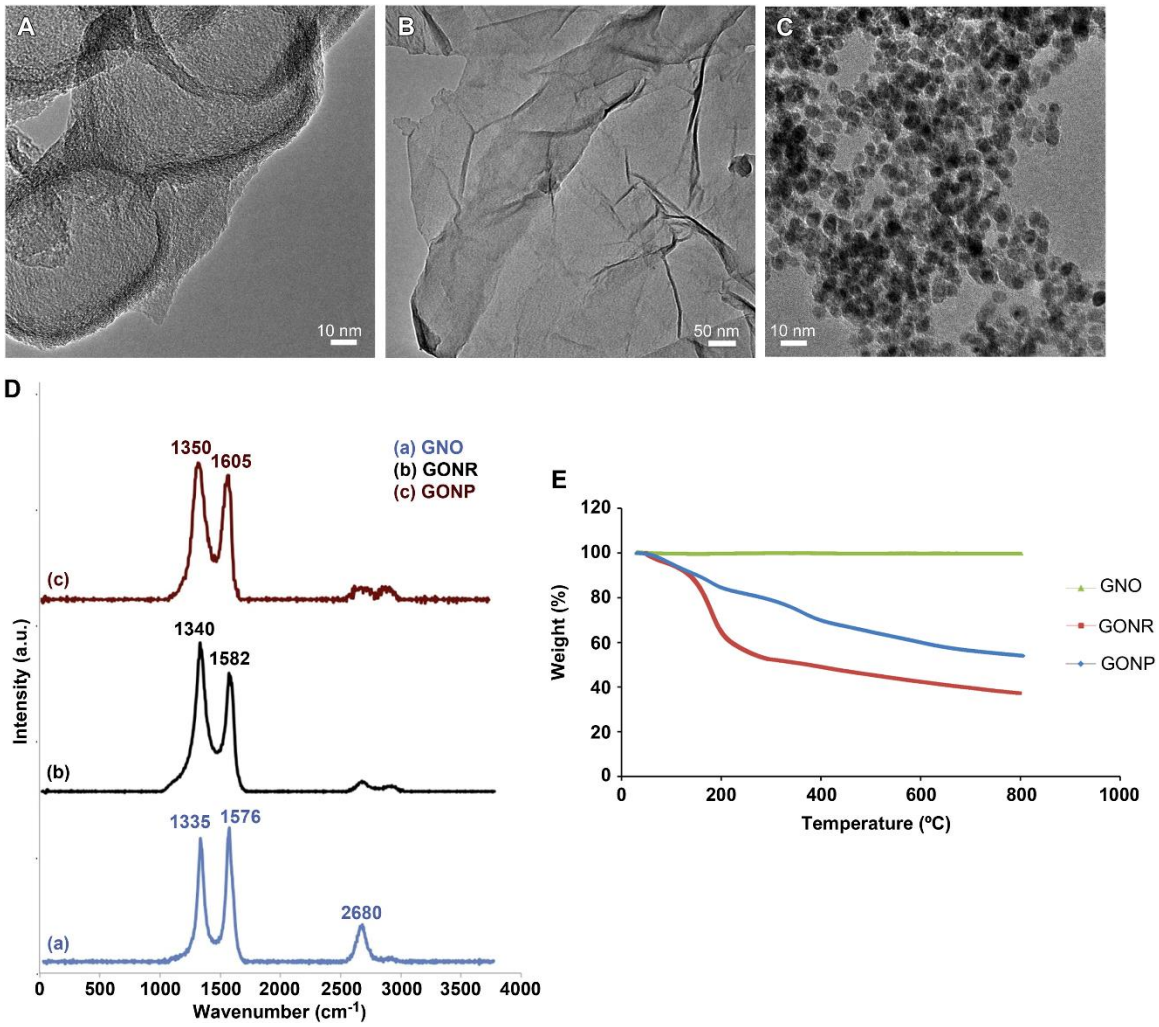

Figure 1: Representative HRTEM images of GNOs (A), GONRs (B), and GONPs (C). Scale bars: (A) 10 nm, (B) 50 nm, and (C) 10 nm. (D) Representative Raman spectra of GNOs (a), GONRs (b), and GONPs (c). (E) TGA profiles of GNOs, GONRs, and GONPs.

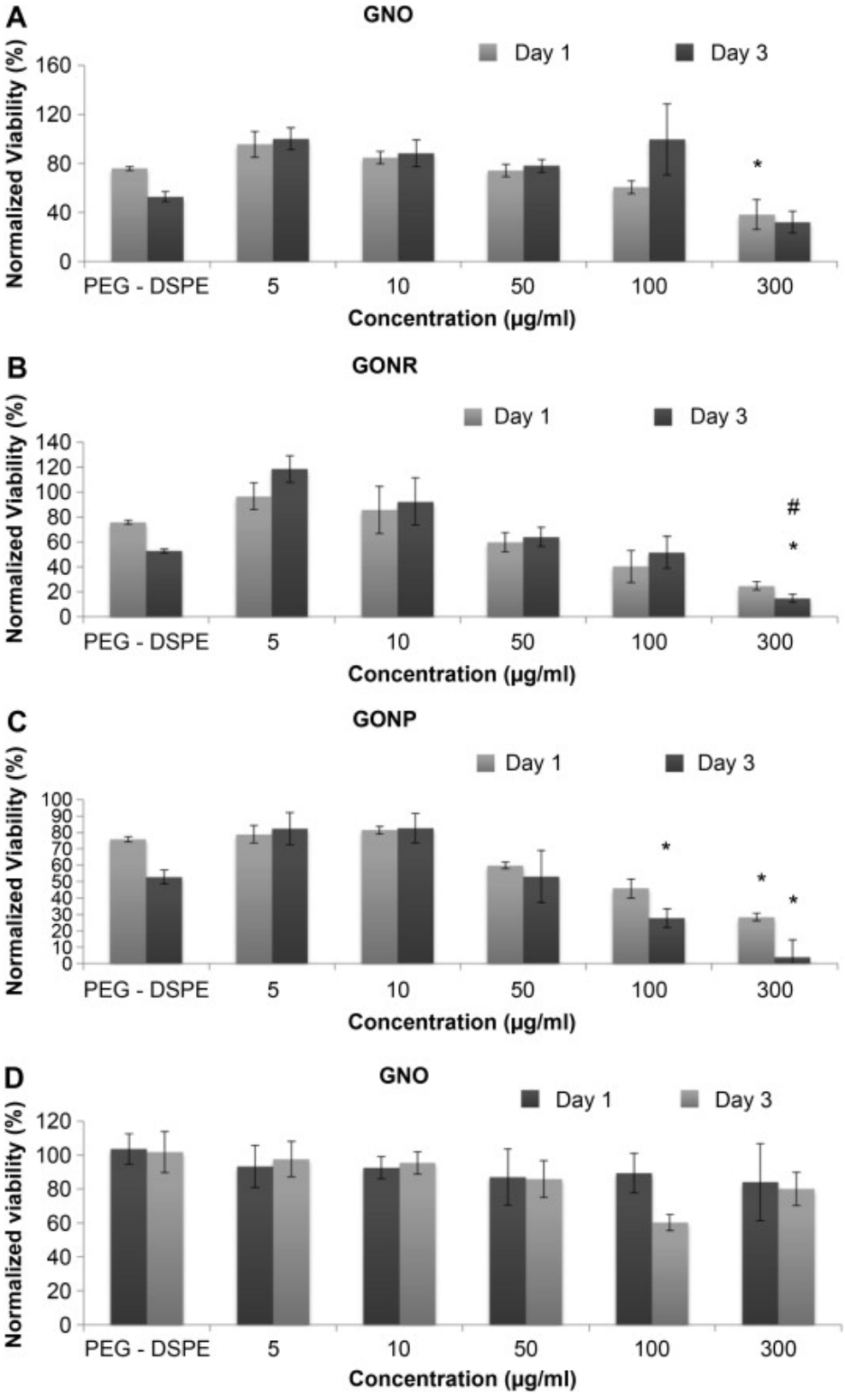
A
GNO
Day 1
Day 3
Normalized Viability (%)
160
120
80
40
0
*
PEG - DSPE
5
10
50
100
300
Concentration (µg/ml)
B
GONR
Day 1
Day 3
Normalized Viability (%)
140
120
100
80
60
40
20
0
#
*
PEG - DSPE
5
10
50
100
300
Concentration (µg/ml)
C
GONP
Day 1
Day 3
Normalized Viability (%)
100
90
80
70
60
50
40
30
20
10
0
*
*
*
PEG - DSPE
5
10
50
100
300
Concentration (µg/ml)
D
GNO
Day 1
Day 3
Normalized viability (%)
120
100
80
60
40
20
0
PEG - DSPE
5
10
50
100
300
Concentration (µg/ml)

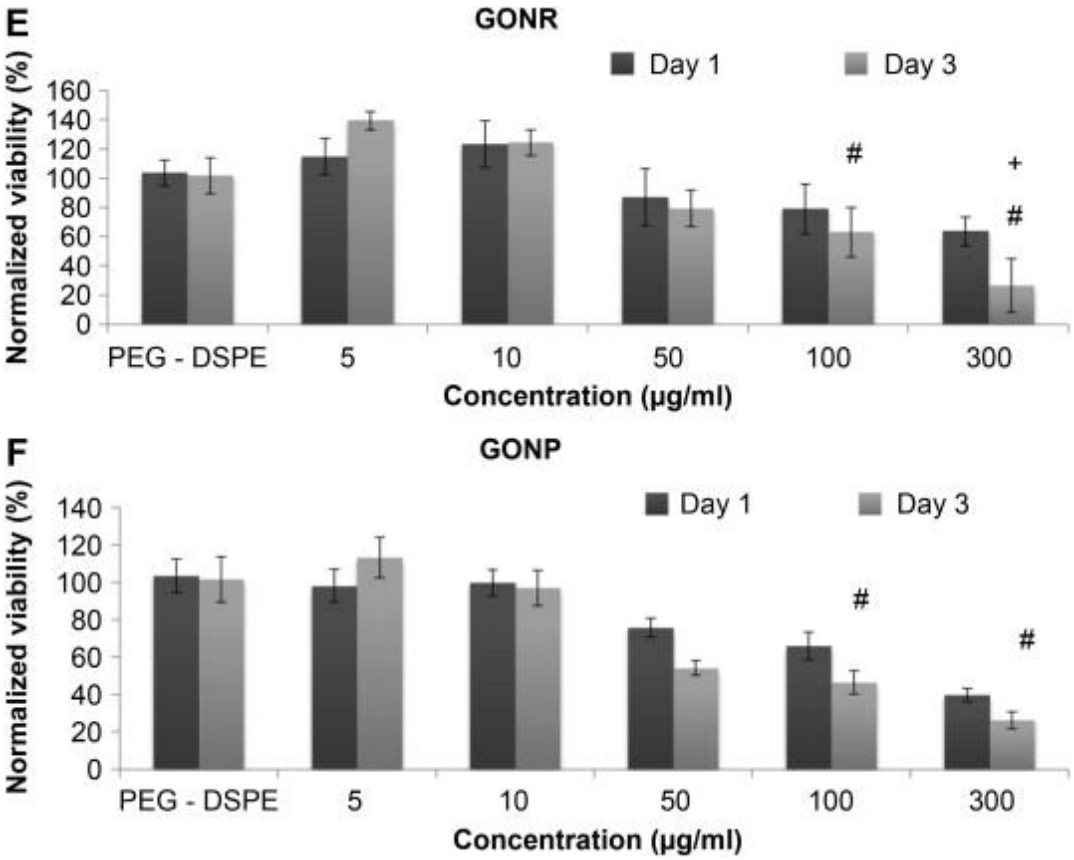

Figure 2: AlamarBlue assay results at one and three days after treatment with GNOs (A), GONRs (B), and GONPs (C) for adMSCs; after treatment with GNOs (D), GONRs (E), and GONPs (F) for bmMSCs. For each nanoparticle, cells were treated with PEG-DSPE, 5 µg/ml, 10 µg/ml, 50 µg/ml, 100 µg/ml, and 300 µg/ml concentrations. Data are presented as mean +/- standard deviation of percentage viability compared to untreated cells (n=4). Statistical significance ($p<0.05$) with respect to untreated groups, 5 µg/ml groups, and 10 µg/ml groups is denoted by (*), (#), and (+) respectively.

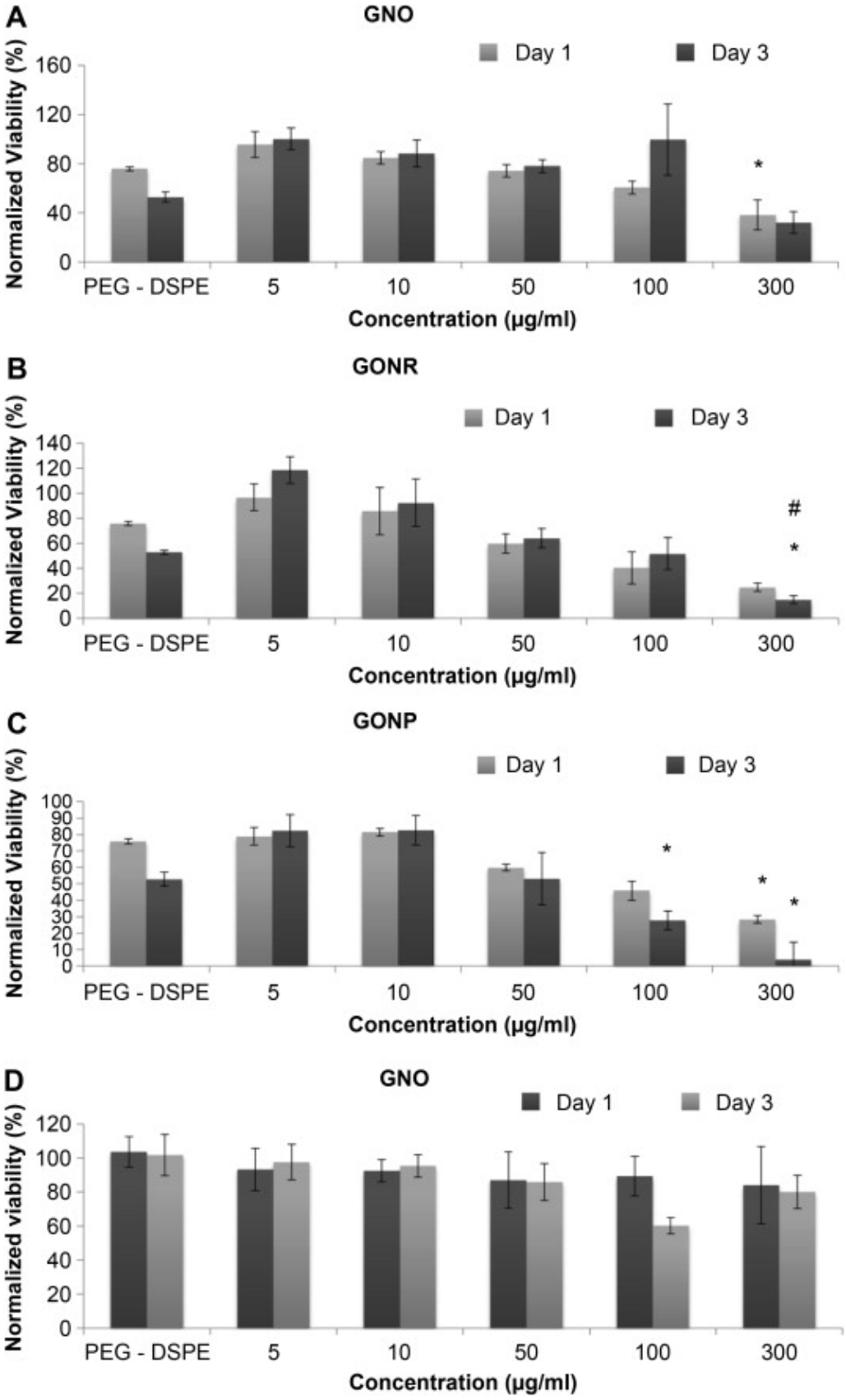
A
GNO
Day 1
Day 3
Normalized Viability (%)
160
120
80
40
0
*
PEG - DSPE
5
10
50
100
300
Concentration (µg/ml)
B
GONR
Day 1
Day 3
Normalized Viability (%)
140
120
100
80
60
40
20
0
#
*
PEG - DSPE
5
10
50
100
300
Concentration (µg/ml)
C
GONP
Day 1
Day 3
Normalized Viability (%)
100
90
80
70
60
50
40
30
20
10
0
*
*
*
PEG - DSPE
5
10
50
100
300
Concentration (µg/ml)
D
GNO
Day 1
Day 3
Normalized viability (%)
120
100
80
60
40
20
0
PEG - DSPE
5
10
50
100
300
Concentration (µg/ml)

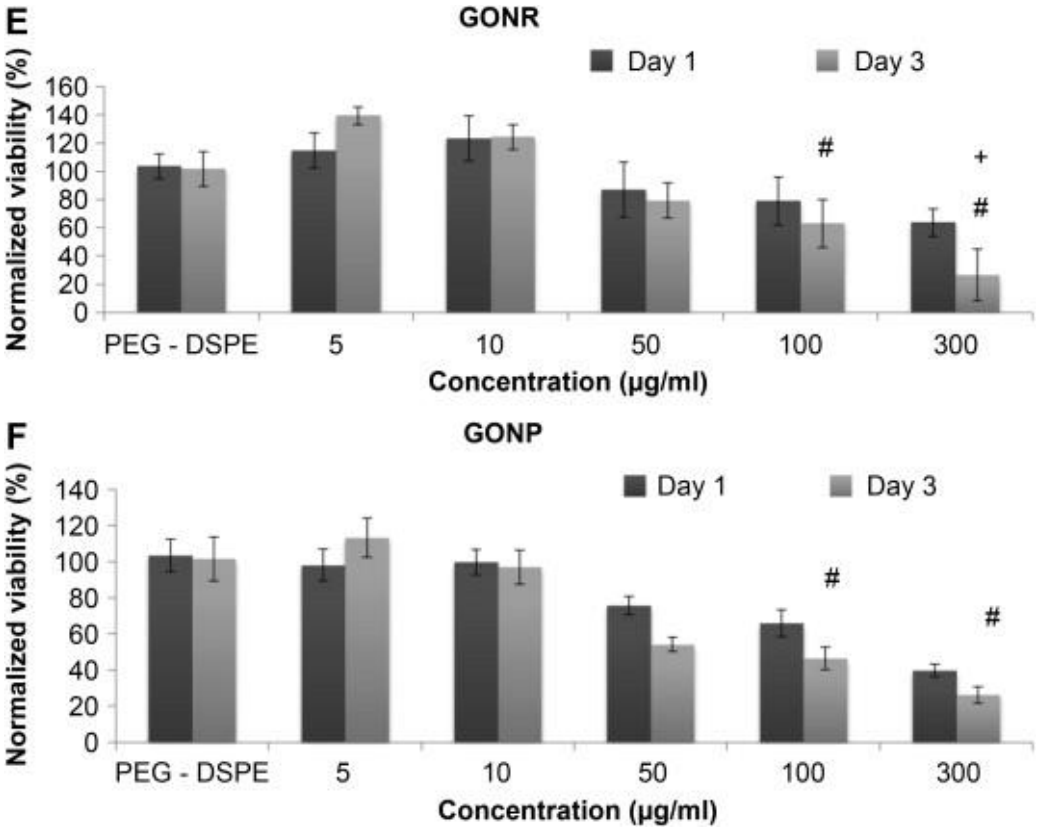

Figure 3: Calcein AM assay results at one and three days after treatment with GNOs (A), GONRs (B), and GONPs (C) for adMSCs; after treatment with GNOs (D), GONRs (E), and GONPs (F) for bmMSCs. For each nanoparticle, cells were treated with PEG-DSPE, at 5 µg/ml, 10 µg/ml, 50 µg/ml, 100 µg/ml, and 300 µg/ml concentrations. Data are presented as mean +/- standard deviation of percentage viability compared to untreated cells (n=4). Statistical significance ($p<0.05$) with respect to untreated groups, 5 µg/ml groups, and 10 µg/ml groups is denoted by (*), (#), and (+) respectively.

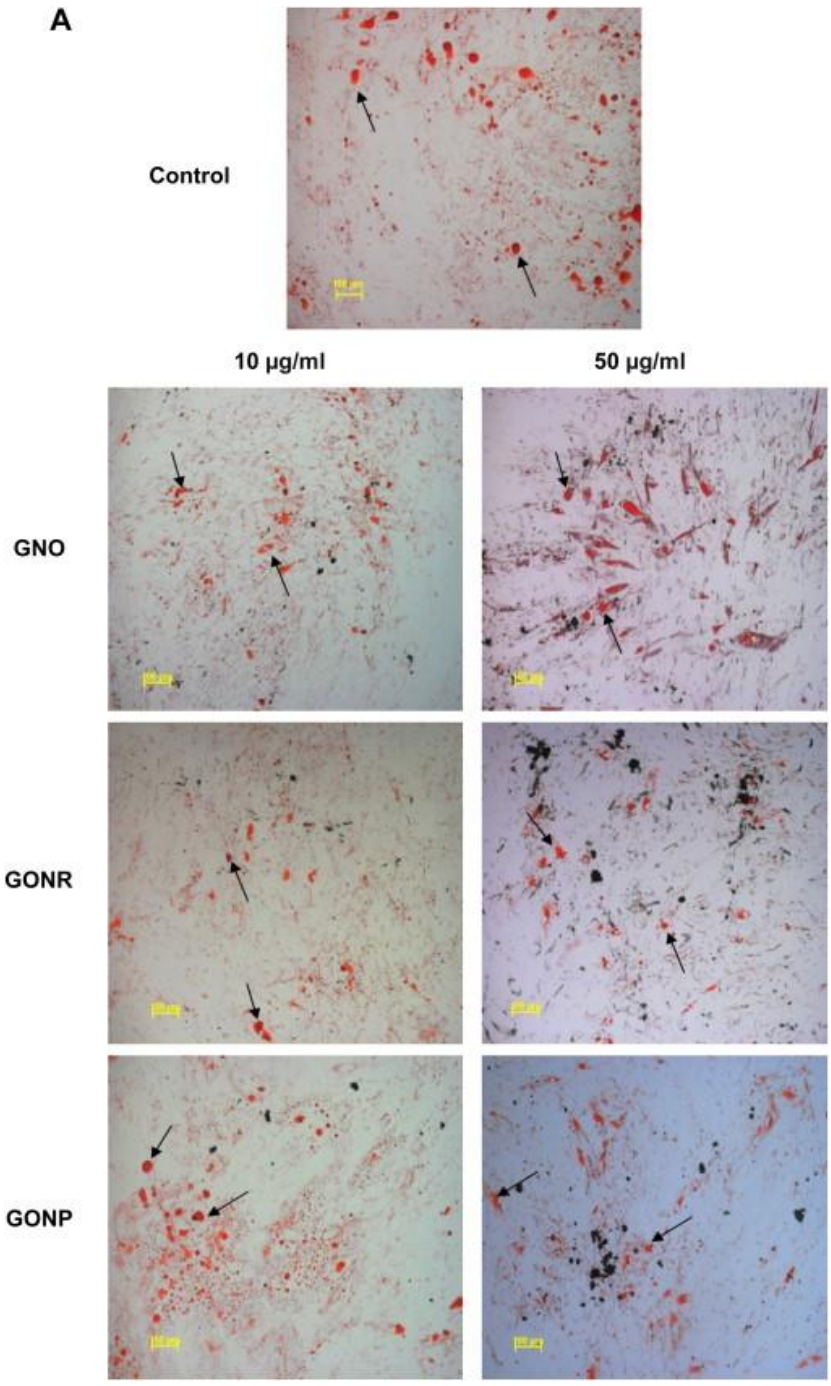
A
Control
10 µg/ml
50 µg/ml
GNO
GONR
GONP

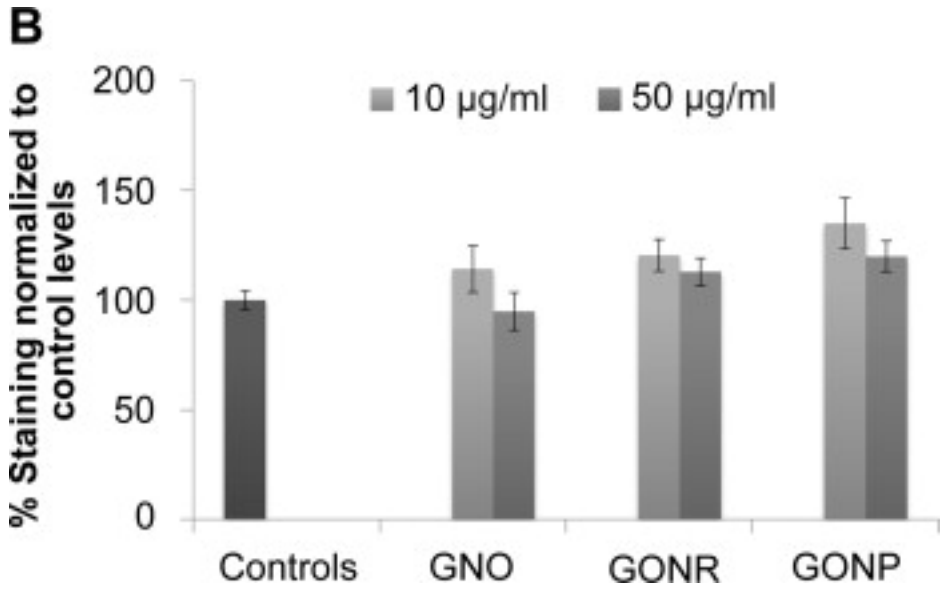

Figure 4. Adipogenesis results. (A) Histological specimens of adMSCs incubated with GNOs, GONRs, and GONPs for 24 hours, followed by incubation with adipogenic differentiation media for 21 days, stained by Oil Red O. (B) Elution of Oil Red O stain. Data are normalized to control values and presented as mean +/- standard deviation (n=3). Statistical significance (p<0.05) compared to the control was determined by the Kruskal-Wallis test with Dunn's post hoc (*).

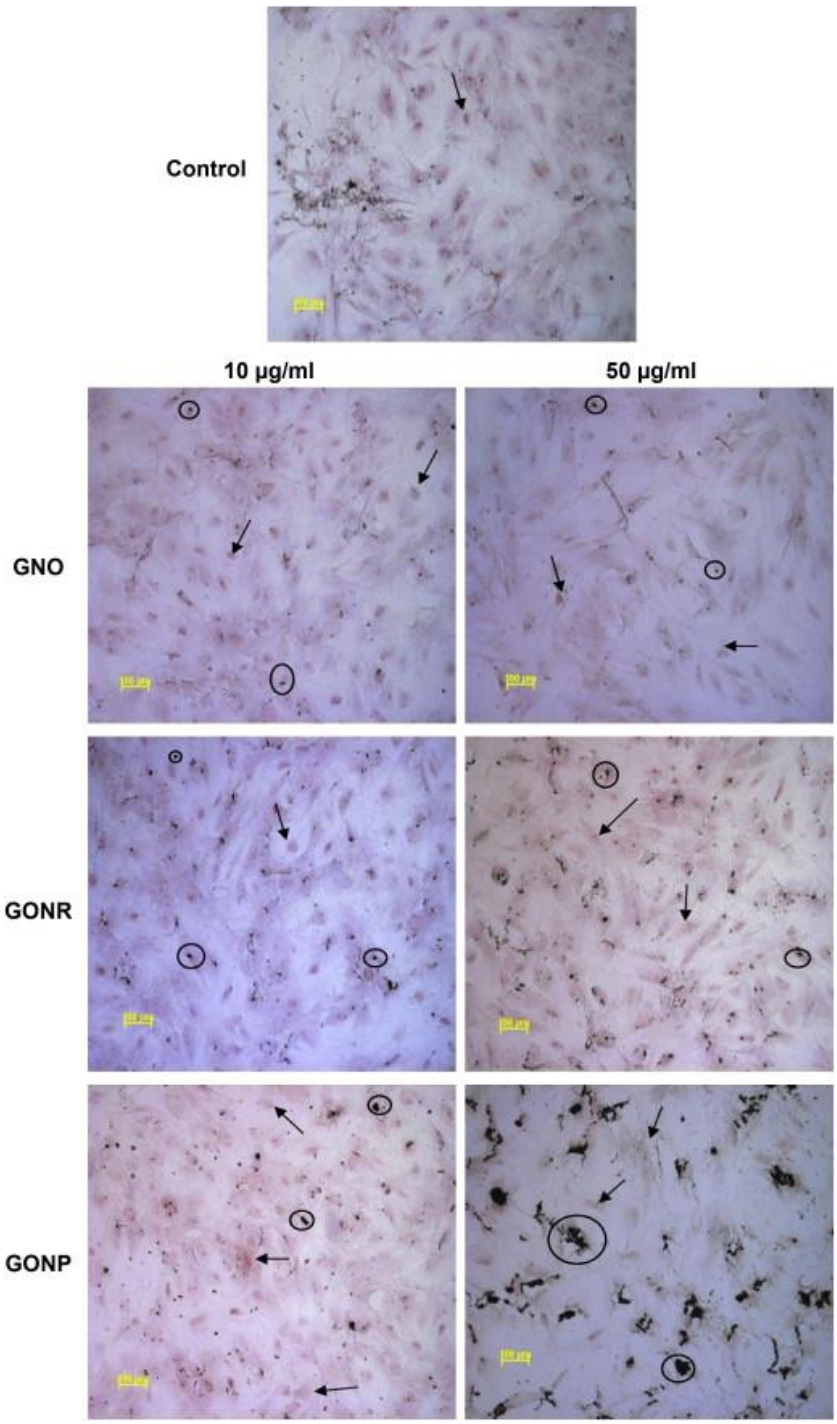

Figure 5. Osteogenesis results. adMSCs after treatment for 24 hours with either 10 or 50 µg/ml of GNOs, GONRs, or GONPs respectively, followed by 14 days of incubation with osteogenic differentiation media stained with Alizarin Red S.

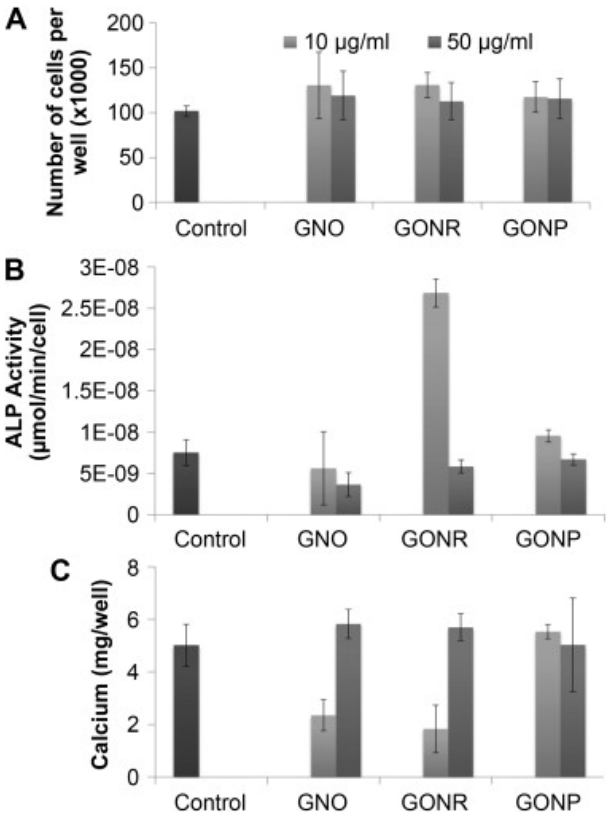

Figure 6. Osteogenesis results. (A) Cellularity for adMSCs after treatment for 24 hours with either 10 or 50 µg/ml of GNOs, GONRs, or GONPs, followed by 14 days of incubation with osteogenic differentiation media. (B) ALP activity in adMSCs after treatment for 24 hours with either 10 or 50 µg/ml of GNOs, GONRs, or GONPs, followed by 14 days of incubation with osteogenic differentiation media. (C) Calcium content after treatment for 24 hours with either 10 or 50 µg/ml of GNOs, GONRs, or GONPs, followed by 14 days of incubation with osteogenic differentiation media. Data are presented as mean +/- standard deviation of mg of calcium per well (n=3). Statistical significance (p<0.05) compared to the control was determined by the Kruskal-Wallis test with Dunn's post hoc (*).

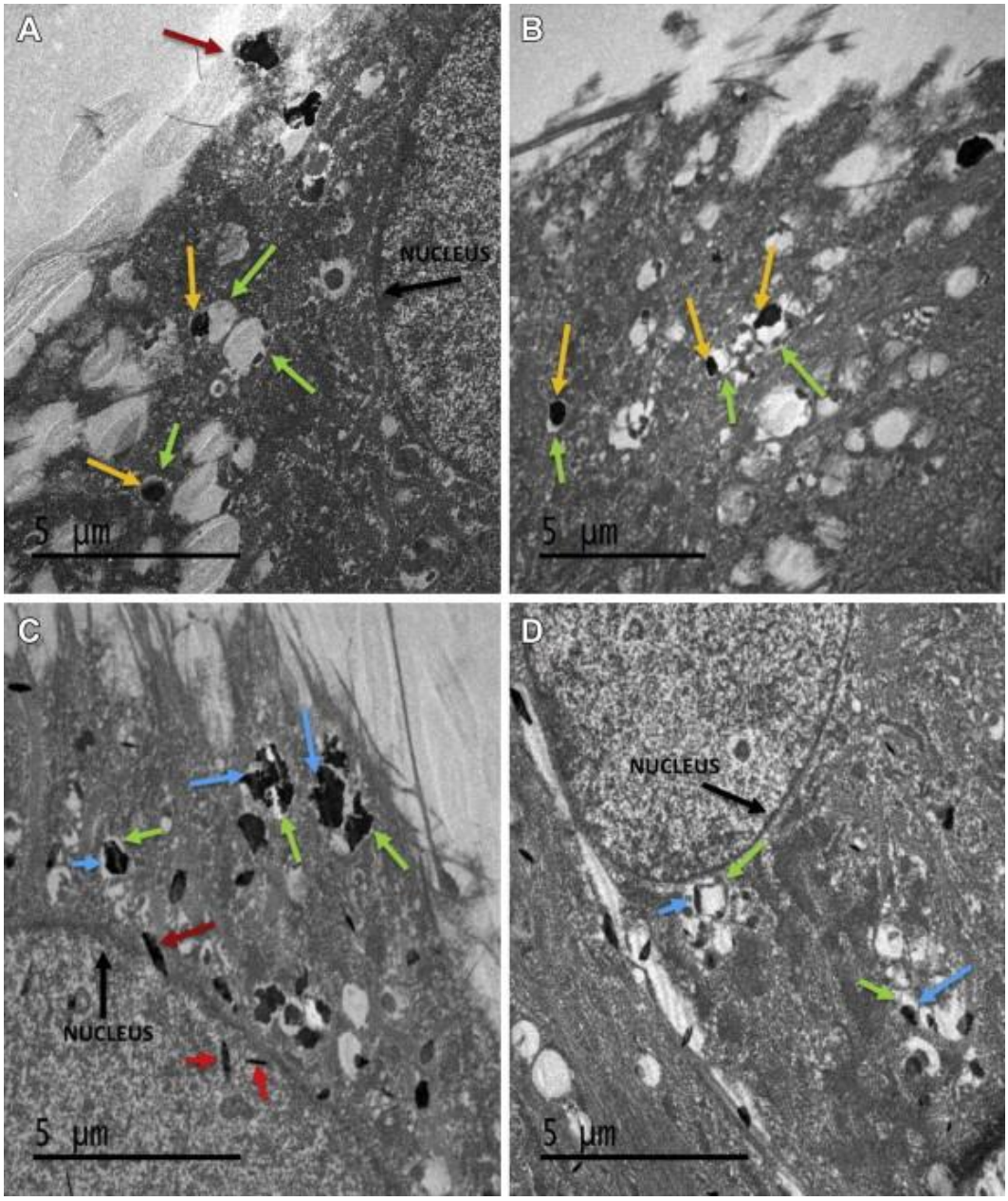

Figure 7. Representative TEM images of adMSCs treated with GNOs (A & B) and GONPs (C & D). GNOs aggregates (yellow arrow) are seen in vacuoles (green arrows) in the cytoplasm of the cell. GNOs are not seen inside the nucleus (black arrow). GONPs particles (blue arrows) are seen in the cytoplasm enclosed in vacuoles. They can also been seen inside the nucleus (red arrows).

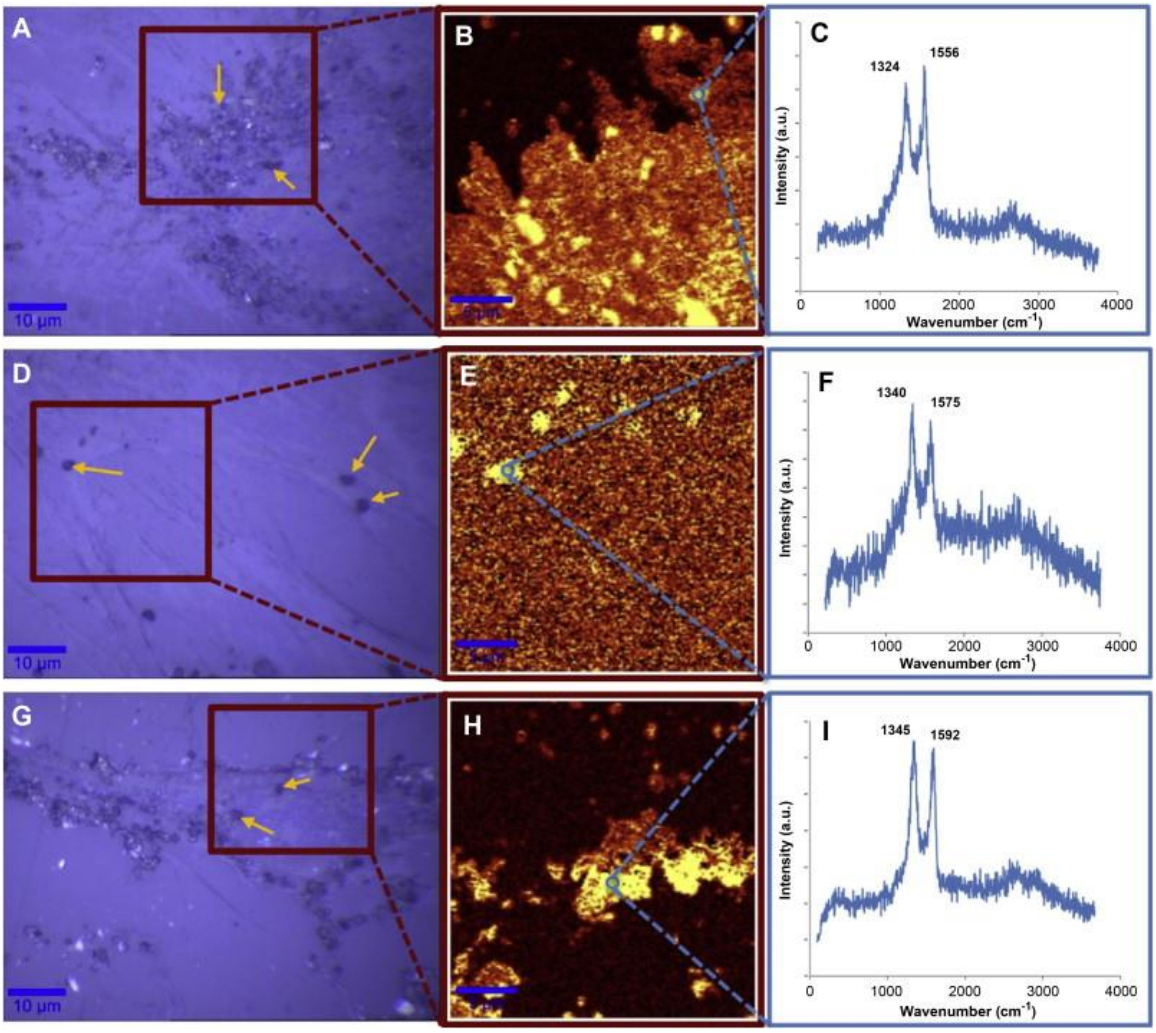

Figure 8. A, D and G show representative brightfield images of adMSCs treated with GNOs, GONRs, and GONPs, respectively. B, E, H show the confocal Raman map of selected regions in A, D, and G. Parts C, F and I show characteristic D- and G-band spectra of GNOs, GONRs, and GONPs employed to obtain confocal Raman maps of these nanoparticles.

Tables

Table 1: Physicochemical characterization of GNOs, GONRs and GONPs by TEM, Raman spectroscopy, TGA and DLS.

Nanoparticle	Dimensions (nm)	Raman peaks	I_D/i_G	Zeta potential (mV)	Hydrodynamic diameter (nm)
GNO	(d) 50–300	1335 cm^{-1}(D), 1576 cm^{-1}(G), 2680 cm^{-1}(G′)	0.92	−32.3 ± 1.35	460.76 ± 53.58
GONR	(w) × (l) 60–90 × 500–1500	1340 cm^{-1}(D), 1580 cm^{-1}(G)	1.28	−26.30 ± 0.75	457.5 ± 35.70
GONP	(d) 20–40	1351 cm^{-1}(D), 1604 cm^{-1}(G)	1.09	−12.47 ± 0.12	296.4 ± 20.32

Table 2: Percentage decrease in viability assessed by Alamar Blue assay of adMSCs and bmMSCs treated with GNOs, GONRs and GONPs at concentration of 300 µg/ml at day 1 and 3 compared to control.

	adMSC		bmMSC	
	Day 1	Day 3	Day 1	Day 3
GNOs	86%	69%	50%	39%
GONRs	93%	79%	67%	72%
GONPs	100%	98%	62%	93%

Table 3: Percentage decrease in viability assessed by Calcein AM assay of adMSCs and bmMSCs treated with GNOs, GONRs and GONPs at concentration of 300 µg/ml at day 1 and 3 compared to control.

	adMSC		bmMSC	
	Day 1	Day 3	Day 1	Day 3
GNOs	98%	38%	19%	21%
GONRs	94%	91%	39%	74%
GONPs	65%	80%	62%	74%

Table 4: CD50 values of adMSCs and bmMSCs treated with GNOs, GONRs and GONPs evaluated by Alamar Blue and CalceinAM assays.

	CD50 (μg/ml)			
	adMSC		bmMSC	
	Alamar Blue	Calcein AM	Alamar Blue	Calcein AM
GNOs	244	164	615	128
GONRs	142	137	200	123
GONPs	79	125	167	198

Chapter 3: Investigate PA imaging of tissue engineering scaffolds

Portions of this chapter have been reproduced from:

Yahfi Talukdar, Pramod Avti, John Sun, Balaji Sitharaman. “Multimodal ultrasound-photoacoustic imaging of tissue engineering scaffolds and blood oxygen saturation in and around the scaffolds”. *Tissue Engineering Part C: Methods*. 2014;20(5):440-9.

*The authors listed in the above manuscript have contributions towards data reported in this chapter

Abstract

Preclinical, noninvasive imaging of tissue engineering polymeric scaffold's structure and/or the physiological processes such as blood oxygenation remains a challenge. *In vitro* or *ex vivo*, the widely used scaffold characterization modalities such as porosimetry, electron or optical microscopy, and X-ray micro-computed tomography has limitations or disadvantages - some are invasive or destructive, others have limited tissue penetration (few hundred micrometers) and/ or show poor contrast under physiological conditions. Post-mortem histological analysis, the most robust technique for the evaluation of neo-vascularization is obviously not appropriate for acquiring physiological or longitudinal data. Herein, we have explored the potential of ultrasound (US)-coregistered photoacoustic (PA) imaging as a non-invasive multimodal imaging modality to overcome some of the above challenges and/ or provide complementary information. US-PA imaging was employed to characterize poly(lactic-co-glycolic acid) (PLGA) polymer scaffolds or single-walled carbon nanotube (SWCNT)-incorporated PLGA (SWCNT-PLGA) polymer scaffolds as well as blood oxygen saturation within and around the scaffolds. *Ex vivo*, PLGA and SWCNT-PLGA scaffolds were placed at 0.5 mm, 2 mm and 6 mm depths in chicken breast tissues. PLGA scaffolds could be localized with US imaging, but generate no PA signal (excitation wavelengths 680 nm and 780 nm). SWCNT-PLGA scaffolds generated strong PA signals at both wavelengths due to the presence of the SWCNTs and could be localized with both US and PA imaging depths between 0.5-6 mm (lateral resolution = 90 µm, axial resolution = 40 µm). *In vivo*, PLGA, and SWCNT-PLGA scaffolds were implanted in subcutaneous pockets at 2 mm depth in rats, and imaged at 7 and 14 days post-surgery. The anatomical position of both the scaffolds could be determined from the US images. Only SWCNT-PLGA scaffolds could be easily detected in the US-PA images. SWCNT-PLGA scaffolds had significant four times higher PA signal intensity compared to surrounding tissue and PLGA scaffolds. *In vivo* blood oxygen saturation maps around and within the PLGA scaffolds could be obtained by PA imaging. There

was no significant difference in oxygen saturation for the PLGA scaffolds at the two-time points. The blood oxygen saturation maps complemented the histological analysis of neo-vascularization of the PLGA scaffolds.

Introduction

A variety of synthetic biodegradable polymer-based scaffolds have thus far been developed for tissue engineering applications.[1-7] Poly-lactic-co-glycolic (PLGA), a FDA-approved polymer, is widely used to fabricate scaffolds because of its mechanical properties, biocompatibility and biodegradability. [2, 3, 8, 9] Recently, nanoparticle-incorporated PLGA nanocomposites have also been developed.[1, 10] The nanoparticles, apart from enhancing the mechanical properties of PLGA, have shown to affect the differentiation of progenitor cells.[11]

In vivo non-invasive imaging of polymeric scaffolds remains a challenge. Even though, *ex vivo*, many characterization techniques such as mercury porosimetry, scanning electron microscopy (SEM), laser scanning optical microscopy techniques (e.g. confocal and two-photon microscopy), and X-ray micro-computed tomography (μCT) are available to assess polymeric scaffold properties such as structure, porosity and pore size; *in vivo*, these techniques have significant limitations.[12] The contrast of wet polymeric scaffolds such as PLGA immersed in blood or biological media using μCT is poor, while mercury porosimetry and SEM require sample preparation that is only possible *ex vivo*. Thus, for *in vivo* studies, invasive post mortem histology is considered as the gold standard to investigate the changes in the scaffold properties, degradation as well as tissue regeneration and vascularization within the scaffolds.[4] Especially, for longitudinal studies, large number of animals implanted with scaffolds are sacrificed at various time points, the scaffold along with the surrounding tissue explanted, and micrometer thick sections are prepared for histological analysis. This procedure could cause scaffolds debris, small proteins, nucleic acids, extracellular complex carbohydrates and other soluble metabolites to be washed away,[13-15] and thus, affects and limits the analysis of the scaffold's physicochemical properties and deposited extracellular matrix. Additionally, porous scaffolds with lower mechanical properties compared to the tissue could crumble, fall out of the surrounding tissue or get displaced during the histological specimen preparation making it

challenging to characterize its structural properties and/or investigate tissue regeneration within these scaffolds. Furthermore, although blood vessel cross-sections can be located in histological sections, the process of vasculogenesis[16] cannot be characterized by histological analysis alone, and complementary physiological information such as blood oxygen saturation cannot be monitored. Monitoring oxygen saturation or oxygenation of tissue engineering scaffold is very important during the process of tissue regeneration. Scaffolds with low oxygen penetration fail to support live cells and prevent tissue regeneration. It is important for aerobic metabolism, cell proliferation and even differentiation of mesenchymal stem cells (MSC). Upon implantation of the scaffolds *in vivo*, it takes about 8-12 days before neovascularization occurs.[17] During this period the cells in the scaffolds rely solely on blood perfusion for oxygen and nutrition. Oxygen saturation of tissue engineering scaffold decreases exponentially with depth.[18] As the interstitial fluid enters the scaffold, the cells on outer layers of the scaffold use up the oxygen leaving hypoxic regions at the center of the scaffold. In these regions, MSCs fail to proliferate and differentiate into osteoblasts, delaying the process of tissue regeneration.[19-21]

To this end various superficial and whole-body small animal imaging modalities have recently been explored for imaging tissue engineering scaffolds.*[22-28]*Each modality has its advantages and limitations. Superficial optical imaging techniques, with excellent sub- μm resolutions, such as bioluminescence, fluorescence, optical coherence tomography (OCT) and two-photon imaging have various limitations such as low tissue penetration (tens to hundreds of micrometers), optical scattering and attenuation, or interferences due to background tissue auto-fluorescence. Additionally, techniques such as bioluminescence imaging require genetically modified small animal model, and fluorescence or two-photon microscopy require the use of fluorophores that may photobleach or interfere with normal physiological processes.[25] Deep tissue imaging modalities, such as X-ray computed tomography (CT), magnetic resonance imaging (MRI), or positron emission tomography (PET) allow whole body imaging. However, μCT of tissue

engineering scaffolds, show poor contrast when perfused with body fluids.[12] Additionally, imaging blood vessels is possible only after injection of contrast agents into the blood vessels post mortem, and thus, not appropriate to obtain longitudinal or real-time information on the process of neo-vascularization[27]. Unlike CT that uses harmful x-ray radiation; MRI is considerably safer. [26, 29-34] However, the contrast of tissue engineering scaffolds monitored using MRI is poor until water can penetrate and perfuse the scaffold. [33-35] This method also requires the use of contrast agents with high relaxivity values. In addition to contrast agents, the strong magnetic fields required for MRI might not be suitable for studying metallic (e.g. titanium) scaffolds. PET has also been proposed for imaging vasculature and although it can effectively target highly vascular tumors[34, 35] with a resolution of 1-2 mm, it is incapable of imaging neo-vasculature or micron-sized blood capillaries in tissue engineering scaffolds.

Recently, photoacoustic microscopy (PAM) imaging has shown promise to non-invasively characterize the porosity and pore size of tissue engineering scaffolds in vitro, and neovascularization within scaffolds *in vivo*.[12, 36] Additionally, the same technique could also be used for histological and histomorphometric analysis of scaffolds.[12] Differential absorption by exogenous (e.g. single-walled carbon nanotubes (SWCNTs)) or endogenous (e.g. hemoglobin) materials, at a specific optical wavelength, is responsible for the contrast generated in PA imaging systems.[12, 28, 36-38] Most biological molecules do not absorb at near infrared (NIR) wavelengths, and therefore do not generate robust PA signals. Oxyhemoglobin and hemoglobin are two of the relatively few endogenous molecules that absorb in this region, and due to their differential absorption spectra, allow mapping of *in vivo* oxygen saturation by PAM.[36] SWCNTs absorb strongly at the near infrared region and generate PA signal stronger than endogenous absorbers such a hemoglobin and melanin.[38, 39]

Pure PA imaging does not typically provide the appropriate contextual anatomic information for useful localization of the photoacoustic imaging signals within the animal.[40] Although white

light overlay methods are beneficial, due to difficulty in animal repositioning, repeated imaging of the same animal in different imaging sessions often results in misinterpretation of the signal localization.[41] The white-light reference image typically used in a pure PA imaging system may be suitable for localization of large objects such as tumor masses, but lacks the anatomical context required for repeatedly localizing smaller signals of interest and/or mapping the molecular signals to bones or other anatomical structures within the animal. Ultrasound (US)-based co-registration of the PA signal has been reported to allow suitable contextual anatomical information of generated PA signals.[42] Using US-PA multi modal imaging both anatomical and physiological data can be obtained. US-PA has thus far been investigated for various preclinical applications such as intravascular imaging of atherosclerotic plaques, tumor detection and staging, *in vivo* stem cell tracking. [43-47] To the best of our knowledge, till date, the potential benefits of US-PA in the field of tissue engineering have not been explored. Therefore, in this study, we investigate the suitability of multimodal US-PA system to image tissue-engineering scaffolds and monitor oxygen saturation *in vivo* in a rat model.

Materials and Methods

2. 1 SWCNT synthesis

SWCNTs were synthesized as described previously.[12] Diblock copolymer templating method was used to coat Fe on Si wafers and placed in a 3-inch-diameter quartz reaction chamber (Easy Tube 2000; First Nano, Central Islip, NY). The chamber was then filled with H_2 for 2 minutes followed by CH_4 as carbon feedstock for 20 minutes. The furnace was then switched off and cooled to room temperature.

2. 2 Scaffold preparation

Porous polylactic-co-glycolic-acid (PLGA) scaffolds were prepared as previously described.[12, 48] PLGA scaffolds with single walled carbon nanotubes (SWCNT-PLGA) were made by uniformly distributing the nanotubes in PLGA (Polysciences Inc. Warrington, PA) dissolved in chloroform at 0.5 wt% concentration. Particulate leaching technique was used to make porous polymer composites using NaCl as a porogen (100-500 μm). The amount of NaCl required to achieve 90% porosity was calculated using the equation:

$$Porosity = \frac{V_{NaCl}}{V_{PLGA} + V_{SWCNT} + V_{NaCl}} \times 100\%$$

Where V_{PLGA}, V_{SWCNT} and V_{NaCl} are the volumes of PLGA, SWNT, and NaCl, respectively. The mixture of PLGA or SWCNT-PLGA with NaCl was poured into cylindrical Teflon™ molds of 4 mm diameter and 1.5 mm in height. Uniform distribution of SWCNT was obtained by stirring the mixture vigorously and vortexing before pouring it into the molds. After complete removal of chloroform, the scaffolds were removed from the molds and immersed in deionized water to

leach NaCl. The vials containing scaffolds were placed on a shaker table (80 rpm) and the water was changed every 6 hours. After 48 hours the scaffolds were removed from water, blotted dry, and air-dried at room temperature for 24 hours.

2. 3 Atomic force microscopy

The structure and dimensions of SWCNTs prepared by the method described above were determined with atomic force microscopy (AFM) as described previously.[49] In short, SWCNTs in 1:1 ethanol:water solution were dispersed by probe sonication (Cole-Parmer Ultrasonicator LPX 750) for 1 minute using a 1 second "on" and 2 second "off" cycle. To prepare samples for AFM, we spin coated 50 µl of dispersed SWCNT solution onto silicon wafers (Ted Pella, USA) at 300 rpm for 5 minutes. We used NanoSurf EasyScan 2 Flex AFM (NanoScience Instruments Inc. Phoenix) in tapping mode with a V-shaped cantilever (APP Nano ACL -10, frequency f_c = 145-230 kHz, L = 225 µm, W = 40 µm, tip radius < 10 nm, spring constant k = 20-95 N/m) for the images.

2. 4 Scanning Electron Microscopy

Scanning electron microscopy (SEM; Schottky Field Emission Scanning Electron Microscope, LEO Gemini 1550) was used to examine the structure of SWCNT-PLGA nanocomposites. The porous scaffolds were sliced, mounted on metal studs and sputter coated with gold before imaging at an acceleration voltage of 20 KV with Everhart-Thornley secondary electron detector.

2. 5 Microcomputed Tomography

Microcomputed tomography (microCT; Scanco Medical AG) was used to characterize the porosity and pore size of the scaffolds. Imaging was done with resolution of 12 µm with 55 KV energy and intensity of 145 µA. Software provided by Scanco Medical AG was used for image reconstruction and analysis. A threshold of 41 was used to represent gray scale tomograms of the

scaffold. The pore sizes were determined from 3D rendered images of the scaffold. For calculating the porosity, total volume (TV), scaffold volume (SV) and volume fraction (SV/TV) was determined. Three separate regions per scaffold was analyzed and the average was used to determine the porosity of the scaffolds using the following equation[50]:

$$Porosity = \left(1 - \frac{SV}{TV}\right) \times 100\%$$

2. 6 Animals and subcutaneous scaffold implants

Animal experiments were performed in compliance with the Institutional Animal Care and Use Committee (IACUC). Three Male Sprague Dawley rats (12 weeks old) were obtained from Charles River Laboratories (Wilmington, MA). Rats were individually housed, allowed free access to water, fed standard rat chow pellet, and kept on a 12-hour light-dark cycle. Before the experiments were conducted, the animals were acclimatized for a week at the above conditions. The scaffolds were implanted in subcutaneous pockets using a well established animal surgical model for tissue engineering strategies, using preanesthesia by isoflurane (5%) in % O_2 inhalation and maintained further by 1-2.5% isoflurane. To reduce pre-operative infection risk and to minimize post-operative discomfort, antibiotic (Enrofloxacin (Baytril), 2.5-5 mg/kg SQ for 5 days, s.c) and analgesic (ketorolac 2-4 mg/kg, s.c) were administered to the rats. For the installation of subcutaneous implants, the dorsum of rats was shaved, washed, and disinfected with povidone-iodine. Four longitudinal incisions of ~1 cm were made through the full thickness of the skin at both sides of the spinal column. Subsequently, lateral to the incisions a subcutaneous pocket was created by blunt dissection and then the scaffolds were placed into these pockets. The skin was closed using a subcuticular vicryl suture. Post surgery, the animals were housed singly and allowed full activity in their cages and monitored for any adverse effects.

2. 7 Ultrasound Co-registered Photoacoustic Imaging

US and PA images of PLGA and SWCNT-PLGA scaffolds embedded in chicken breast tissue were taken using Visual Sonics Vevo LAZR Photoacoustics Imaging System (LZ550 imaging probe, 40 MHz center frequency, bandwidth 22-55 MHz). Scaffolds placed on chicken breast tissue were covered with layers of chicken breast of varying thickness (0.5 mm, 2 mm and 6 mm). A thin layer of ultrasound gel was applied on the surface of the chicken breast to reduce attenuation due to air pockets between the skin and transducer. The transducer was placed in contact with the gel. Images were obtained using a 680 nm and 780 nm laser and analyzed using Vevo 2100 Workstation software (v1.4.0).

PA images of the scaffolds *in vivo* were taken at 7 and 14 days post-surgery at 680, 780, 880 and 970 nm wavelengths. The energies of the lasers used for imaging were all within the American National Standards Institute (ANSI) limitation (20 mJ/cm^2). For PA imaging the rats were preanesthetized with isoflurane (5%) in O_2 mixture and maintained under 1-2.5% isoflurane. Animals were placed on flat stationary surface designed for rats on the PA instrument and ultrasound gel was applied for imaging. Photoacoustic signals were detected by placing the transducer on the gel applied portion to perform imaging. Two and three-dimensional images of scaffolds were taken and oxygen saturation levels within the scaffolds were determined using Vevo 2100 Workstation software (v1.4.0). Oxygen saturation (sO_2) measurements were assessed using the Oxyhemo mode, an inbuilt software algorithm, that uses a dual-wavelength (750nm and 850nm) approach.[51] A region of interest (ROI) was created to include the scaffold in the 2D acquired sO2 images.

2. 8 Statistics

Data was analyzed as a ratio of average photoacoustic signal obtained from the scaffold with signal obtained from surrounding tissue. One sample T test was used to determine significance of

difference of signal from the scaffold and surrounding tissue. Furthermore, non-parametric Man Whitney U test was used to analyze significance in difference between PLGA and SWCNT-PLGA groups. Differences with $P<0.05$ are considered significant.

2. 9 Histology

Subcutaneous tissue containing scaffolds were excised and fixed in 10% buffered formalin (pH 7.2), dehydrated through a series of ethanol solutions, embedded in paraffin, and routinely processed for histological analysis. Sections of 5-micron thickness were cut and stained with hematoxylin-eosin (H&E) for histological analysis. The stained tissues were observed through a microscope (Carl Zeiss, Oberkochen, Germany), photographed by a charge-couple device (CCD) camera and histopathological analysis was performed.

Results and Discussions

The studies reported in this article were performed to answer the following questions: 1) Can US-coregistered PA imaging non-invasively characterize PLGA and SWCNT-PLGA scaffolds, and monitor blood oxygen saturation levels in and around these scaffolds? 2) If yes, what are the strengths and weaknesses of this modality for applications mentioned above? PLGA and SWCNT-PLGA scaffolds were chosen since, they have previously been used for *in vitro* PA imaging.[12] Additionally, these scaffolds do not show adverse biological responses *in vitro* and *in vivo.[52, 53]* The NIR wavelengths used for PA imaging were selected to achieve optimal laser power, and PA signal amplitude, as well as greater tissue penetration.

SWCNTs used for the study were characterized by AFM. SWCNT-PLGA scaffolds were characterized using optical microscopy, SEM, and MicroCT. The SWCNTs had a diameter of 1.0-1.5 nm, and had lengths ranging from 1-5 μm (Figure 1A). Figure 1B shows a representative optical image of the PLGA and SWCNT-PLGA scaffold. SWCNT-PLGA scaffolds with SWCNT incorporated throughout the polymer scaffolds appear gray in the optical images and are morphologically similar to PLGA scaffolds. Figure 1C shows a SEM image of SWCNT-PLGA scaffold with SWCNT embedded into the polymer matrix. SWCNTs within the polymer matrix are seen bridging the micro cracks within the scaffold and protruding out from the polymer matrix.[54, 55] Furthermore, microCT image of the scaffold shows a porous structure with inter connecting pores. Analysis shows porosity of about 89% with 145 μm as the average size of the pores.[12]

US-PA imaging of PLGA and SWCNT-PLGA scaffolds was first performed *ex vivo*. Figure 2 shows representative US-coregistered PA images of PLGA and SWCNT-PLGA scaffolds embedded in chicken breast tissue at depths of 0.5, 2, and 6 mm. Regions pseudo-colored in bright red are the PA signals overlaid on black and grey ultrasound images. Anatomical

information obtained from US images was used to determine the position and depth of the scaffolds within the tissue. PLGA scaffolds generated no PA signal at all the depths, except in some regions (Figure 2 A-C). In these regions, the generated PA signals (colored in red) were due to trace amounts of SWCNTs used to indicate the distal lining of chicken breast tissue. SWCNT-PLGA scaffolds showed PA signal intensity up to four times higher than PLGA scaffolds and surrounding tissue and appear red in the images (Figure 2D-F). PA images of the entire scaffold could be obtained at a depth of 0.5 mm and 2 mm. At 6 mm depth, PA images of only the top portion of the scaffold could be obtained, and the entire scaffold could not be imaged at depths below 6 mm. SWCNT-PLGA scaffolds generated strong PA signals at both 680 nm and 780 nm wavelengths, due to the presence of SWCNTs. The 680 nm wavelength laser had a higher power compared to the 780 nm wavelength laser, which resulted in higher fluence and thus, a stronger PA signal. 3D reconstruction of the 2D planar US-PA images allowed better registration of the location and dimensions of the scaffolds. Figure 2G displays 3D reconstructed image of a representative scaffold embedded 0.5 mm deep in the tissue, which clearly shows the scaffold shape and dimensions (4 mm x 1.5 mm). The lateral resolution of the images was 90 μm and axial resolution was 40 μm. The porosity or the pore size of these scaffolds could not be measured from these images, since the pore sizes were ~ 145 μm and pore interconnects were ~ 40-100 μm.[12]

Figure 3 shows US-PA images of PLGA (A & B) and SWCNT-PLGA (C & D) scaffolds implanted subcutaneously in a rat. The scaffolds were imaged on days 7 (A & C) and 14 (B & D) post-surgery. US images obtained from the US-PA Imaging system were used to detect the scaffolds implanted 2 mm deep in subcutaneous pockets on the dorsal region of the rats. The full thickness and the cross-section of the scaffold could be determined in the images. PA signal from endogenous absorbers such as hemoglobin, from as deep as 8 mm was visible in the images. PLGA (Figures 3 A & B) (Figures 3 C &D) scaffolds are indistinguishable in the US-PA images, and have poor contrast with respect to

surrounding tissue. PA signal obtained from PLGA scaffold shows no significant difference compared to signal obtained from surrounding tissue (One sample t test, $P>0.05$). SWCNT-PLGA scaffolds, outlined in Figure 3 C & D, have significantly higher PA intensity compared to surrounding tissue. Average PA intensity of SWCNT-PLGA scaffolds, normalized with PA intensity of surrounding tissue, is 4 times greater than that of PLGA scaffolds (Man Whitney U test, $p<0.05$). Images taken in day 7 and day 14 show no particular trends in signal distribution within the scaffold. Distribution of the PA signal within the scaffold varies based on the 2D slice chosen from the 3D images. 3D rendering of the 2D slices shows the morphology of the scaffold *in vivo* surrounded by endogenous absorbers oxy-and-deoxy hemoglobin (Figure 3E). The epidermal layer produces PA signals due to the presence of melanin and appears as a continuous layer on the surface of the skin. Previous report on PA imaging of scaffolds have applied spectral imaging would allow removal of signal from endogenous absorbers.[56] Since SWCNT has characteristic absorption spectrum, it could easily be delineated from surrounding tissue with spectral imaging and also be quantified.[56] Although NIR lasers with wavelengths between 700 nm-1100 nm have low absorbance and better depth of penetration than visible lasers in biological tissue,[57] biomolecules such as melanin and hemoglobin have significant absorbance at 780 nm wavelength used for *in vivo* PA imaging.[35] In Figure 3E, PA signal from melanin can be seen on the epidermal layer and signal from hemoglobin can be detected in surrounding tissues in Figure 3 A-D. Since PA signal produced from SWCNTs is much stronger than signal produced by these biomolecules,[38, 58] SWCNT-PLGA scaffolds have a very high contrast and can be easily distinguished from surrounding tissue.

Other PA imaging modalities, such as optical or acoustic resolution PAM, possess a better resolution and allow determination of porosity *in vitro*. Optical resolution PAM has a lateral resolution of 2.6 µm, axial resolution of 15 µm with penetration of 660 µm *in vitro* and, 1 mm *in vivo*.[12, 37, 59, 60] Acoustic resolution PAM (AR-PAM) has a spatial resolution of 45 µm, axial resolution of 15 µm with penetration of 2 mm.[12] Compared to PAM, US-PA imaging allows greater tissue penetration, making it more suitable for *in vivo* small animal studies that require deep tissue (> 1 mm) monitoring of scaffolds for applications such as bone or cardiovascular tissue engineering. For these applications, the various PA imaging modalities should provide complementary information at multiple length-scales using the same contrast mechanism.[61] The US-PA imaging should provide anatomy of the tissue surrounding the scaffolds, as well as real-time longitudinal changes in the overall shape, and size of scaffold. Once the scaffolds are explanted, PAM should provide immediate 3D information of changes in pore size and porosity of the explanted scaffolds, and co-validate these scaffold properties *in vitro* during histological and histomorphometric analysis.[12]

Figure 4 shows the blood oxygen saturation maps, at day 7 and 14 post implantation, in and around the PLGA and SWCNT scaffolds. PA signal obtained at 750 nm and 850 nm were used to obtain the blood oxygen saturation maps. Oxygen saturation or dissolved oxygen is the concentration of oxygen in a given media. In the case of blood vessels in biological tissues, it is determined as a ratio of oxy-hemoglobin and total hemoglobin in a given region. Due to the differential absorbance of NIR light by deoxyhemoglobin (Hb) and oxyhemoglobin (HbO) at different wavelengths,[62] relative absorbance of Hb and HbO can be used to determine *in vivo* oxygen saturation with PA imaging.[36] Figures 4 A-D show oxygen saturation maps of the skin and underlying areas. There were regions of high saturation around the PLGA and SWCNT-PLGA scaffolds. PLGA scaffolds showed oxygen saturation on the edges of the scaffold on day 7 (Figure 4A) and at day 14, the regions of high oxygen saturation, appearing red and white, are

also seen within the scaffold (Figure 4B). PLGA scaffolds had lower, oxygen saturation of 12% on day 14 as compared to 16% on day 7. SWCNT-PLGA scaffolds, indistinguishable from surrounding tissue, appear to have high oxygen saturation throughout the scaffold (Figure 4C & D). SWCNT-PLGA scaffolds had 2-3 fold higher oxygen saturation values at both time points with an average oxygen saturation of 41% on day 7 and 36% on day 14. This is due to the additional optical absorbance by the SWCNTs in the scaffolds in the NIR. Unlike Hb and HbO, SWCNT absorbs equivalently at the two NIR wavelengths (750 and 850nm) used for oxygen saturation measurements. SWCNT produces strong PA signal at both wavelengths giving rise to false positive oxygen saturation signal in SWCNT-PLGA scaffolds. Spectroscopic PA imaging can be used to differentiate and quantify SWCNTs as well as Hb and HbO in a given region and eliminate SWCNT-generated false positive signal in the scaffolds.[28, 63] This information can then be used to accurately map blood oxygen saturation of SWCNT-PLGA scaffolds without false positive signal from SWCNTs. Since oxygen saturation is measured from relative concentration of Hb and HbO, it is also a good surrogate indicator of vasculogenesis, and neovascularization.[16] Upon vascularization of the scaffold, there would be an increase in PA signal due to the presence of Hb and HbO within the scaffold. Thus, in small animals, US-PA could provide not only longitudinal anatomical information about the scaffold, but also important physiological information such as Hb, HbO, and oxygen saturation during the process of tissue regeneration.

H&E stained sections of tissue surrounding PLGA and SWCNT-PLGA scaffolds were examined under the microscope to investigate tissue regeneration and vascularization (Figure 5). Surrounding tissue is seen to have penetrated the scaffold with evidence of vascularization around and within the scaffold. The morphology of the regenerated tissue (Figure 5A) matches and validates the oxygen saturation maps obtained *in vivo* (Figure 4B). Red blood cells can be seen in the newly formed capillaries in the regenerated tissue (yellow arrows, Figure 5 A, B, C & D).

Small fragments of the scaffolds were surrounded by newly formed healthy tissue with no signs of fibrosis (red arrows, Figure 5 C & D). SWCNT aggregates can also be seen within the scaffold region surrounded by healthy tissue (green arrows, Figure 5D). The histological results are similar to previous studies that show no adverse host response of highly porous scaffolds, which allow better oxygenation within the scaffolds, of these dimensions.[1, 2, 9]

The above results indicate US-PA imaging should allow longitudinal monitoring of scaffold architecture and oxygen saturation in and around the scaffolds. PLGA is a slowly degrading polymer and previous *in vitro* degradation studies show that scaffolds with similar porosity (89%) and pore size (145 μm) used in this study show negligible degradation.[9] Furthermore, previous *in vitro* studies on similarly prepared scaffolds have shown negligible degradation within two weeks.[12] Histological analysis shows intact PLGA scaffold structures within the regenerated tissue indicating that observed PA signal are mainly from SWCNT incorporated in the scaffolds and not from any SWCNT released from the scaffold. To validate the utility and feasibility of this imaging technique in tissue engineering applications further investigation is required. The effect of varying scaffold parameters such as size, porosity, pore size, degradation kinetics and nanoparticle concentration on imaging tissue regeneration *in vivo* should be investigated. Compared to other multi-modal small animal imaging systems that provide both anatomical and functional imaging, such as MRI-PET and PET-CT, US-PA has significant advantages. It has a higher spatial resolution compared to PET-CT, allowing imaging of vasculature possible, and does not use harmful radiation. Compared to MRI-PET, US-PA has higher temporal resolution allowing real time monitoring of oxygen saturation and does not require exogenous contrast agents for either anatomical or functional imaging.

Our *in vitro* and *in viv*o data provide proof-of-principle demonstration that US-PA imaging hold potential as a preclinical tool for spatial and temporal imaging and characterization of key anatomical and physiological information (structure, and oxygenation) in and around polymeric

scaffolds overcoming the limitations of current structural and histological techniques. Our study in conjunction with reports by others on photoacoustic acoustic microscopy (PAM) indicate that multi-scale PA imaging enhanced with nanoparticle contrast agents has the potential to complement conventional diagnostic approaches for monitoring scaffold structure and vasculogenesis in engineered tissue while overcoming many limitations of existing imaging technologies for small animals. We expect the complete development / adaption of this imaging technique will significantly impact translational research. Tissue engineering scaffolds are biomedical implants. Clinical development of any therapeutic biomedical implant technology is a long and expensive process involving extensive developmental research, animal model testing and then clinical studies. Shortening this development process is critical to managing development-associated costs and time frame. Preclinical non-invasive *in vivo* small animal imaging bridges the gap between *in vitro* exploratory and *in vivo* clinical research facilitating more direct and rapid transfer of preclinical studies in animal models to clinical investigation.[56, 64] Preclinical non-invasive imaging can dramatically increase the efficiency of lead candidate selection by providing earlier and more highly predictive data compared to traditional methods based on histology results alone. Longitudinal imaging of the same animal at multiple time points will result in more valuable information than would be obtained from multiple individual animals. In these systems, the animal acts as its own control and analysis of dynamic data charts progressive biological changes and therapeutic response without need for large numbers of animals. Multi-scale PA imaging, as a non-invasive preclinical modality shows promise to allow longitudinal monitoring and characterization of key structural and tissue regeneration parameters (i.e., size and porosity of scaffolds, neovascularization and oxygen saturation), facilitating more rapid selection of candidate polymeric scaffolds for further development**.** It will also provide important insights into sequence of events that occur during *in vivo* regeneration within polymeric scaffolds, enabling more efficient translation from preclinical testing to clinical evaluation. In addition, low-power photoacoustic imaging is non-ionizing, user-friendly and less expensive than

other 3D small animal imaging modalities used to monitor bone regeneration. Therefore, it is appropriate for use by researchers for rodent studies to improve understanding of the tissue development process, and could be widely adapted for other tissue engineering applications (e.g., skin, bone, and cardiovascular tissue regeneration).

Conclusion

We demonstrate that US-PA imaging allows deep tissue (up to 6 mm) imaging of SWCNT-PLGA scaffolds *ex vivo* with lateral resolution of 90 μm and axial resolution of 40 μm. The modality also allows 2-D and 3D non-invasive longitudinal imaging of SWCNT-PLGA scaffolds subcutaneously implanted into rats. Longitudinal oxygen saturation maps in and around subcutaneously implanted PLGA scaffolds can be obtained using US-PA imaging. Post mortem histological analysis qualitatively corroborates this result. The results suggest that US-PA imaging is a promising multi-modal small animal imaging modality for non-invasive longitudinal monitoring of changes to polymeric tissue engineering scaffold architecture (size, shape, degradation) and key physiological indicators of tissue regeneration such as changes in oxygen saturation.

References

[1] Choi SW, Zhang Y, Thomopoulos S, Xia Y. In vitro mineralization by preosteoblasts in poly(DL-lactide-co-glycolide) inverse opal scaffolds reinforced with hydroxyapatite nanoparticles. Langmuir. 2010;26:12126-31.

[2] Kim SS, Sun Park M, Jeon O, Yong Choi C, Kim BS. Poly (lactide-co-glycolide)/hydroxyapatite composite scaffolds for bone tissue engineering. Biomaterials. 2006;27:1399-409.

[3] Yoshimoto H, Shin Y, Terai H, Vacanti J. A biodegradable nanofiber scaffold by electrospinning and its potential for bone tissue engineering. Biomaterials. 2003;24:2077-82.

[4] Ge Z, Baguenard S, Lim LY, Wee A, Khor E. Hydroxyapatite-chitin materials as potential tissue engineered bone substitutes. Biomaterials. 2004;25:1049-58.

[5] O'Keefe RJ, Mao J. Bone tissue engineering and regeneration: from discovery to the clinic,Äîan overview. Tissue Engineering Part B: Reviews. 2011;17:389-92.

[6] Muzzarelli RA, Greco F, Busilacchi A, Sollazzo V, Gigante A. Chitosan, hyaluronan and chondroitin sulfate in tissue engineering for cartilage regeneration: A review. Carbohydrate polymers. 2012.

[7] Atala A. Tissue engineering of human bladder. British medical bulletin. 2011;97:81-104.

[8] Burg KJL, Porter S, Kellam JF. Biomaterial developments for bone tissue engineering. Biomaterials. 2000;21:2347-59.

[9] Rezwan K, Chen Q, Blaker J, Boccaccini AR. Biodegradable and bioactive porous polymer/inorganic composite scaffolds for bone tissue engineering. Biomaterials. 2006;27:3413-31.

[10] Zhang P, Wu H, Lu Z, Deng C, Hong Z, Jing X, et al. RGD-conjugated copolymer incorporated into composite of poly(lactide-co-glycotide) and poly(L-lactide)-grafted nanohydroxyapatite for bone tissue engineering. Biomacromolecules. 2011;12:2667-80.

[11] Sitharaman B, Avti PK, Schaefer K, Talukdar Y, Longtin JP. A Novel Nanoparticle-Enhanced Photoacoustic Stimulus for Bone Tissue Engineering. Tissue Engineering Part A. 2011;17:1851-8.

[12] Cai X, Paratala BS, Hu S, Sitharaman B, Wang LV. Multiscale photoacoustic microscopy of single-walled carbon nanotube-incorporated tissue engineering scaffolds. Tissue Eng Part C Methods. 2012;18:310-7.

[13] Eltoum I, Fredenburgh J, Myers RB, Grizzle WE. Introduction to the theory and practice of fixation of tissues. Journal of Histotechnology. 2001;24:173-90.

[14] Bancroft JD, Gamble M. Theory and practice of histological techniques: Elsevier Health Sciences; 2008.

[15] Dapson R. Macromolecular changes caused by formalin fixation and antigen retrieval. Biotechnic & Histochemistry. 2007;82:133-40.

[16] Risau W, Flamme I. Vasculogenesis. Annual Review of Cell and Developmental Biology. 1995;11:73-91.

[17] Druecke D, Langer S, Lamme E, Pieper J, Ugarkovic M, Steinau HU, et al. Neovascularization of poly(ether ester) block-copolymer scaffolds in vivo: Long-term investigations using intravital fluorescent microscopy. Journal of Biomedical Materials Research Part A. 2004;68:10-8.

[18] Kellner K, Liebsch G, Klimant I, Wolfbeis OS, Blunk T, Schulz MB, et al. Determination of oxygen gradients in engineered tissue using a fluorescent sensor. Biotechnology and bioengineering. 2002;80:73-83.

[19] Barrilleaux B, Phinney DG, Prockop DJ, O'connor KC. Review: ex vivo engineering of living tissues with adult stem cells. Tissue engineering. 2006;12:3007-19.

[20] D'Ippolito G, Diabira S, Howard GA, Roos BA, Schiller PC. Low oxygen tension inhibits osteogenic differentiation and enhances stemness of human MIAMI cells. Bone. 2006;39:513-22.

[21] Carrancio S, López-Holgado. N, Sánchez-Guijo. FM, Villarón. E, Barbado. V, Tabera. S, et al. Optimization of mesenchymal stem cell expansion procedures by cell separation and culture conditions modification. Experimental hematology. 2008;36:1014-21.

[22] Schenke-Layland K, Riemann I, Damour O, Stock UA, Konig K. Two-photon microscopes and in vivo multiphoton tomographs - Powerful dicagnostic tools for tissue engineering and drug delivery. Adv Drug Deliv Rev. 2006;58:878-96.

[23] C. C-R, El Haj AJ, Yang X, Yang Y. Fluorescent labeling of chitosan for use in non-invasive monitoring of degradation in tissue engineering. Journal of Tissue Engineering and Regenerative Medicine. 2011.

[24] Georgakoudi I, Rice WL, Hronik-Tupaj M, Kaplan DL. Optical spectroscopy and imaging for the noninvasive evaluation of engineered tissues. Tissue Engineering Part B: Reviews. 2008;14:321-40.

[25] Studwell AJ, Kotton DN. A Shift From Cell Cultures to Creatures: In Vivo Imaging of Small Animals in Experimental Regenerative Medicine. Molecular Therapy. 2011.

[26] Wittenborn T, Nielsen T, Nygaard JV, Larsen EKU, Thim T, Rydtoft LM, et al. Ultrahigh-field DCE-MRI of angiogenesis in a novel angiogenesis mouse model. Journal of Magnetic Resonance Imaging. 2012;35:703-10.

[27] Young S, Kretlow JD, Nguyen C, Bashoura AG, Baggett LS, Jansen JA, et al. Microcomputed tomography characterization of neovascularization in bone tissue engineering applications. Tissue Engineering Part B: Reviews. 2008;14:295-306.

[28] Rao B, Maslov K, Danielli A, Chen R, Shung KK, Zhou Q, et al. Real-time four-dimensional optical-resolution photoacoustic microscopy with Au nanoparticle-assisted subdiffraction-limit resolution. Optics letters. 2011;36:1137-9.

[29] Chen WT, Ting Fang Shih T, Chen RC, Tu SY, Wen-Yuen H, Yang PC. Integrin alphavbeta3-Targeted Dynamic Contrast-Enhanced Magnetic Resonance Imaging Using a Gadolinium-Loaded Polyethylene Gycol-Dendrimer-Cyclic RGD Conjugate to Evaluate Tumor Angiogenesis and to Assess Early Antiangiogenic Treatment Response in a Mouse Xenograft Tumor Model. Mol Imaging. 2012;11:286-300.

[30] Haney CR, Fan X, Markiewicz E, Mustafi D, Karczmar GS, Stadler WM. Monitoring Anti-Angiogenic Therapy in Colorectal Cancer Murine Model using Dynamic Contrast-Enhanced MRI - Comparing Pixel-by-Pixel with Region of Interest Analysis. Technol Cancer Res Treat. 2012.

[31] Huang SY, Chen BB, Lu HY, Lin HH, Wei SY, Hsu SC, et al. Correlation among DCE-MRI measurements of bone marrow angiogenesis, microvessel density, and extramedullary disease in patients with multiple myeloma. Am J Hematol. 2012;87:837-9.

[32] O'Connor JPB, Jackson A, Parker GJM, Jayson GC. DCE-MRI biomarkers in the clinical evaluation of antiangiogenic and vascular disrupting agents. British Journal of Cancer. 2007;96:189-95.

[33] van der Zande M, Sitharaman B, Walboomers XF, Tran L, Ananta JS, Veltien A, et al. In vivo magnetic resonance imaging of the distribution pattern of gadonanotubes released from a degrading poly (lactic-co-glycolic acid) scaffold. Tissue Engineering Part C: Methods. 2010;17:19-26.

[34] Sitharaman B, Van Der Zande M, Ananta JS, Shi X, Veltien A, Walboomers XF, et al. Magnetic resonance imaging studies on gadonanotube, reinforced biodegradable polymer nanocomposites. Journal of Biomedical Materials Research Part A. 2010;93:1454-62.

[35] Viator JA, Komadina J, Svaasand LO, Aguilar G, Choi B, Nelson JS. A comparative study of photoacoustic and reflectance methods for determination of epidermal melanin content. Journal of investigative dermatology. 2004;122:1432-9.

[36] Zhang HF, Maslov K, Sivaramakrishnan M, Stoica G, Wang LV. Imaging of hemoglobin oxygen saturation variations in single vessels in vivo using photoacoustic microscopy. Applied physics letters. 2007;90:053901-3.

[37] Cai X, Hu S, Paratala B, Sitharaman B, Wang LV. Dual-mode photoacoustic microscopy of carbon nanotube incorporated scaffolds in blood and biological tissues. International Society for Optics and Photonics2011. p. 78992I-I.

[38] Pramanik M, Song KH, Swierczewska M, Green D, Sitharaman B, Wang LV. In vivo carbon nanotube-enhanced non-invasive photoacoustic mapping of the sentinel lymph node. Physics in medicine and biology. 2009;54:3291.

[39] Xiang L, Yuan Y, Xing D, Ou Z, Yang S, Zhou F. Photoacoustic molecular imaging with antibody-functionalized single-walled carbon nanotubes for early diagnosis of tumor. Journal of biomedical optics. 2009;14:021007-8.

[40] Emelianov SY, Li PC, O'Donnell M. Photoacoustics for molecular imaging and therapy. Physics today. 2009;62:34.

[41] Hu S, Maslov K, Wang LV. Three-dimensional optical-resolution photoacoustic microscopy. J Vis Exp. 2011;3:55.

[42] Aguirre A, Guo P, Gamelin J, Yan S, Sanders MM, Brewer M, et al. Coregistered three-dimensional ultrasound and photoacoustic imaging system for ovarian tissue characterization. Journal of biomedical optics. 2009;14:054014-9.

[43] Bayer CL, Joshi PP, Emelianov SY. Photoacoustic imaging: a potential tool to detect early indicators of metastasis. Expert review of medical devices. 2013;10:125-34.

[44] Emelianov S, Wang B, Su J, Karpiouk A, Yantsen E, Sokolov K, et al. Intravascular ultrasound and photoacoustic imaging. Conf Proc IEEE Eng Med Biol Soc. 2008;2008:2-5.

[45] Mehrmohammadi M, Yoon SJ, Yeager D, Emelianov SY. Photoacoustic Imaging for Cancer Detection and Staging. Curr Mol Imaging. 2013;2:89-105.

[46] Nam SY, Ricles LM, Suggs LJ, Emelianov SY. In vivo ultrasound and photoacoustic monitoring of mesenchymal stem cells labeled with gold nanotracers. PLoS One. 2012;7:e37267.

[47] Sethuraman S, Aglyamov SR, Amirian JH, Smalling RW, Emelianov SY. Intravascular photoacoustic imaging using an IVUS imaging catheter. IEEE Trans Ultrason Ferroelectr Freq Control. 2007;54:978-86.

[48] Shi X, Sitharaman B, Pham QP, Liang F, Wu K, Edward Billups W, et al. Fabrication of porous ultra-short single-walled carbon nanotube nanocomposite scaffolds for bone tissue engineering. Biomaterials. 2007;28:4078-90.

[49] Lalwani G, Henslee AM, Farshid B, Lin L, Kasper FK, Qin Y-X, et al. Two-Dimensional Nanostructure-Reinforced Biodegradable Polymeric Nanocomposites for Bone Tissue Engineering. Biomacromolecules. 2013.

[50] Lalwani G, Kwaczala AT, Kanakia S, Patel SC, Judex S, Sitharaman B. Fabrication and Characterization of Three-Dimensional Macroscopic All-Carbon Scaffolds. Carbon N Y. 2013;53:90-100.

[51] Li C, Wang LV. Photoacoustic tomography and sensing in biomedicine. Physics in medicine and biology. 2009;54:R59.

[52] Shi XF, Sitharaman B, Pham QP, Spicer PP, Hudson JL, Wilson LJ, et al. In vitro cytotoxicity of single-walled carbon nanotube/biodegradable polymer nanocomposites. Journal of Biomedical Materials Research Part A. 2008;86A:813-23.

[53] Sitharaman B, Shi XF, Walboomers XF, Liao HB, Cuijpers V, Wilson LJ, et al. In vivo biocompatibility of ultra-short single-walled carbon nanotube/biodegradable polymer nanocomposites for, bone tissue engineering. Bone. 2008;43:362-70.

[54] Shi X, Hudson JL, Spicer PP, Tour JM, Krishnamoorti R, Mikos AG. Injectable nanocomposites of single-walled carbon nanotubes and biodegradable polymers for bone tissue engineering. Biomacromolecules. 2006;7:2237-42.

[55] Sitharaman B, Shi X, Tran LA, Spicer PP, Rusakova I, Wilson LJ, et al. Injectable in situ cross-linkable nanocomposites of biodegradable polymers and carbon nanostructures for bone tissue engineering. Journal of Biomaterials Science, Polymer Edition. 2007;18:655-71.

[56] Avti PK, Hu S, Favazza C, Mikos AG, Jansen JA, Shroyer KR, et al. Detection, mapping, and quantification of single walled carbon nanotubes in histological specimens with photoacoustic microscopy. PloS one. 2012;7:e35064.

[57] König K. Multiphoton microscopy in life sciences. Journal of Microscopy. 2000;200:83-104.

[58] De La Zerda A, Zavaleta C, Keren S, Vaithilingam S, Bodapati S, Liu Z, et al. Carbon nanotubes as photoacoustic molecular imaging agents in living mice. Nature nanotechnology. 2008;3:557-62.

[59] Cai X, Zhang Y, Li L, Choi SW, MacEwan MR, Yao J, et al. Investigation of Neovascularization in Three-Dimensional Porous Scaffolds In Vivo by a Combination of Multiscale Photoacoustic Microscopy and Optical Coherence Tomography. Tissue Engineering Part C: Methods. 2012.

[60] Maslov K, Zhang HF, Hu S, Wang LV. Optical-resolution photoacoustic microscopy for in vivo imaging of single capillaries. Opt Lett. 2008;33:929-31.

[61] Chen Q, Chen H, Zheng D, Kuang C, Fang H, Zou B, et al. Smad7 Is Required for the Development and Function of the Heart. J Biol Chem. 2009;284:292-300.

[62] Chance B, Borer E, Evans A, Holtom G, Kent J, Maris M, et al. Optical and Nuclear Magnetic Resonance Studies of Hypoxia in Human Tissue and Tumors a. Annals of the New York Academy of Sciences. 1988;551:1-16.

[63] Kim S, Chen YS, Luke GP, Emelianov SY. In vivo three-dimensional spectroscopic photoacoustic imaging for monitoring nanoparticle delivery. Biomedical optics express. 2011;2:2540-50.

[64] Koo V, Hamilton P, Williamson K. Non-invasive in vivo imaging in small animal research. Analytical Cellular Pathology. 2006;28:127-39.

Figures

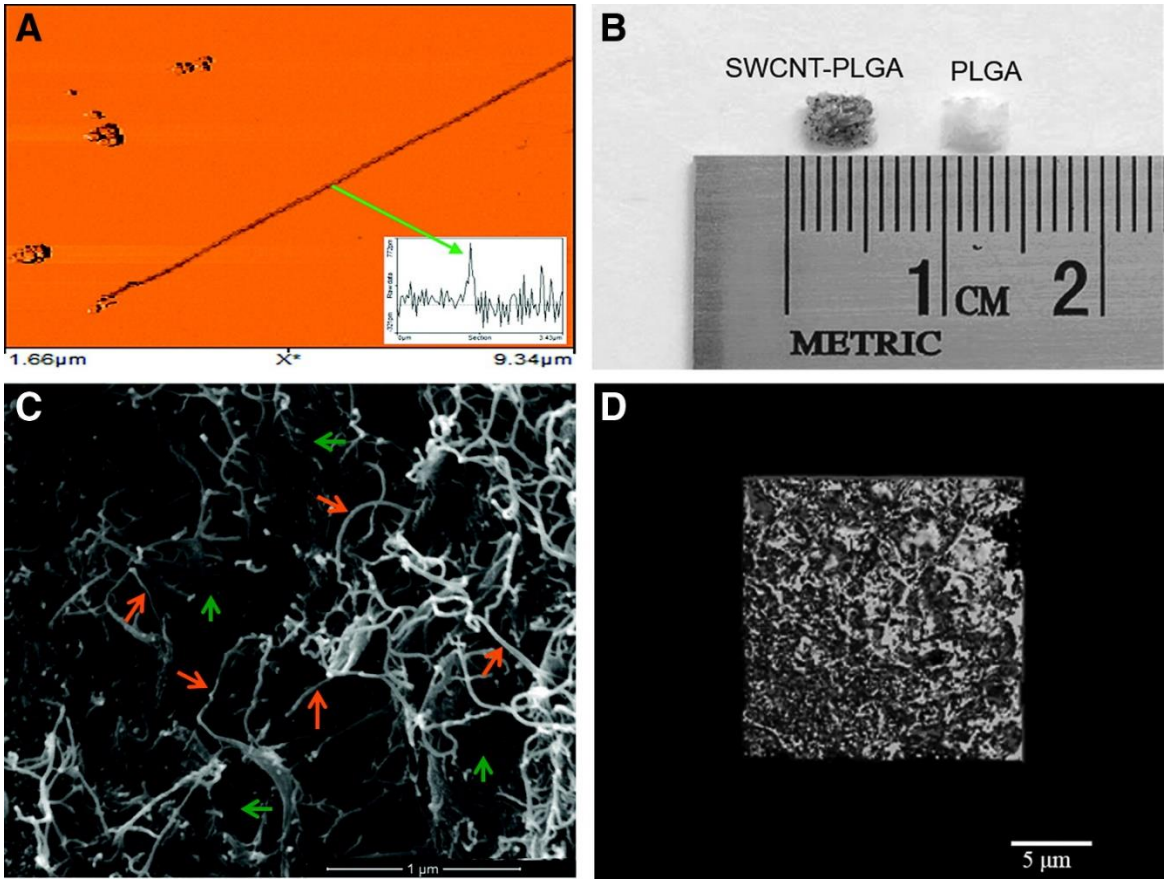

Figure 1: (A) Representative AFM image of a SWCNT. Inset is a cross-sectional topography plot of this nanotube that shows its diameter to be ~ 1 nm. (B) Optical images of PLGA and SWCNT-PLGA (C) SEM images of SWCNT-PLGA scaffold with scale bar showing 1 µm. The orange arrows point to SWCNTs and the green arrows point to PLGA polymer matrix. (D) MicroCT image of SWCNT-PLGA scaffold with scale bar of 5 µm.

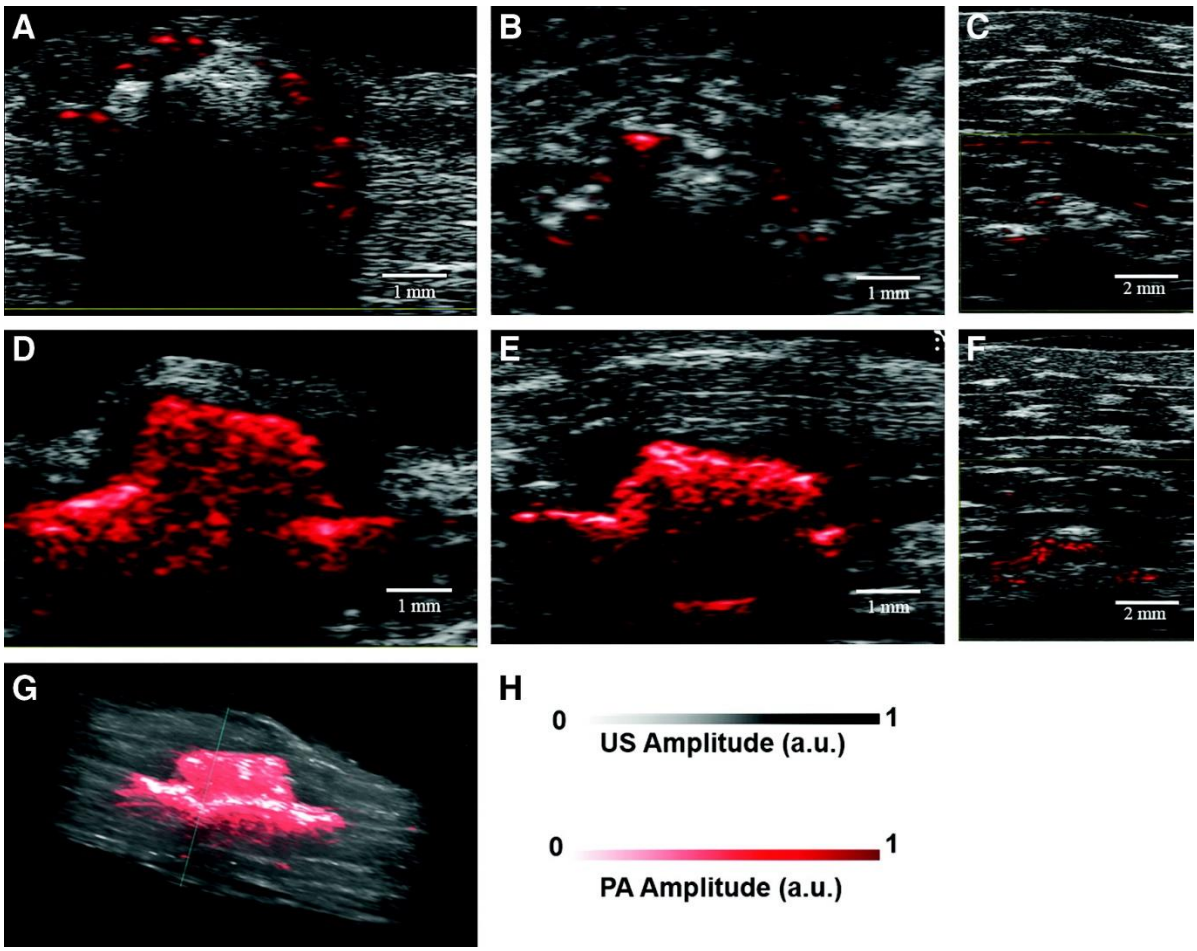

Figure 2: US-PA images of PLGA (A, B & C) and SWCNT-PLGA (D, E and F) scaffold imaged at 680 nm embedded into chicken breast tissue at depths of (A & D) 0.5 mm, (B & E) 2 mm and (C & F) 6 mm. (G) 3D US-PA image rendition of SWCNT-PLGA scaffold embedded 0.5 mm in chicken breast tissue.

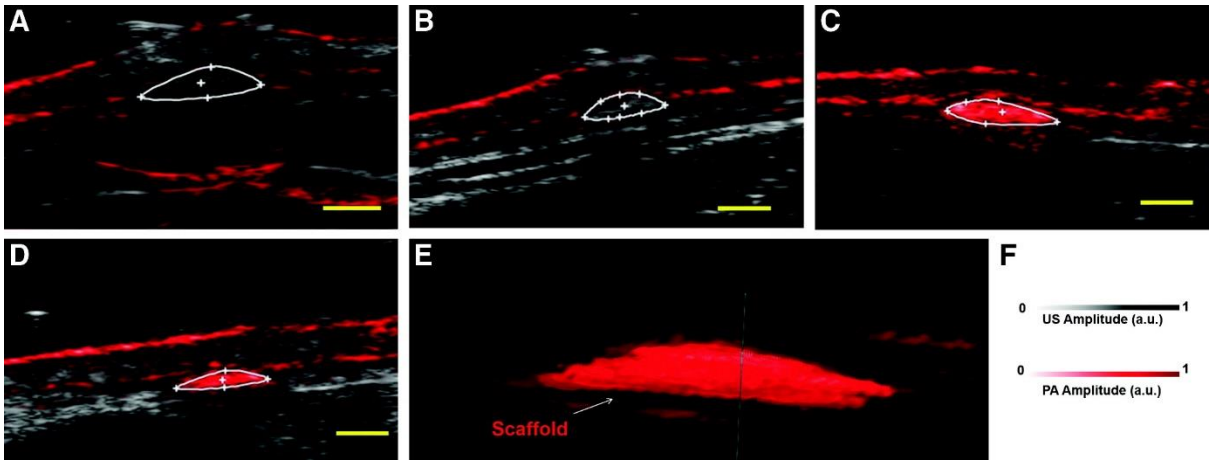

Figure 3: Representative US-PA images of PLGA (A & B) and SWCNT-PLGA (C & D) scaffolds in vivo. The scaffolds were implanted into subcutaneous pockets and imaged on day 7 (A &C) and day 14 (B &D) post-surgery. (E) 3D rendering of SWCNT-PLGA scaffold under the skin at day 7 imaged at 780 nm. Scale bar represents 2 mm.

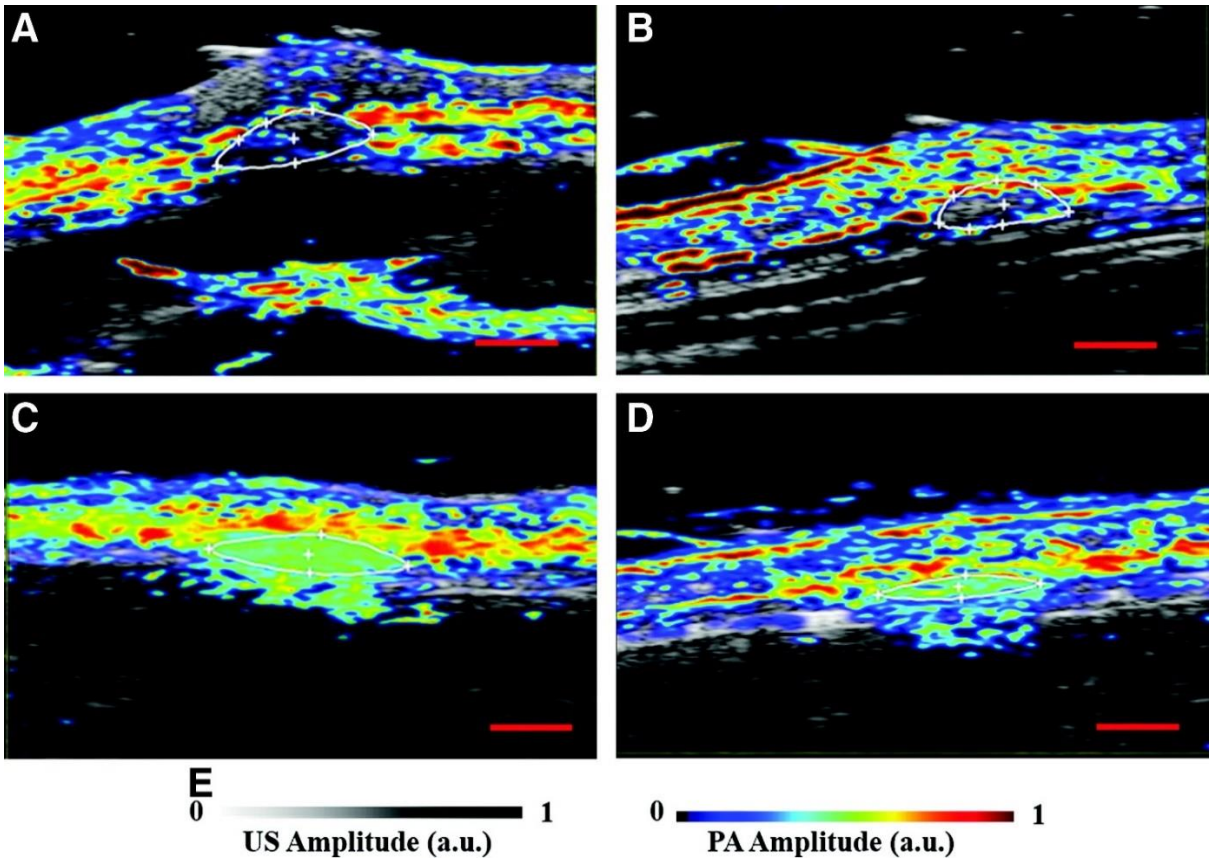

Figure 4: Representative blood oxygen saturation maps of PLGA (A & B) and SWCNT-PLGA (C & D) scaffolds taken day 7 (A & C) and 14 (B &D) post-surgery. Scale bar represents 2 mm.

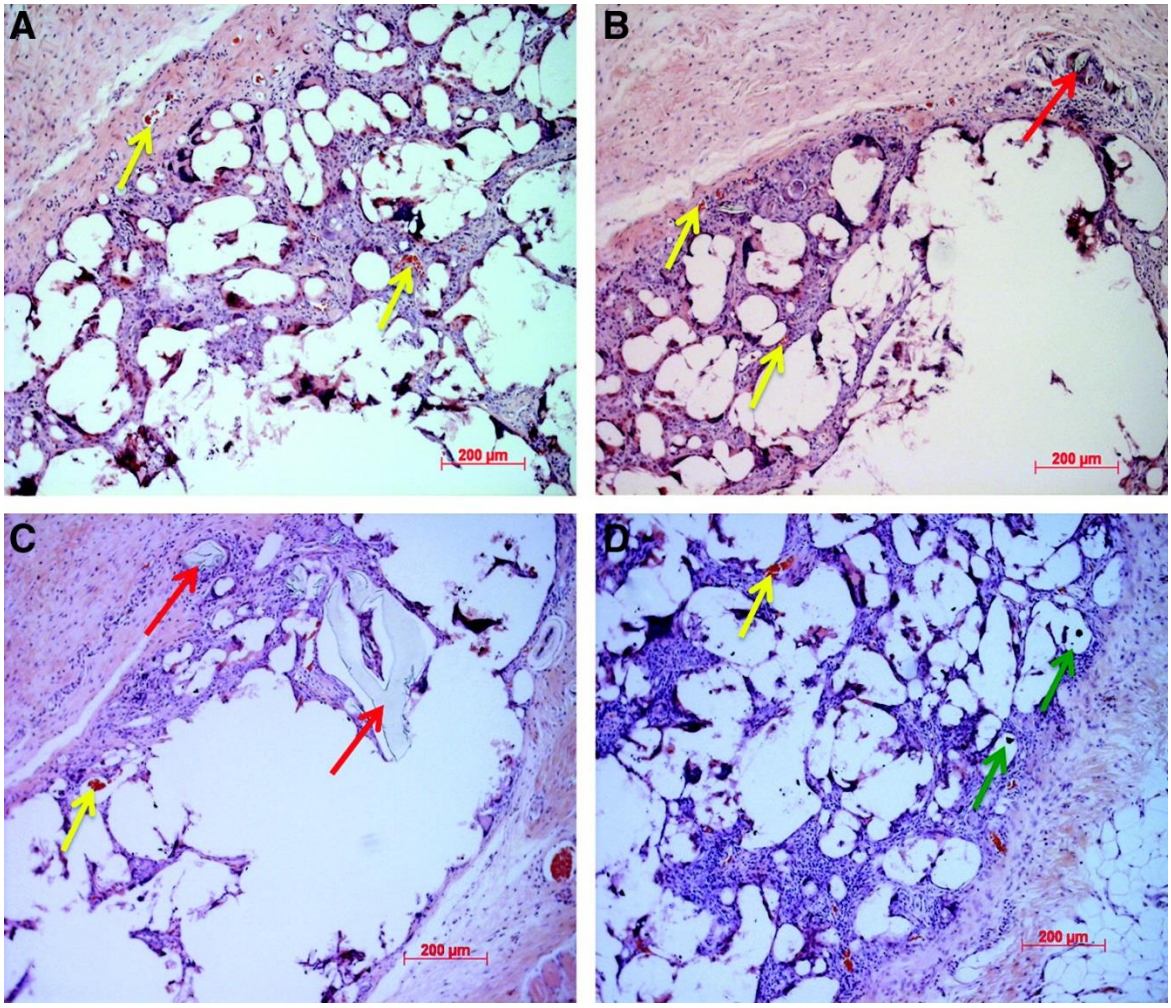

Figure 5: Histology of tissue surrounding PLGA (A & B) and SWCNT-PLGA (C & D) scaffolds showing tissue regeneration and vascularization. Arrows point to scaffold fragments (red arrows), blood vessels (yellow arrows) and SWCNT aggregates (green arrows).

Chapter 4: Carbon Nanoparticle Enhance Photoacoustic Stimulation to Enhance Bone Fracture Healing

Abstract

Stimulus-responsive nanomaterials have mainly been employed to ablate or destroy tissues or to facilitate controlled release of drugs or biologics. Herein, we demonstrate the potential of stimulus responsive nanomaterials to promote tissue regeneration and healing via a non-pharmacological and non-invasive strategy. Thin films of single-walled oxidized graphene nanoribbons (O-SWGNR) were placed on the skin of a rodent femoral fracture site. A nanosecond pulsed laser diode was employed 10 minutes a day for 2 weeks to generate photoacoustic (PA) signals (PAS) from the nanoparticles. Results showed significant increases in bone quantity at the fracture sites of rats exposed to the nanoparticle-generated PAS. In these rats, up to three fold increase in bone volume to callus volume ratio and two fold increase in bone mineral density within the callus were noted, compared to rats that were not exposed to the photoacoustic signals. The results taken together indicate that nanoparticle generated photoacoustic signals serve as an anabolic stimulus for bone regeneration. The results in conjugation with the known ability of these nanoparticles to serve as PA contrast agents suggest opportunities towards the development of integrated non-invasive imaging and non-invasive or invasive treatment strategies for bone loss due to disease or trauma.

Introduction

The physical (electromagnetic, magnetic, acoustic) properties of variety of nanoparticles have been exploited to treat various disease conditions.[1,2] In these treatment strategies, upon stimulation by appropriate external sources (e.g. electromagnetic radiation, magnetism), nanoparticles facilitate the controlled release of therapeutic moieties (drugs, biologics) or transduction of the energy into physical (heat) or chemical (reaction oxygen species) effects that lead to cell or tissue destruction[3]. Very little[4] to no progress has been made in the development of stimulus-responsive nanoparticles that stimulate tissue regeneration.

The photoacoustic (PA) effect - generation of acoustic waves by the absorption of electromagnetic (EM) energy.[5] has been exploited for imaging and therapy. [6] Typically, low intensity EM radiation with fluence that conforms to limits placed by the American National Standards Institute (ANSI) standards have been utilized for PA imaging and high intensity EM radiation has been utilized for PA tissue ablation.[6] A number of nanomaterials such as single-walled carbon nanotubes (SWNTs), gold and graphene nanoparticles with strong intrinsic electromagnetic absorption at visible, near IR wavelengths and in the radiofrequency domain can be used as contrast agents for PA imaging.[7] These nanoparticles could also facilitate PA-stimulated drug delivery.[8]

Previous in vitro studies showed that nanoparticle-enhanced PA signals differentiate multipotent marrow stromal cells (MSCs) towards osteoblasts. However, no *in vivo* study has investigated the efficacy of nanoparticle-enhanced PA effect signals to promote tissue regeneration. *In vivo* bone regeneration is a multistage complex process that requires a

delicate balance of anabolic and catabolic pathways. Herein we present a strategy that utilizes the inherent physical properties of carbon nanoparticles called single walled oxidized graphene nanoribbon (O-SWGNR) to induce anabolism in a rat bone fracture model.

Methods

Synthesis of nanomaterials

SWGONR nanoparticles were synthesized by longitudinally unzipping single walled carbon nanotubes [25] The characterization of these nanoparticles have been reported elsewhere. [26]

Fabrication of O-SWGNR films

SWGONR were mixed into a 1 mg/mL ethyl acetate dispersion and bath sonicated for 1 hour to disperse aggregated particles. The dispersion was fed into a 130kHz ultrasonic spray nozzle with a cylindrical spray shaper (Sonaer Ultrasonics, Farmingdale, NY. USA). Spray coating was performed in a rastering pattern utilizing an automated XYZ gantry. The suspensions were coated onto 12 mm diameter glass coverslips. Inert nitrogen gas was fed into the spray shaper as the carrier gas. While spray coating, the glass circles were clamped by an aluminum vacuum chuck. The vacuum chuck sat on top of an aluminum hotplate with a set point temperature of 135°C. The coated cover slips were then sandwiched between two films of Tegaderm^{TM} (3M^{TM} Nexcare, Maplewood, MN).

Atomic Force Microscopy

O-SWGNR films were imaged with a NanoSurfEasyScan 2 Flex AFM (NanoScience Instruments Inc, Phoenix, Az) using a V-shaped cantilever (APP Nano ACL – 10, frequency fc 145-230 kHz, L=225 µm, W = 40 µm, tip radius < 10 µm, spring constant k

= 20-95 N/m) in tapping mode under ambient conditions of 50% relative humidity and 25º C.

Raman Spectroscopy

O-SWGNR films were analyzed by Raman spectroscopy (Enwave Optronics, Irvine, CA) using a 40x objective and 532 nm laser source. Point spectra were acquired from 500-3000 cm^{-1}.

Photoacoustic characterization

O-SWGNR film was placed 2 cm away from a 905 nm standard pulsed laser diode (OSRAM, Munich, Germany) pulsed at 20 kHz frequency. Absorption of NIR light was verified with a digital power meter (Thorlabs, Newton, NJ). Production of ultrasound was verified using a high frequency delay line ultrasonic transducer (Olympus, Center Valley, PA) and oscilloscope (Fluke, Everett, WA).

Animal model

Female Sprague dawley rats (200 - 225 g) were used for this study (n = 6). Femoral fractures were induced using a standard technique using a Bonnarens and Einhorn fracture induction system.[27] Briefly, all animals were anesthetized by Isoflurane (1-2.5%) in an O_2/Air mixture by inhalation and a small skin incision was made in the knee and the patella was deflected. A hole was drilled into the intercondylar notch and a kirschner wire (1.1 mm, Smith and Nephew Richards, Memphis, TN, USA) was inserted into the medullary cavity. The muscle and skin were then sutured in layers with absorbable suture. Unilateral closed femoral fractures were made in all the groups. For fracture

induction, femur was placed in a three-point bending device and a 500 g weight dropped from a height of 35 cm. X-ray images of the fracture were used to confirm transverse fractures at the diaphysis of the femur. The rats were given buproprion analgesics (0.015 mg/ml, dose 0.05 mg/kg) for pain relief and allowed unrestricted ambulation around the cage.

Photoacoustic stimulation

All PAS stimulation was carried out on rats anesthetized by Isoflurane (1-2.5%) in an O_2/Air mixture by inhalation. After anesthetic induction, the hair around the proximal tibia/distal femur was shaved to allow dermal exposure. A transparent ultrasound coupling gel was applied to the skin over the fracture site and a O-SWGNR film was placed on top. A 60 ns pulsed, near infrared light (905 nm) stimulated the film at 20 kHz frequency. The rats were stimulated for 10 minutes daily for two weeks. At the end of the study, all the groups were euthanized using carbon dioxide inhalation. Femur was collected from each rat for MicroCT analysis and histology. Krishner wire was removed from the intramedullary canal and soft tissue surrounding the bone was removed before analysis.

MicroCT analysis

The fracture site in each femur was scanned using Sanco µCT 4 with an energy of 55 kVp, current of 145 µA. This produced a resolution of 15μm^3 voxel size. Fracture analysis was done on 600 slices from each sample. Analysis of regions proximal and distal to the fracture was done on 100 slices on respective fracture ends. The outer boundary of the callus was defined and the outlined area in each slice was used for

analysis. We gaussian filtered (σ= 1.2, support = 1) the grey scale images and applied 0-225, 225-330 and 331-700 threshold values to produce segmented images of the entire bone, dense new bone and calcified cartilage, and very dense cortical bone respectively. We used manufacture provided software to determine total volume (TV), bone volume (BV), bone volume fraction (BV/TV).

Histomorphometric analysis

Rat femurs were decalcified with ethylenediaminetetraacetic acid and embedded in paraffin for sectioning. Sections of 10 μm thickness were then stained with masson's trichrome and imaged using a BX-51 Olympus microscope (Hamburg, Germany). Cartilage area and callus area were outlined and area calculated using ImageJ software (US NIH, Bethesda, MD).

Statistical Analysis

Statistical analysis was performed with student t-test. Differences in mean, between PA stimulated experimental group and non-stimulated control groups, with $P < 0.05$ was considered statistically significant. All results are reported as mean ± standard deviation.

Results and Discussion

In this study, transverse closed fractures in rats were stimulated with PAS stimulation. PAS was generated by stimulating O-SWGNR films with high frequency pulsed NIR laser. The generation of ultrasonic PAS was validated by transducers prior to stimulating the animals. O-SWGNR particles have excellent PA properties[9] that are superior to single walled carbon nanotubes that were previously used in *in vitro* PAS studies.[10,11] NIR light was used for the study due to its high penetration depth in biological tissue compared to visible light. O-SWGNR films were coated on 12 mm glass cover slips using ultrasonic spray deposition technique.[12] Figure 1A displays a digital image of a O-SWGNR film sandwiched with Tegaderm^{TM} – a transparent polyurethane membrane that allows moisture and air to pass through but prevents passage of larger particles. Tegaderm^{TM} were used to prevent direct contact of the nanoparticle with the skin during stimulation. AFM image of the film (Figure 1B) shows a uniform coating of the glass surface with SWGONR feature sizes congruent with dispersed individual O-SWGNR particles. Raman spectra of the films following spray coating showed characteristic peaks for O-SWGNR at 1340 cm^{-1} (D band) and 1580 cm^{-1} (G band) (Figure 1C).

The goal of the fabrication process was to create films that allowed little to no NIR light to pass through. This was achieved by coating the glass cover slips with 50 passes of ultrasonic spray nozzle. The films transmitted only 10% of NIR light (905 nm wavelength) with intensity of NIR light passing through the films, placed 2 cm away from the laser diode, measured to be 3.5 mW/cm^2, which is significantly below the ANSI time-averaged intensity limit of 300 mW/cm^2 for NIR light.[13] Each pulse of NIR light

shown in Figure 1B produced a corresponding ultrasonic pulse from the O-SWGNR film (Figure 1C).

A closed transverse fracture on Sprague dawley rats was used as a suitable animal model for this study. The experimental groups (PA) consisted of rats with transverse fractures stimulated for 10 minutes daily with O-SWGNR enhance PAS and the control groups (CON) consisted of rats with fractures that were not stimulated with PAS. The PAS stimulations were performed with a 905 nm laser diode at a pulse rate of 20 kHz with a pulse width of 60 ns. O-SWGNR films were placed directly above the fracture site using an ultrasound coupling gel to ensure minimal attenuation of the PAS signals generated from the film. The laser diode was placed 2 cm above the O-SWGNR film for maximum coverage of the film surface (Figure 1D). The animals were kept under anesthesia using isofluorane gas during the procedure to ensure minimal movement during the stimulation. Fracture healing was assessed after 2 with microCT and histology.All animals showed normal activity and recovered full weight bearing capabilities within a few hours of the surgery. There were no significant differences in body weight between the groups throughout the duration of the study.

Figure 2 shows representative 3D rendition of fracture sites from CON (A) and PA (B) groups following 2 weeks of stimulation. The images show the gross morphology of the fracture site with a longitudinal cross section showing cortical bone (#) surrounded by newly formed woven bone (*). The fracture can be seen as a discontinuity in the cortical bone in the cross-section view. PA groups in general had smaller callus volume compared to CON after two weeks of stimulation. Longitudinal cross sections showed higher

degree of calcification of callus in PA groups compared to CON. PA group had smaller overall volume and thicker dense cortical bones at the fracture site.

Fracture healing process was quantitatively analyzed by measuring total volume (TV), bone volume over total volume (BV/TV) and bone mineral density (BMD). The healing process begins with the formation of a cartilaginous callus. The callus then starts to calcify and forms woven bone surrounding the fracture site. This process is analyzed by measuring the BV/TV of calcified cartilage and woven bone. The woven bone is then organized into lamellar bone producing dense cortical bone. The extent of healing is dependent on the quantity of bone formation within the callus, the density of the bone, as defined by BMD and whether the newly formed bone connected the proximal and distal ends of the fracture. Overall, PA groups showed a greater extent of healing compared to CON groups. MicroCT analysis of whole callus showed 44% higher BV/TV of dense cortical bone in PA groups compared to CON (Figure 2C iii) following two weeks of stimulation ($p = 0.04$). Total volume, BV/TV of calcified cartilage and new bone, and bone mineral density (BMD) showed no statistical differences between the groups (Figure 2C i, ii & iv).

The results of this study suggest PAS stimulations positively affect fracture healing leading to a faster mineralization and maturation of the callus. Following two weeks of stimulation, PA groups had smaller callus volume compared to CON due to accelerated maturation of the callus in PA groups. The fracture sites of PA groups had 44% more dense cortical bone and had already started to remodel leading to a smaller callus volume.

Histological analysis of the fracture sites is congruent with findings from microCT. All groups showed secondary fracture healing characterized by cartilaginous callus (CA) formation followed by intramembranous and endochondral ossification. At two weeks, both groups had varying degrees of periosteal woven bone (WB) within the cartilaginous tissue filled callus (Figure 3 A & B). PA group had more intramembranous bone (IB) formation compared to CON. Following two weeks of stimulation, CON group had two animals with remaining cartilage and woven bone at the fracture site with one of the two animals having incomplete bridging. Only one animal in PA group had some remaining cartilage and woven bone resulting in incomplete bridging.

Histology slides were quantitatively analyzed by measuring the amount of cartilage area compared to the callus area (Figure 3C). PA group had 26% less total callus area (TCA) and half the cartilage area (CA) compared to CON. Ratio of CA/TCA of PA was 37% lower than CON. The difference in CA and CA/TCA were found to be statistically significant (t-test, $p = 0.005$ and 0.015 respectively). Difference in TCA was not found to be statistically significant (t-test, $p = 0.12$). PA groups with smaller regions of cartilage in callus and higher amounts of intramembranous and woven bone show more bone healing and callus maturation. The fracture site was subdivided into proximal and distal ends with 100 microCT slices each. During fracture healing calcification of the cartilage and formation of woven bone initiates at the proximal and distal ends and slowly propagates towards the center leading to bridging of the two sections of the bone. The proximal end of the callus, which is closer to the hip joint, showed PA groups had 48% lower TV compared to CON for 2 week groups ($p = 0.00067$). BV/TV of calcified cartilage and dense cortical bone of PA groups were higher by 60% and 213% respectively compared

to CON (p= 0.003 and 0.0006). BMD was 88% higher in PA compared to CON (p = 0.0005).

Analysis of the distal end of the callus, the end closer to the knee joint, showed similar trends to the proximal end. Following two weeks of stimulation, PA groups had 28% lower TV compared to CON (p= 0.04). BV/TV of calcified cartilage and new bone in PA was 59% higher compared CON (p= 0.047). BV/TV of dense cortical bone was higher by 93% (p = 0.03). BMD was also higher in PA by 55% compared to CON (p= 0.039).

The results clearly indicate that dense cortical bone and bone mineral density were all significantly higher in PA groups compared to the CON group at two weeks. This is because at the edge of the calluses, bone formation occurs by the process of intramembranous ossification, where MSCs in the periosteum proliferate and differentiate into osteoblast that are responsible for bone matrix formation.[14] This process leads to the formation of trabecular bone growth at the distal and proximal ends separated by cartilaginous callus at the middle. Interestingly, BV/TV of dense cortical bone and BMD in proximal end were significantly higher than that of the distal end for PA groups. There were no such differences found for the CON groups. Fractures in femurs heal from distal to proximal end [15] with callus formation originating from the distal end. Therefore, proximal end having more bone quantity compared to distal end is unlike normal fracture healing. This phenomenon cannot be explained by differential blood supply since proximal end of the fracture usually has lower blow flow compared to the distal end.[16] Neither can it be explained by differential access to MSCs since both regions are in the diaphysis and are equally exposed to intramedullary marrow. Since bone formation is a balance between anabolic and catabolic events, an increase in bone quantity could also be

due to a decrease in bone resorption as opposed to increased bone formation. Further investigations in the cellular and molecular mechanism would be required to elucidate the effect of PAS on bone formation and resorption within the callus.

Healing a bone fracture is a multistage complex process that requires a delicate balance of anabolic and catabolic pathways. Healing occurs naturally in healthy individuals with non-critical sized bone defects. In cases where anabolic pathways are compromised due to disease or increased size of defect, various pharmacological or mechanical stimulations can be used to enhance healing. Non-pharmacological mechanical stimulations are favored over pharmacological interventions due to their non-invasive, localized application which limits systemic side effects. Stimulation of bone defects with low intensity pulsed ultrasound (LIPUS) has been shown to enhance regeneration.[17,18] LIPUS increases recruitment, proliferation and differentiation of mesenchymal stem cells (MSC) into osteoblasts at fracture sites.[19,20] PAS stimulation of nanoparticles could be employed in enhancing anabolism in fracture healing.

The underlying rationale for the current study is the propensity of various sources of low intensity electromagnetic (continuous or pulsed laser) and mechanical (ultrasound, mechanical vibrations) signals to promote osteogenesis. There are a few limitations for this study. Firstly, the effect of PAS signal without enhancement with carbon nanoparticle was not investigated in this study. Only 10% of the NIR light intensity is transmitted through the O-SWGNR films. Stimulation with pulsed laser has been shown to increase proliferation and differentiation of osteoblasts [21,22]. However, *in vitro* studies with PAS effect on mesenchymal showed significantly higher efficacy in enhancing osteodifferentiation with carbon nanoparticles than without.[10,11] Secondly, bone

resorption was not investigated in this study. Fracture healing requires bone resorption for remodeling. This process has been shown to be affected by laser and ultrasonic stimulation.[23] [24] Following this proof of concept study, further studies need to be done in order to answer these questions.

The results of this study, for the first time, demonstrate the anabolic effects of nanoparticle enhanced PAS in fracture healing *in vivo*. PA stimulation increased BV/TV of new cortical bone by three folds and BMD by two folds following two weeks of 10 minute daily stimulation. The biological mechanisms that mediate fracture healing need to be investigated extensively to elucidate the mechanism by which nanoparticle enhanced PAS increases healing in bone. PA stimulation in conjunction with nanocomposites, that have nanoparticles embedded within a polymeric tissue engineering scaffolds, could potentially lead to the development of anabolic tissue engineering constructs that can be stimulated to promote tissue regeneration. The findings of this study could potentially lead to the development of a device implant combined therapy for healing difficult to heal non-union bone defects. Even though, in this study NIR laser was used to stimulate O-SWGNR films place superficially over the skin, it could potentially be used for applications that required stimulation of nanoparticle implants placed subcutaneously or within a bone defect.

References

1 Montesi, M., Panseri, S., Iafisco, M., Adamiano, A. & Tampieri, A. Effect of hydroxyapatite nanocrystals functionalized with lactoferrin in osteogenic differentiation of mesenchymal stem cells. *Journal of biomedical materials research Part A* **103**, 224-234 (2015).

2 Zhang, Y., Wei, L., Miron, R. J., Shi, B. & Bian, Z. Anabolic Bone Formation Via a Site-Specific Bone-Targeting Delivery System by Interfering With Semaphorin 4d Expression. *Journal of Bone and Mineral Research* **30**, 286-296 (2015).

3 Hou, J., Mi, M., Wei, M. & Yi, W. [Photothermal effects of metallic carbon nanotubes on human breast cancer cells]. *Yao xue xue bao= Acta pharmaceutica Sinica* **50**, 980-985 (2015).

4 Ha, S.-W., Sikorski, J. A., Weitzmann, M. N. & Beck, G. R. Bio-active engineered 50nm silica nanoparticles with bone anabolic activity: Therapeutic index, effective concentration, and cytotoxicity profile in vitro. *Toxicology in Vitro* **28**, 354-364 (2014).

5 Xu, M. & Wang, L. V. Photoacoustic imaging in biomedicine. *Review of Scientific Instruments* **77**, 041101-041122 (2006).

6 Emelianov, S. Y., Li, P.-C. & O'Donnell, M. Photoacoustics for molecular imaging and therapy. *Physics Today* **62**, 34-39, doi:10.1063/1.3141939 (2009).

7 Weber, J., Beard, P. C. & Bohndiek, S. E. Contrast agents for molecular photoacoustic imaging. *Nat Meth* **13**, 639-650, doi:10.1038/nmeth.3929

8 Jun, X., Chulhong, K. & Jonathan, F. L. Opportunities for Photoacoustic-Guided Drug Delivery. *Current Drug Targets* **16**, 571-581, doi:http://dx.doi.org/10.2174/1389450116666150707100328 (2015).

9 Lalwani, G., Cai, X., Nie, L., Wang, L. V. & Sitharaman, B. Graphene-based contrast agents for photoacoustic and thermoacoustic tomography. *Photoacoustics* **1**, 62-67 (2013).

10 Green, D. E., Longtin, J. P. & Sitharaman, B. The effect of nanoparticle-enhanced photoacoustic stimulation on multipotent marrow stromal cells. *ACS nano* **3**, 2065-2072 (2009).

11 Sitharaman, B., Avti, P. K., Schaefer, K., Talukdar, Y. & Longtin, J. P. A novel nanoparticle-enhanced photoacoustic stimulus for bone tissue engineering. *Tissue Engineering Part A* **17**, 1851-1858 (2011).

12 Patel, S. C., Lalwani, G., Grover, K., Qin, Y.-X. & Sitharaman, B. Fabrication and cytocompatibility of in situ crosslinked carbon nanomaterial films. *Scientific reports* **5** (2015).

13 in *ANSI Z136* (ed Orlando Laser Institue of America, Fl) 2000 (200).

14 Gerstenfeld, L. C., Cullinane, D. M., Barnes, G. L., Graves, D. T. & Einhorn, T. A. Fracture healing as a post-natal developmental process: Molecular, spatial, and temporal aspects of its regulation. *Journal of cellular biochemistry* **88**, 873-884 (2003).

15 Gerstenfeld, L. C. *et al.* Three-dimensional reconstruction of fracture callus morphogenesis. *Journal of Histochemistry & Cytochemistry* **54**, 1215-1228 (2006).

16 Grundnes, O. & Reikerås, O. Blood flow and mechanical properties of healing bone: Femoral osteotomies studied in rats. *Acta Orthopaedica Scandinavica* **63**, 487-491 (1992).

17 Rutten, S., Nolte, P. A., Korstjens, C. M., van Duin, M. A. & Klein-Nulend, J. Low-intensity pulsed ultrasound increases bone volume, osteoid thickness and mineral apposition rate in the area of fracture healing in patients with a delayed union of the osteotomized fibula. *Bone* **43**, 348-354 (2008).

18 Jingushi, S., Mizuno, K., Matsushita, T. & Itoman, M. Low-intensity pulsed ultrasound treatment for postoperative delayed union or nonunion of long bone fractures. *Journal of Orthopaedic Science* **12**, 35-41 (2007).

19 Kusuyama, J. *et al.* Low intensity pulsed ultrasound (LIPUS) influences the multilineage differentiation of mesenchymal stem and progenitor cell lines through ROCK-Cot/Tpl2-MEK-ERK signaling pathway. *Journal of Biological Chemistry* **289**, 10330-10344 (2014).

20 Wei, F.-Y. *et al.* Low intensity pulsed ultrasound enhanced mesenchymal stem cell recruitment through stromal derived factor-1 signaling in fracture healing. *PLoS One* **9**, e106722 (2014).

21 Oliveira, F. A. *et al.* Low intensity lasers differently induce primary human osteoblast proliferation and differentiation. *Journal of Photochemistry and Photobiology B: Biology* **163**, 14-21 (2016).

22 Shingyochi, Y. *et al.* A Low-Level Carbon Dioxide Laser Promotes Fibroblast Proliferation and Migration through Activation of Akt, ERK, and JNK. *PloS one* **12**, e0168937 (2017).

23 Feres, M. F. N., Kucharski, C., Diar-Bakirly, S. & El-Bialy, T. Effect of low-intensity pulsed ultrasound on the activity of osteoclasts: An in vitro study. *Archives of Oral Biology* **70**, 73-78 (2016).

24 Liu, Z., Xu, J., E, L. & Wang, D. Ultrasound enhances the healing of orthodontically induced root resorption in rats. *The Angle orthodontist* **82**, 48-55 (2011).

25 Kosynkin, D. V. *et al.* Longitudinal unzipping of carbon nanotubes to form graphene nanoribbons. *Nature* **458**, 872-876 (2009).

26 Lalwani, G. *et al.* Two-Dimensional Nanostructure-Reinforced Biodegradable Polymeric Nanocomposites for Bone Tissue Engineering. *Biomacromolecules* **14**, 900-909 (2013).

27 Bonnarens, F. & Einhorn, T. A. Production of a standard closed fracture in laboratory animal bone. *Journal of orthopaedic research* **2**, 97-101 (1984).

Figures

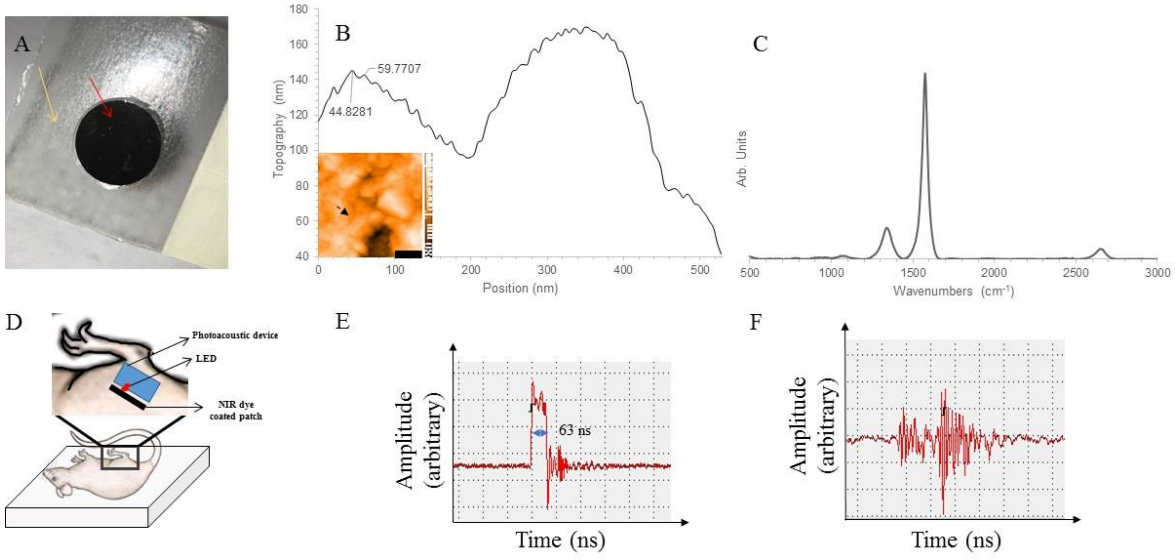

Figure 1: Characterization of oxidized single walled graphene nanoribbon(O-SWGNR) films and schematic of protocol used for photoacoustic stimulation. (A) Representative optical image of GONR films coated on glass cover slips (red arrow) covered with water proof polyurethane Tegaderm^{TM} film (yellow arrow) (B) Line plot of the region with the dotted line showing feature sizes observed in the AFM image (inset) with black scale bar of 1 micron referring to the x-y scale (C) Raman spectra of graphene oxide nanoribbons. (D) O-SWGNR film placed over fracture site on a rat femur stimulated with a NIR laser diode (E) Width of the input current pulse measured from the electric input for the NIR laser diode used for PA stimulation. (F) Ultrasound pulse generated from O-SWGNR film upon stimulation with a single pulse of NIR light.

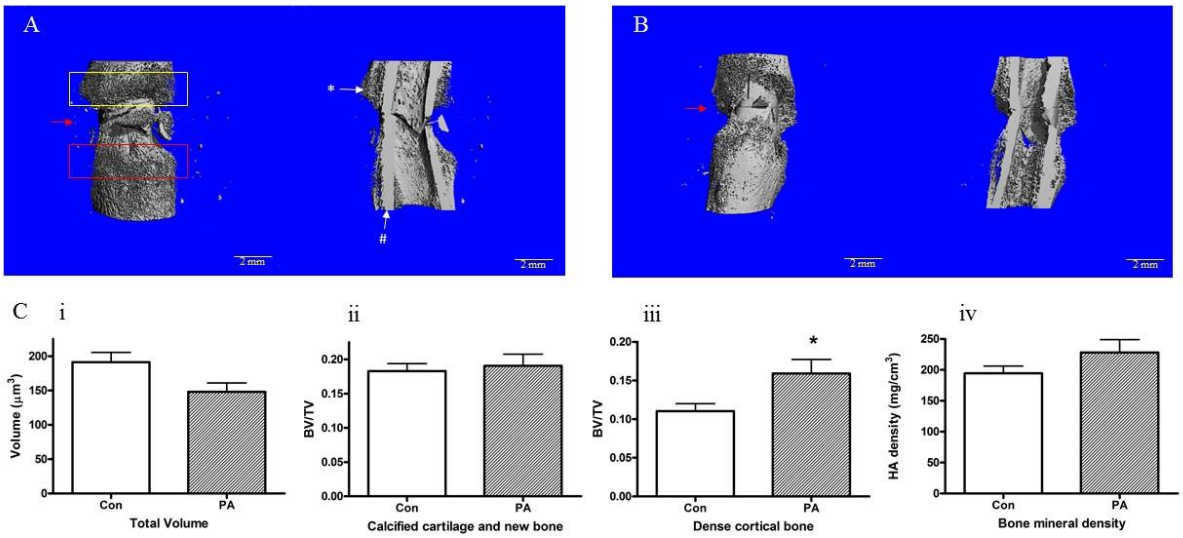

Figure 2: Three dimensional microCT rendition of rat femur fracture sites, two weeks following surgery, of non-stimulated CON (A) and stimulated PA groups (B). The whole callus area is shown with proximal and distal ends marked with yellow and red boxes respectively. Cut plane views show old cortical bone (#) and newly formed woven bone in callus (*). Red arrows indicate regions of incomplete bridging. Scale bar represents 2 mm. (C) MicroCT analysis of the fracture site of the two groups showing (i) Total volume, (ii) BV/TV of calcified cartilage and new bone, (iii) BV/TV of dense cortical bone and (iv) bone mineral density of whole callus formed at fracture site. Statistical significance, denoted by (*), was determined by two-tailed, unpaired student t-test with $p<0.05$

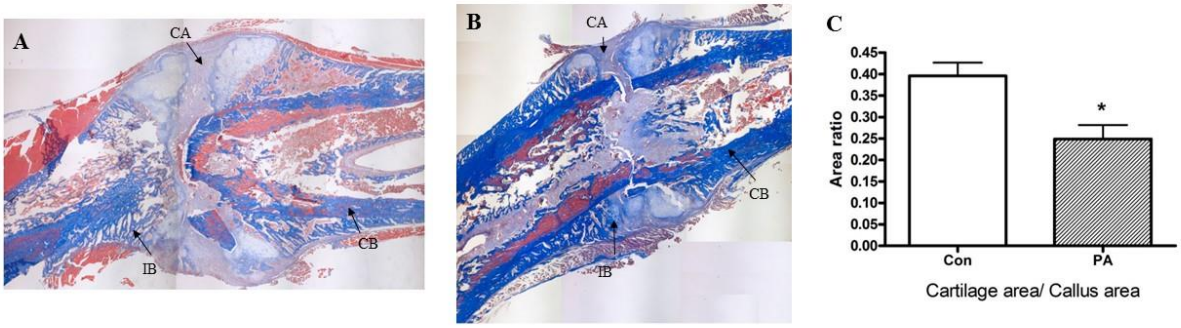

Figure 3: Representative histological sections of fracture site from (A) non-stimulated controls and (B) photoacoustic stimulated groups two weeks following surgery stained with masson's trichrome. Cartilage (CA), intramembranous bone (IB), and cortical bone (CB) are indicated with arrows. (C) Graph shows cartilage area normalized to callus area of the two groups. Statistical significance, denoted by (*), was determined by two-tailed, unpaired student t-test with $p<0.05$

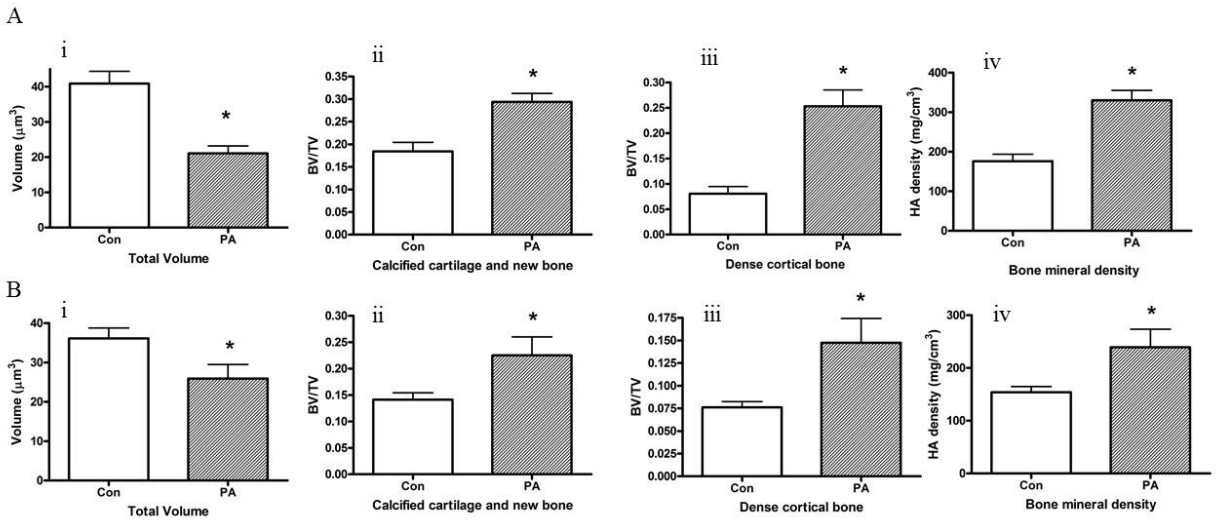

Figure 4: MicroCT analysis of the proximal (A) and distal (B) end of the fracture site of non-stimulated controls and photoacoustic stimulated (PA) groups two weeks following surgery. (i) Total volume, (ii) BV/TV of calcified cartilage and new bone, (iii) BV/TV of dense cortical bone and (iv) bone mineral density of callus formed at the proximal end of the fracture site. Statistical significance, denoted by (*), was determined by two-tailed, unpaired student t-test with $p<0.05$

Chapter 5: Conclusion and Future Direction

The aim of this dissertation was to investigate the use of nanoparticle enhanced PA in regenerating bone tissue and to demonstrate its utility in *in vivo* imaging. PA is investigated for imaging applications and has never been considered as an anabolic stimulus for tissue regeneration. This is the first time PA stimulus has enhanced bone healing in an *in vivo* model. It sets up premises to develop a combined device implant therapy to treat critical sized bone defects caused by disease or trauma. Furthermore, the findings from this dissertation have implications within and outside the field of bone tissue engineering.

In the first aim, we investigated the effect of treating MSCs with graphene nanoparticles of varying 2 dimensional morphologies. These nanoparticles have interesting physicochemical properties that make them desirable for tissue engineering applications. When incorporated in tissue engineering scaffolds, these particles increase surface roughness which facilitates cell adhesion[1] and increase scaffold mechanical strength [2]. Our results indicate that treating MSCS with GNO, GONP and GONR carbon nanoparticles in up to 50 μg/ml DSPE-PEG dispersions have no effect on viability for at least 72 hours. Furthermore, they do not affect osteodifferentiation of MSCs when incubated for 24 hours. Interestingly, the varying morphologies lead to differential uptake by MSCs. GONR was not taken up into the cells where as GONP and GNO were. This finding could be used to choose graphene nanoparticles in developing applications that require uptake of nanoparticles, such as drug or gene delivery, or avoid uptake from nanocomposite scaffolds or PA enhancing thin films.

The findings from this study have opened avenues for further research in the use of graphene nanoparticles in bone tissue engineering. GONP and GONR incorporated poly (propylene fumarate) (PPF) nanocomposites were tested for *in vitro* cytocompatibility[1]. Varies concentrations of nanomaterial, cross linking agents and degradation products from these scaffolds were also tested for their effect on viability of NIH3T3 fibroblasts and MC3T3 pre-osteoblasts. The results showed high cellular viability and attachment on nanocomposites made with GONP and GONR[1]. Furthermore, *in vivo* biocompatibility of GONP nanocomposites was

also investigated recently (yet to be published). Nanocomposites made with PLGA were implanted in non-critical sized monocortical defects in rat tibia. Bone growth within the scaffolds was then analyzed with microCT and histology two weeks after implantation. The results indicate nanocomposites made with GONP had comparable biocompatibility with PLGA alone. These results, taken together with results from aim 3 that demonstrate carbon nanoparticle enhanced PA increases bone growth, indicate that carbon nanoparticles are suitable for *in vivo* bone tissue engineering applications and could potentially be used to develop a combined device implant therapy for using PA to enhance bone tissue regeneration.

The implications of this study extend beyond bone tissue engineering. GONP nanoparticles have excellent contrast in magnetic resonance imaging.[3-5] Synthesis of GONP leads to confinement of trace amounts of Mn^{2+} ions between graphene sheets. This leads to GONP having relaxivity values ~20 times greater than clinically used contrast agents making them suitable as low concentration blood pool agents or molecular and cellular tags. Since GONP is taken up into cells even at low concentrations, as demonstrated in chapter 2, they can be used to tag MSCs for *in vivo* imaging with MRI. Furthermore, due to their ability to produce PA signals, they could also be used for PA imaging. This makes GONP a truly multi modal contrast agent that could allow MSCs, tagged with GONP, to be tracked *in vivo*. MSCs used for various therapeutic purposes could be tagged with GONP to allow for monitoring and ensuring targeted delivery.

In chapter 3 of this dissertation we investigate the use of multimodal ultrasound photoacoustic (US-PA) imaging for tissue engineering applications. Whole body imaging modalities has poor resolution and cannot distinguish tissue-engineering scaffolds from surrounding tissue. In this study, we demonstrate the use of multimodal US-PA imaging for tissue engineering applications. The location and morphology of polymeric and nanocomposite scaffolds can easily be detected and monitored using this modality. Furthermore, with the presence of carbon nanoparticles, such as SWCNT, in the polymeric matrix, nanocomposites can be imaged with PA generated from SWCNT. The scaffold structure and location can easily be delineated from surrounding tissue and

can be monitored longitudinally over time. Functional imaging is also facilitated with US-PA. Oxygen saturation calculated using PA could be used to monitor tissue penetration within the polymeric scaffolds. Since carbon nanoparticles produce strong PA signals at the wavelengths used to determine oxygen saturation they give false positive values for oxygen saturation. It is therefore only suitable for use with polymeric scaffolds without carbon nanoparticles.

The results from this study opens possibilities of further improving PA imaging modality for use with carbon nanoparticles. With modifications in imaging protocols and algorithms it is possible to obtain oxygen saturation values even with the presence of carbon nanoparticles in the sample. To calculate oxygen saturation within tissue or a polymeric scaffold, the area of interest is imaged using two different wavelengths. Differential PA intensity from the two wavelengths is used for calculations. Using known molar extinction coefficients of oxy hemoglobin and deoxy hemoglobin the concentrations of oxy hemoglobin and deoxy-hemoglobin can be calculated.[6] The ratio of these molecules is used to determine oxygen saturation. This protocol could be modified to utilize three wavelengths to determine three unknown concentrations: oxy hemoglobin, deoxy hemoglobin and carbon nanoparticles.[7] This would allow the determination of oxygen saturation and nanoparticle concentration *in vivo* using PA imaging for applications in an outside tissue engineering.

PA signals, currently used only for imaging applications, was demonstrated to have anabolic properties in enhancing bone fracture healing in chapter 4. This is the first study of its kind that demonstrates carbon nanoparticle enhanced PA stimulation increases bone regeneration *in vivo*. Bone regeneration can be enhanced with various mechanical stimulations such as whole body vibrations, LIPUS or pulsed electromagnetic field (PEMF)[8-11] etc. Most common clinically prescribed non-pharmacological therapies for non-unions or critical sized defects are LIPUS and PEMF [12, 13]. LIPUS treatment is usually applied for only 20 minutes daily while PEMF treatment requires up to 8 hours daily stimulation; making patient compliance crucial for successful treatment. LIPUS has been shown to be efficacious in healing delayed union and stress

fractures in various clinical trials [13]. It has also been shown to accelerate healing in critical sized defects treated with bone grafts. PEMF is similarly effective in healing non-union or delayed union long bone fractures but it is more commonly used to increase vascularization to treat osteonecrosis. Carbon nanoparticle enhance PA (CEPS) technology is different from these stimulations because it combines a mechanical stimulation with an implant. Furthermore, CEPS would provide therapy while simultaneously allow anatomical and functional PA imaging to monitor and assess healing over time. Carbon nanocomposite implanted at the critical sized defect site would provide the mechanical strength required for weight bearing, while simultaneously increase tissue attachment and regeneration in the micro and nano scale due to the presence of carbon nanoparticles. Upon stimulation with NIR light, these nanoparticles will produce ultrasonic signals that would provide highly localized mechanical stimulation at the defect site. This could in turn activate pathways that enhance bone tissue regeneration within the scaffold [14-17] without affecting neighboring tissue. The differentiating factor of CEPS from LIPUS or PEMF is its ability to provide feedback of the healing process. Oxygen saturation information obtained from PA imaging would give physicians real time feedback of the efficacy of the treatment and allow for adjustments in therapy. Oxygen saturation, a potentially useful indicator of healing, could also be used to assess osteonecrosis at fracture site. However, PA imaging modality is limited by penetration depth of the laser. NIR used in CEPS is limited to ~1 cm penetration in tissue[18]. This would limit the use of CEPS to bones with proximity to the skin surface. Fractures in scaphoid and hamate in the wrist, fifth metatarsal in the feet, and periosteal tibia in the leg are notorious for non-unions or delayed healing[19-21]. Since all these bones lie near the skin surface, they could potentially be treated with CEPS. Taken together, CEPS could be an ideal device implant solution to delayed, non-union or critical sized bone defects that would accelerate while simultaneously monitor healing in real time. Even though the dissertation does not test such an implant, it lays the foundation of knowledge required to develop a device implant combined PA therapy to treat bone defects. This dissertation investigates components of safety,

utility and efficacy of carbon nanoparticle enhanced photoacoustic imaging and therapy for bone tissue engineering.

References

[1] B. Farshid, G. Lalwani, B. Sitharaman, In vitro cytocompatibility of one-dimensional and two-dimensional nanostructure-reinforced biodegradable polymeric nanocomposites, Journal of Biomedical Materials Research Part A 103(7) (2015) 2309-2321.

[2] G. Lalwani, A.M. Henslee, B. Farshid, L. Lin, F.K. Kasper, Y.X. Qin, A.G. Mikos, B. Sitharaman, Two-dimensional nanostructure-reinforced biodegradable polymeric nanocomposites for bone tissue engineering, Biomacromolecules 14(3) (2013) 900-9.

[3] S. Kanakia, J.D. Toussaint, S.M. Chowdhury, G. Lalwani, T. Tembulkar, T. Button, K.R. Shroyer, W. Moore, B. Sitharaman, Physicochemical characterization of a novel graphene-based magnetic resonance imaging contrast agent, Int J Nanomedicine 8 (2013) 2821-2833.

[4] S. Kanakia, J. Toussaint, D.M. Hoang, S. Lee, K. Shroyer, W. Moore, Y. Wadghiri, B. Sitharaman, Towards An Advanced Graphene-Based Magnetic Resonance Imaging Contrast Agent: Sub-acute Toxicity and Efficacy Studies in Small Animals, Scientific reports 5 (2014) 17182-17182.

[5] B.S. Paratala, B.D. Jacobson, S. Kanakia, L.D. Francis, B. Sitharaman, Physicochemical characterization, and relaxometry studies of micro-graphite oxide, graphene nanoplatelets, and nanoribbons, PloS one 7(6) (2012) e38185.

[6] X. Wang, X. Xie, G. Ku, L.V. Wang, G. Stoica, Noninvasive imaging of hemoglobin concentration and oxygenation in the rat brain using high-resolution photoacoustic tomography, Journal of biomedical optics 11(2) (2006) 024015-024015-9.

[7] S. Kim, Y.-S. Chen, G.P. Luke, S.Y. Emelianov, In vivo three-dimensional spectroscopic photoacoustic imaging for monitoring nanoparticle delivery, Biomedical optics express 2(9) (2011) 2540-2550.

[8] P. Hannemann, E. Mommers, J. Schots, P. Brink, M. Poeze, The effects of low-intensity pulsed ultrasound and pulsed electromagnetic fields bone growth stimulation in acute fractures: a

systematic review and meta-analysis of randomized controlled trials, Archives of orthopaedic and trauma surgery 134(8) (2014) 1093-1106.

[9] H.M. Bilgin, F. Çelik, M. Gem, V. Akpolat, İ. Yıldız, A. Ekinci, M.S. Özerdem, S. Tunik, Effects of local vibration and pulsed electromagnetic field on bone fracture: A comparative study, Bioelectromagnetics (2017).

[10] F. Padilla, R. Puts, L. Vico, K. Raum, Stimulation of bone repair with ultrasound: a review of the possible mechanic effects, Ultrasonics 54(5) (2014) 1125-1145.

[11] T. Ogawa, X. Zhang, I. Naert, P. Vermaelen, C.M. Deroose, K. Sasaki, J. Duyck, The effect of whole-body vibration on peri-implant bone healing in rats, Clinical oral implants research 22(3) (2011) 302-307.

[12] R. Cadossi, E. Vaienti, L. Massari, G. Traina, Biophysical Stimulation with Pulsed Electromagnetic Fields in Avascular Necrosis of the Femur Head, Avascular Necrosis of the Femoral Head: Current Trends, Springer2004, pp. 33-44.

[13] S. Schandelmaier, A. Kaushal, L. Lytvyn, D. Heels-Ansdell, R.A. Siemieniuk, T. Agoritsas, G.H. Guyatt, P.O. Vandvik, R. Couban, B. Mollon, Low intensity pulsed ultrasound for bone healing: systematic review of randomized controlled trials, bmj 356 (2017) j656.

[14] J. Kusuyama, K. Bandow, M. Shamoto, K. Kakimoto, T. Ohnishi, T. Matsuguchi, Low intensity pulsed ultrasound (LIPUS) influences the multilineage differentiation of mesenchymal stem and progenitor cell lines through ROCK-Cot/Tpl2-MEK-ERK signaling pathway, The Journal of biological chemistry 289(15) (2014) 10330-44.

[15] H.Z. Ma, B.F. Zeng, X.L. Li, Y.M. Chai, Temporal and spatial expression of BMP-2 in sub-chondral bone of necrotic femoral heads in rabbits by use of extracorporeal shock waves, Acta orthopaedica 79(1) (2008) 98-105.

[16] L. Ren, Z. Yang, J. Song, Z. Wang, F. Deng, W. Li, Involvement of p38 MAPK pathway in low intensity pulsed ultrasound induced osteogenic differentiation of human periodontal ligament cells, Ultrasonics 53(3) (2013) 686-90.

[17] Z. Yang, L. Ren, F. Deng, Z. Wang, J. Song, Low-intensity pulsed ultrasound induces osteogenic differentiation of human periodontal ligament cells through activation of bone morphogenetic protein-smad signaling, Journal of ultrasound in medicine : official journal of the American Institute of Ultrasound in Medicine 33(5) (2014) 865-73.

[18] E.L. Rosenthal, J.M. Warram, K.I. Bland, K.R. Zinn, The status of contemporary image-guided modalities in oncologic surgery, Annals of surgery 261(1) (2015) 46.

[19] I.R. Murray, C.J. Foster, A. Eros, C.M. Robinson, Risk factors for nonunion after nonoperative treatment of displaced midshaft fractures of the clavicle, The Journal of bone and joint surgery. American volume 95(13) (2013) 1153-8.

[20] A.R. King, S.L. Moran, S.P. Steinmann, Humeral nonunion, Hand clinics 23(4) (2007) 449-56, vi.

[21] A.M. Furr, J.M. Schweinfurth, W.L. May, Factors associated with long-term complications after repair of mandibular fractures, The Laryngoscope 116(3) (2006) 427-30.